Amorphous Silicon Based Solar Cells

Von der Fakultät Informatik, Elektrotechnik und Informationstechnik
der Universität Stuttgart zur Erlangung der Würde eines
Doktor-Ingenieurs (Dr.-Ing.) genehmigte Abhandlung

Vorgelegt von

Anas Al Tarabsheh

geboren am 30.06.1978 in Irbid / Jordanien

Hauptberichter: Prof. Dr. rer. nat. habil. J. H. Werner
Mitberichter: Prof. Dr.-Ing. N. Frühauf

Tag der Einreichung: 15.11.2006
Tag der mündlichen Prüfung: 29.01.2007

Institut für Physikalische Elektronik der Universität Stuttgart
2007

Contents

Abstract

This thesis focuses on the deposition of hydrogenated amorphous silicon (a-Si:H) films by means of plasma enhanced chemical vapor deposition (PECVD). This technique allows the growth of device quality a-Si:H at relatively low deposition temperatures, below 140 °C and, therefore, enables the use of low-cost substrates, e.g. plastic foils. The maximum efficiencies of a-Si:H solar cells in this work are $\eta = 6.8$ % at a deposition temperature $T_{\text{dep}} = 180$ °C and $\eta = 5.9$ % at a deposition temperature $T_{\text{dep}} = 135$ °C.

Decreasing the deposition temperature deteriorates the structural and electronic quality of a-Si:H films. Therefore, the deposition conditions are carefully optimized at low temperatures. The mismatch in the mechanical properties of the plastic foils and the inorganic semiconductor layers have less effect on the a-Si:H films at low deposition temperatures. As a result, the deposition temperatures should be decreased to minimize mechanical deterioration of the films but without losing too much of the electronic properties of the films.

A novel analytical description of the current density/voltage (J/V) characteristics of p-i-n solar cells well represents experimental J/V curves of a-Si:H solar cells. The extended model solves the continuity and transport equations for electrons and holes, and fully accounts for the contributions of the drift and the diffusion currents. Many analytical models neglect the contribution of the diffusion current in describing the a-Si:H solar cells. Other existing models assume the diffusion lengths of electrons and holes to be equal, resulting in a symmetric distribution of carrier concentrations around the center of the intrinsic layer of the p-i-n solar cells. Both restrictions strongly limit the ability of these analytical models to accurately reproduce the J/V-characteristics of real solar cells.

In contrast to existing analytical models , the new analytical description solves the continuity and transport equations of carriers at each location within the i-layer for the whole range of applied voltages. The peculiar extension of this model over

previous ones enables a more realistic description of solar cells.

My novel analytical model implements i) different values of the diffusion lengths, or mobility-lifetime products, of electrons and holes, and ii) realistic wavelength and depth dependencies of the photogeneration rate of charge carriers. The results of the model demonstrate that the location of the main recombination path of the photogenerated carriers inside the i-layer is voltage dependent, rather than being fixed at the middle of the i-layer as existing models assume. For a realistic description of the solar cell optics in calculating the J/V-characteristics, I fully account for the reflection of photons at the back contact. The model proves that the performance of a-Si:H solar cells which are illuminated through the p-layer is better than the one of cells illuminated through the n-layer. Testing corresponding J/V-characteristics from this model against experimental data of bifacial a-Si:H solar cells with transparent front and backside contacts, reveals that this extended analytical model well describes the output characteristics of real a-Si:H p-i-n solar cells. The model proves that the current collection of bifacial p-i-n solar cells is larger if the light enters through the p-layer because the mobility μ_n of electrons is larger than the mobility μ_p of holes.

This thesis also investigates the dependence of the electrical and optical properties of a-Si:H films on the deposition conditions, and how those properties are enhanced by optimizing the deposition conditions. I apply the optimized layers to solar cells deposited on glass and on polyethylene terephtalate (PET) substrates. The incorporation of a buffer layer or a microcrystalline layer enhances the performance of the cells. In order to realize flexible cells, I study the mechanical properties of the films, i.e. the mechanical interaction between the a-Si films and the flexible foils, by measuring the curvature (bending) of the substrates after coating with a-Si:H. The higher the mismatch between the deposited films and the substrate is, the higher the curvature of the substrate will be. To decrease this curvature, the ratio between thickness of the deposited film and the substrate should be maximized.

Due to the wide spread applications of a-Si:H solar cells under low illumination intensities, this work analyzes the behavior of the a-Si:H devices under different illumination levels. The measurements of the J/V-characteristics yield an illumination-intensity dependent parallel resistance rather than a constant one. The intensity dependence follows a power law which I ascribe to the photoconductivity of parallel resistances distributed over the whole solar cell area. From this model, I develop a new method, called partial shading method, of characterizing the component cells of commercial thin film modules, without electrical access to the single cells. Removal

or destruction of the lamination for physically contacting individual cells in a photovoltaic module is avoided by recording the global current density characteristics of the whole module. During the measurement, each component cell is subsequently exposed to a reduced illumination intensity Φ while all other cells of the module are fully illuminated. By this method, I qualitatively study each cell of the module and then identify the shunted cells.

Zusammenfassung

Die vorliegende Arbeit untersucht die Herstellung von Solarzellen aus wasserstoffhaltigem amorphen Silizium (a-Si:H) durch Plasma Enhanced Chemical Vapor Deposition (PECVD) bei Temperaturen unter 140 °C. Eine niedrige Herstellungstemperatur ermöglicht die Verwendung flexibler Kunststofffolien als Substrat, verschlechtert aber die elektronischen Eigenschaften der a-Si:H Schichten und Solarzellen. Daher müssen die Abscheideparameter bei niedrigen Temperaturen besonders sorgfältig optimiert werden. Bei niedrigen Herstellungstemperaturen wirken sich die Unterschiede zwischen den mechanischen Eigenschaften der Kunststoffsubstrate und denjenigen der anorganischen Halbleiterschichten weniger stark aus als bei hohen Substrattemperaturen. Insgesamt sucht die vorliegende Arbeit, einen Kompromiss zwischen der Absenkung der Abscheidetemperatur und der elektronischen Qualität der Schichten und Solarzellen zu erreichen. Ein wichtiger Teil dieser Arbeit stellt in Kapitel 3.1 eine neue analytische Beschreibung der Strom/Spannungs-Kennlinie von a-Si:H p-i-n Solarzellen vor. Dieses erstmals veröffentlichte Modell löst die Kontinuitäts- und Transportgleichungen für Elektronen und Löcher und berücksichtigt Feld- und Diffusionsströme. Bisher bekannte analytische Modelle für p-i-n Solarzellen vernachlässigen den Beitrag der Diffusionsströme, oder sie gehen von der Annahme aus, dass die Diffusionslängen von Elektronen und Löchern gleich sind, was zu einer symmetrischen Verteilung der Ladungsträgerkonzentrationen um die geometrische Mitte der intrinsischen Absorberschicht der p-i-n Dioden führt. Beide Einschränkungen beschreiben die Situation in p-i-n Strukturen, beispielsweise aus a-Si:H, nur unzureichend und grenzen daher die Fähigkeit der vorhandenen analytischen Modelle stark ein, J/V-Kennlinien realer Solarzellen genau zu reproduzieren oder vorher zu sagen. Die wesentliche Erweiterung gegenüber den existierenden analytischen Modellen besteht darin, die Kontinuitäts- und Transportgleichungen der Träger für jeden Ort innerhalb der i-Schicht über den gesamten Bereich der angelegten Spannungen zu lösen. Diese Erweiterung ermöglicht eine realistische Beschreibung

4

tatsächlicher Solarzellen, wie die Vergleiche mit experimentellen Daten in den Kapiteln 3.1.3 belegen. Realistische Annahmen zur Anwendung der analytischen Modellierung berücksichtigen zum einen unterschiedliche Werte der Diffusionslängen von Elektronen und Löchern, und zum anderen die Energie- und Ortsabhängigkeit der Photogenerationsrate innerhalb der i-Schicht entlang der Einstrahlungsrichtung des einfallenden Lichtes. Die Ergebnisse der erweiterten analytischen Beschreibung demonstrieren, dass der Ort maximaler Ladungsträgerrekombination innerhalb der i-Schicht spannungsabhängig ist, anstatt einer Fixierung in der Mitte der i-Schicht wie in bisherigen Modellen. Um die optischen Eigenschaften der p-i-n Solarzellen aus a-Si:H realistisch zu beschreiben, berücksichtigt das neue Modell auch den Beitrag der Reflexion niederenergetischer Photonen am rückseitigen Kontakt. Die Modellierung bestätigt, dass die Leistung von amorphen Solarzellen, die durch die p-Schicht beleuchtet werden, besser ist als diejenige von Zellen, die durch die n-Schicht beleuchtet werden. Entsprechend modellierte J/V-Kennlinien stimmen gut mit experimentellen Daten von a-Si:H Solarzellen mit durchsichtigem Front- und Rückkontakt überein. Der experimentelle Teil der Arbeit untersucht die Abhängigkeit der elektronischen und optischen Eigenschften von a-Si:H Filmen von den Abscheidebedingungen, und optimiert die Eigenschaften durch die Variation der Abscheideparameter. Die optimierten Schichten kommen in Solarzellen auf Glas sowie auf Polymerfolien aus Polyethylenterephtalat (PET) und Polyethylennaphtalene (PEN) zum Einsatz. Die Leistung der a-Si:H Solarzellen verbessert sich durch Einfügen einer Pufferschicht oder einer mikrokristallinen Dotierschicht und erreicht einen maximalen Wirkungsgrad $\eta = 6.8\,\%$ bei einer Abscheidetemperatur $T_{\mathrm{dep}} = 180$ °C und $\eta = 5.9\,\%$ bei einer Abscheidetemperatur $T_{\mathrm{dep}} = 135$ °C. Bei der Übertragung von Abscheideparametern, die bei niedriger Temperatur auf starren Glassubstraten optimiert wurden, auf flexible Foliensubstrate müssen die Unterschiede in den mechanischen Eigenschaften der anorganischen Halbleiterfilme und der Polymerfolien berücksichtigt und untersucht werden. Die Wechselwirkung zwischen den amorphen Filmen und den flexiblen Folien erzeugt mechanische Spannungen und ein Aufrollen der Substraten. Je höher die Fehlanpassung zwischen den abgeschiedenen Filmen und dem Substrat ist, desto stärker rollt sich die flexible Solarzelle ein. Um dieses Aufrollen zu quantifizieren und zu reduzieren, variiert die Arbeit das Verhältnis der Dicken der abgeschiedenen a-Si:H Filme und der Substratfolien. Aufgrund der breiten Anwendungsmöglichkeiten von a-Si:H Solarzellen bei niedrigen Beleuchtungsintensitäten untersuchen die Kapitel 3.5 und 3.6 das Verhalten von a-Si:H Zellen und Modulen unter verschiedenen Bestrahlungsstärken. Die Messungen

der J/V-Kennlinien liefern keinen konstanten, sondern einen intensitätsabhängigen Parallelwiderstand der Solarzellen. Die Intensitätsabhängigkeit folgt einem Potenzgesetz, das ich der Photoleitfähigkeit der i-Schicht in den Solarzellen zuschreibe, die zu einem intensitätsabhängigen Parallelwiderstand führt, der über die gesamte Solarzellenfläche verteilt ist. Ausgehend von dieser Beobachtung entwickelt die Arbeit in Kapitel 3.6.3 eine neuartige Methode der Teilabschattung, um die Einzelzellen innerhalb eines serienverschalteten Dünnschicht-Photovoltaikmoduls zu charakterisieren, und zwar ohne einen elektrischen Zugang zu den Kontakten der Einzelzellen zu haben. Während dieser Messung werden die Einzelzellen im Modul sequentiell mit einer verringerten Lichtintensität beleuchtet, während alle anderen Zellen des Moduls mit voller Intensität beleuchtet bleiben. Dadurch lässt sich jede Einzelzelle des Moduls qualitativ untersuchen, und die Parallelwiderstände oder eventuelle Fertigungsprobleme, beispielsweise bei der Verschaltung durch Laserschreiben, lassen sich bei den einzelnen Zellen im Modul lokalisieren.

Chapter 1

Introduction

The first remarkable breakthrough of hydrogenated amorphous silicon (a-Si:H) came with the application of plasma for the decomposition of silane (SiH_4) by Chittick et. al. [1]. The second breakthrough was the possibility of doping the a-Si:H films by adding phosphine (PH_3) or diborane (B_2H_6) to the silane gas [2]. Carlson and Wronski reported the first amorphous silicon solar cell with an efficiency of 2.4 % in 1976 [3].

On the one hand, a-Si:H films behave as direct band gap semiconductors due to the breakdown of the selection rules for optical transitions and therefore, their absorption coefficient is high. This characteristic enables the a-Si:H solar cells to completely absorb sun light with thicknesses less than 1 μm. On the other hand, a-Si:H films can be deposited at low deposition temperatures around 100 ºC [4]. This facilitates the use of inexpensive and flexible substrate foils such as polyethylene terephtalate (PET) and polyethylene naphtalene (PEN), and therefore opens new photovoltaic applications.

The main goals of this thesis are

- studying a-Si:H films deposited at low deposition temperatures, and electrically and optically characterizing them in order to enhance their performance by adjusting the deposition conditions;

- investigating the mechanical interaction between a-Si:H films and the flexible foils as a function of foil and film thicknesses, in order to check the feasibility of building durable flexible a-Si:H solar cells on very thin polymer substrates;

- presenting a more accurate analytical description for the current density/ voltage (J/V) characteristics of a-Si:H solar cells by preventing some important

limitations of previous models;

- analyzing a-Si:H solar cells and photovoltaic modules under different illumination intensities, and characterizing their shunt resistances under low illumination intensities where in door and low-light seem to be very promising.

The organization of this thesis is as follows: Chapter 2 summarizes background knowledge about a-Si:H films and solar cells. This chapter includes the main structural, optical, and electrical characteristics of p-i-n and n-i-p a-Si:H solar cells depending on their layer deposition sequence.

Chapter 3.1 introduces a novel analytical model of the J/V-characteristics of a-Si:H solar cells. Chapters 3.2 and 3.3 present an optimization study of a-Si:H films and solar cells at low deposition temperatures, while Chapter 3.4 analyzes the requirements for making a-Si:H solar cells on flexible polymer foils.

Chapter 3.5 and 3.6 study the shunt resistance of a-Si:H solar cells under different illumination intensities, and introduce a non-destructive technique for characterizing integrated a-Si:H solar cells in photovoltaic modules without granting an access to the electrical contacts of each individual cell.

Chapter 2

Properties and characterization of amorphous silicon films and solar cells

2.1   Properties of amorphous silicon

Amorphous silicon (a-Si) is different from crystalline silicon (c-Si) in that it lacks the long range order. Random variations in bond angles and lengths [5] cause exponential band tails in the electronic density of states. Region (B) in Fig. 2.1 denotes the valence band tail, the slope of which is generally addressed as Urbach energy. Region (D) of Fig. 2.1 is the conduction band tail while Regions (A) and (E) represent the extended valence and the extended conduction band states, respectively. The variation of bond angles and lengths in amorphous silicon leads to the scattering of charge carriers and also to the broadening of the density of states leading to massive changes in the electrical and optical properties of the amorphous materials.

   The presence of energy states in the mid gap as deep defects is due the unsaturated valences or frequently called dangling bonds, represented by region (C) in Fig. 2.1. These defects prevent the Fermi energy from moving out of the mid gap position leading to the fact that the amorphous silicon is difficult to be doped. Therefore, decreasing the dangling bonds makes the doping more feasible. In a-Si films, the concentration of dangling bonds is of the order 10^{19}-10^{20} cm^{-3} [8]. The presence of hydrogen from the reactant gases during the deposition saturates most of the dangling bonds, reducing the concentration of dangling bonds to an order 10^{15}-10^{16}

cm^{-3}, producing a new material called hydrogenated amorphous silicon (a-Si:H) [6].
A high quality amorphous silicon should present mono-hydride or Si-H bonds, rather
than SiH$_2$ or SiH$_3$ bonds [7]
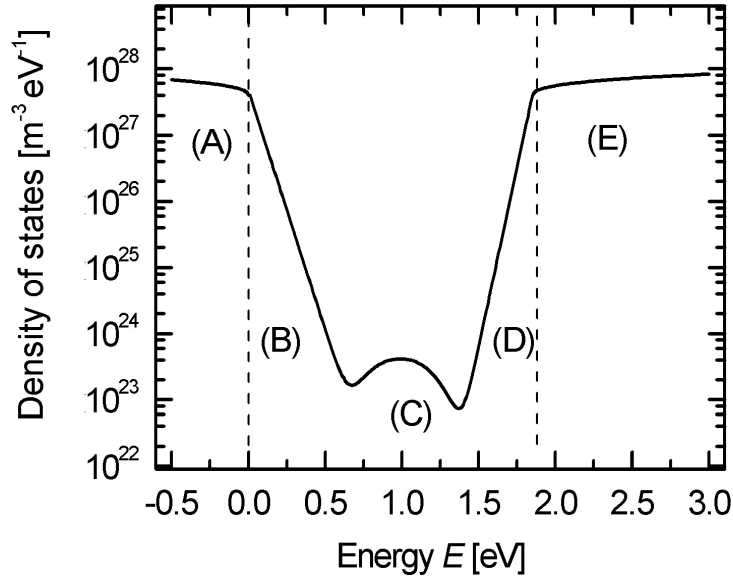
Fig. 2.1: Representation of the electronic density of states in a-Si:H. Region (A)
represents the extended valence band states, region (B) represents exponential distribution of the valence band tail states, region (C) represents the dangling bond
defect density, region (D) represents the exponential distribution of conduction band
tail states, and region (E) represents the extended conduction band states.

The structural disorder of a-Si and a-Si:H introduces localized band tail states
resulting in a difficulty of identifying a unique band gap of the material. Therefore,
the concept of a mobility gap is widely used because the mobility of charge carriers
drops by several orders of magnitude inside the gap.

The a-Si:H disorder network leads also to a non-periodic lattice potential, resulting in a direct optical transitions in a-Si:H. The a-Si:H films have a high optical
absorption coefficient in the visible range of the solar spectrum since the photon
energies within this range are absorbed by direct transition of the electrons from
the occupied states in the valence band to the empty states of the conduction band.

2.2 Deposition of amorphous silicon

All a-Si:H samples studied in this work were produced by the plasma enhanced chemical vapor deposition (PECVD) technique [9, 10]. The Plasma itself, referred to as the fourth state of matter[1], is a quasi-neutral gas containing charged particles, electrons and ions, governed by electromagnetic forces. It is produced by an electric field which delivers energy to the gas to ignite the plasma and maintain it [11, 12].

Many external parameters, that can be controlled, are involved in the plasma process: plasma power, pressure, hydrogen dilution, gas flow, reactor temperature, frequency [13, 14]. Layer deposition processes are characterized by the layer properties. Therefore, the interactions between plasma parameters and layer properties is important for a better process optimization. Increasing the plasma power increases the dissociation rate and therefore the deposition rate. However, the higher dissociation of silane could result in a change in the species involved in the growth because of an increasing importance of secondary reactions [15]. An increase of the pressure may produce similar effects [16] because of the increased electron-silane collisions, enhanced secondary reactions and deposition rate. The hydrogen dilution has been reported to be an excellent way to improve the a-Si:H properties. However, it can interact in the growth-zone to change a-Si:H to microcrystalline silicon growth [17, 18]. The reactor temperature strongly affects the plasma reactions. The effects of deposition temperature on the plasma reactions are discussed in [19–21].

Silane (SiH_4) is the most common source for a-Si:H deposition [22, 23]. The glow discharge decomposition of SiH_4 and the growth of a-Si:H films from SiH_4 plasmas [24] proceeds through several steps of gas phase and solid state reactions [25]. In the primary radical generation and ionization process, SiH_4 molecules gain energy through collisions with high energy electrons and get excited to their dissociative or ionization states. Therefore, neutral atoms, radicals and ions are formed and then diffuse on the substrate surface and finally condense into a-Si:H after various kinds of surface reactions for attending low energy configurations. The mobility of those radicals at the growing a-Si:H surface is often considered an important factor for the deposition of high quality a-Si:H films [26].

Among the various deposition methods of a-Si:H [27], PECVD using radio frequency RF ($f = 13.56$ MHz) and very high frequency VHF ($f = 80$ MHz) excitations are still the most widely used today in research and manufacturing of a-Si:H based materials. Interestingly, during the growth of a-Si:H by PECVD, dopants can be

---

[1]The three other ones being the solid state, the liquid state, and the gas state.

mixed with silane SiH$_4$ in a controlled way to achieve the desired doping level. The addition of diborane (B$_2$H$_6$) to silane results in an p-type a-Si:H, where the Fermi level is shifted toward the valence band (VB), while the addition of phosphine (PH$_3$) to silane results in an n-type a-Si:H, where the Fermi level is shifted toward the conduction band (CB). The shifts of the Fermi levels in both types of doping are limited by the band-tails and the deep defects in the gap of a-Si:H and therefore, it is impossible to move the Fermi levels closer to the VB than 300 meV for p-type a-Si:H, and closer than 150 meV to the CB for n-type a-Si:H. In our labs, the concentration of the two types of dopants in the feed stock gas is 2%.

The deposition of doped a-Si:H layers in the PECVD machine used in this work is done in one chamber for both p- and n-type films, while the deposition of intrinsic (i-) a-Si:H layers is done in a separate chamber since the material quality of the intrinsic a-Si:H layers depends strongly on the contamination.

2.3   Characterization of amorphous silicon

2.3.1   Film characterization

Optical characterization

Optical transmission measurements yield the growth rate r ($r = d/t_{\mathrm{dep}}$ with film thickness d and deposition time t_{dep}) and the energy dependent optical constants of a-Si:H-based films [28] which include the optical band gap E_{g}, the absorption coefficient α, and the refractive index n_{rix}. An ultraviolet/visible/near-infrared (UV/VIS/NIR) spectrophotometer (Varian Cary-5) measures the optical transmission T_{r} in the range of wavelengths from 400 nm to 2000 nm. The evaluation software Diplot [29], models the transmission of the films with d, E_{g}, and n_{rix} as parameters. The thickness d is determined from the interference fringes of the transmission spectrum [30]. Fig. 2.2 shows an example of a transmission spectrum (circles) of a-Si:H film and the fit to the data (solid line). The films that I characterize here are deposited on transparent substrates (Corning glass 7059 or polyethelyne terephthalate foils).
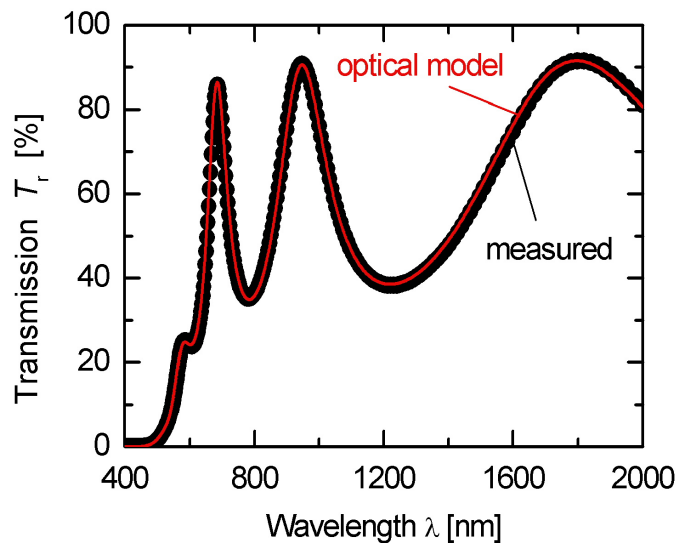

Fig. 2.2: Optical transmission measurement of an a-Si:H layer. The circles represent the measured transmission data while the solid line represents an optical model used to extract the optical properties of the measured film. The modeled parameters are: $d = 300.7 \pm 8.6$ nm, $E_{\mathrm{g}} = 1.85$ eV, and $n_{\mathrm{rix}} = 3.37$.

Electrical characterization

Four characterization techniques give information about the transport properties of a-Si:H films: temperature-dependent dark conductivity, photoconductivity, constant photocurrent method (CPM), and steady-state photocarrier grating (SSPG). For all these measurements, I used a-Si:H films with coplanar "*T*'"-shaped contacts, made by evaporation of aluminum through a shadow mask. Fig. 2.3 shows the contact geometry. The separation between the contacts is 1 mm, and their width is 10 mm.
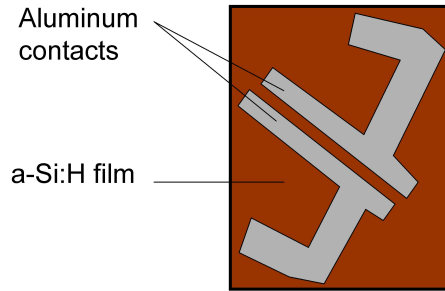
Fig. 2.3: Contact geometry used for all the electrical characterizations. In this coplanar geometry the current flows parallel to the substrate. The contacts are separated by 1 mm, and are 10 mm wide.

Temperature-dependent dark conductivity

This experiment is carried out under vacuum ($\sim 10^{-3}$ Pa) to eliminate moisture and oxygen at the sample surface, which might lead to parasitic conduction paths. To obtain the temperature-dependent dark conductivity $\sigma_{\text{dark}}(T)$, I place the sample with its electrical contacts on a heating plate in a dark vacuum chamber. The computer-controlled measurement of $\sigma_{\text{dark}}(T)$ consists of the following steps: the sample is fast heated up to 480 K; then the temperature is kept constant for 60 minutes ("annealing" step); and finally a controlled decreasing temperature ramp is applied to the sample. During the last step I apply a constant voltage V of 50 V for intrinsic a-Si:H films, or 0.1 V for highly-doped a-Si:H films (to prevent the current limit of the measurement setup) between the "*T*'"-contacts of the sample, and measure the corresponding current I in the temperature range from 480 to 200 K. $\sigma_{\text{dark}}(T)$ is then calculated as follows by taking into account the geometry

$$\sigma_{\text{dark}}(T) \quad = \quad \frac{l}{wd}\frac{I(T)}{V}, \tag{2.1}$$

where l is the separation of the contacts, w is their width, and d is the thickness

of the sample.

The measurement of $\sigma_{dark}(T)$ gives us access to the activation energy E_{act}, as defined in Fig. 2.4 and Eq. (2.2a). In the case of crystalline silicon, E_{act} is temperature independent because only the free carriers outside the band gap contribute to the current, while in amorphous silicon the electronic states within the band gap are occupied states up to the Fermi level E_F, in Fig. 2.4b. Heating the a-Si:H-based film increases the energy of the carriers and therefore, E_F statistically moves towards the conduction band E_C with a temperature coefficient ξ. Therefore, one must conclude that the activation energy itself is temperature dependent in a-Si:H-based semiconductors, i.e.

$$\sigma_{dark}(T) = \sigma_0 \exp\left(-\frac{E_{act}(T)}{kT}\right), \tag{2.2a}$$

$$= \sigma_0 \exp\left(\frac{\xi}{k}\right) \exp\left(-\frac{E_{act}^*}{kT}\right), \tag{2.2b}$$

$$= \sigma_{00} \exp\left(-\frac{E_{act}^*}{kT}\right), \tag{2.2c}$$

where ξ represents the statistical shift of the Fermi level, k is the Boltzmann constant, E_{act}^* is the slope of the Arrhenius plot of Eq. (2.2c), and σ_{00} is the extrapolation of the plot to $1/T \sim 0$ as shown in Fig. 2.5. In order to make the calculation of temperature-dependent dark conductivity $\sigma_{dark}(T)$ easier, Refs. [31, 32] apply $\sigma_{00} = 200$ S/cm. However, in my work, the values of the activation energy E_{act} represent $E_{act}(T = 300K)$, i.e. at room temperature. Fig. 2.5 presents the Arrhenius plot of the dark conductivity of two examples of p- and n-layers.

Photoconductivity

The photoconductivity σ_{photo} measurement consists of measuring the current of a sample while illuminating uniformly the area between the two coplanar metallic contacts on which the voltage V is applied. σ_{photo} describes the layer transport properties of a-Si:H films [33] and is written as

$$\sigma_{photo} = qG\left(\mu_n \tau_n + \mu_p \tau_p\right), \tag{2.3}$$

where G is the generation rate, $\mu_n \tau_n$ and $\mu_p \tau_p$ are the mobility-lifetime products of electrons and holes, respectively [34]. The calculation of the photoconductivity from Eq. (2.3) gives a direct access to the mobility-lifetime product of the majority carriers $(\mu\tau)_{Maj}$ [35] since $\mu_n \tau_n > \mu_p \tau_p$ [15, 36] results in:
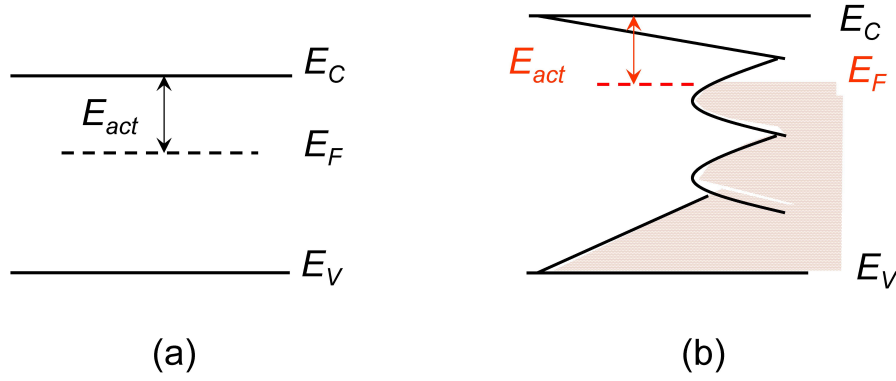
Fig. 2.4: Band diagram of a) crystalline silicon, and b) amorphous silicon based films, showing the energies of the conduction band E_{C} and the valence band E_{V}. The activation energy E_{act} is the energy difference between E_{C} and the Fermi level E_{F}.
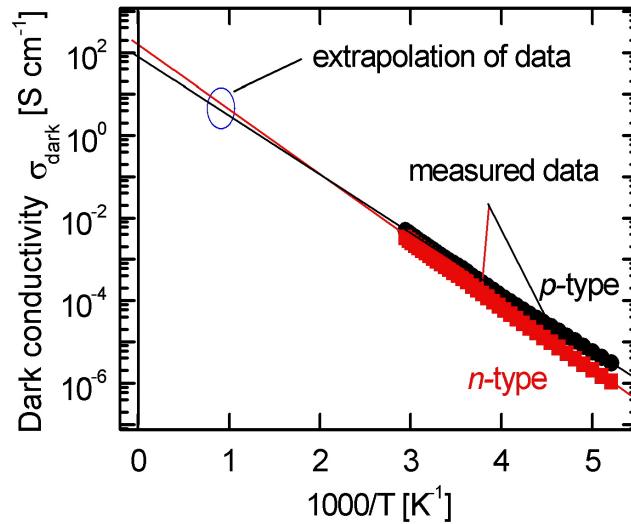
Fig. 2.5: Arrhenius plot of the dark conductivity $\sigma_{\mathrm{dark}}(T)$ of two samples of p- and n-layers. E^{*}_{act} is calculated directly from the slope of the data while σ_{00} is calculated from the extrapolated data at $1/T = 0$. In this example, $E^{*}_{\mathrm{act}} = 283$ meV, 285 meV for the p- and n-layers, respectively. While the values of ξ are 7.7 $\times 10^{-5}$ eV K^{-1}, 8.2 $\times 10^{-5}$ eV K^{-1} for the p- and n-layer, respectively.

$$\sigma_{photo} \;=\; qG\,(\mu\tau)_{\mathrm{Maj}}\,. \tag{2.4}$$

The last equation is also valid for intrinsic a-Si:H layers because they are slightly n-type. Therefore, in this case, σ_{photo} is linked to the mobility-lifetime product of electrons. The ratio between the photoconductivity and dark conductivity is called the photosensitivity Ψ

$$\Psi = \frac{\sigma_{\mathrm{photo}}}{\sigma_{\mathrm{dark}}}. \tag{2.5}$$

The higher the photosensitivity Ψ of intrinsic films is, the more electron-hole pairs are generated inside the films, resulting in a higher photocurrent. In my work, the photoconductivity measurement has not been applied for doped a-Si:H films because their photosensitivity is very close to unity.
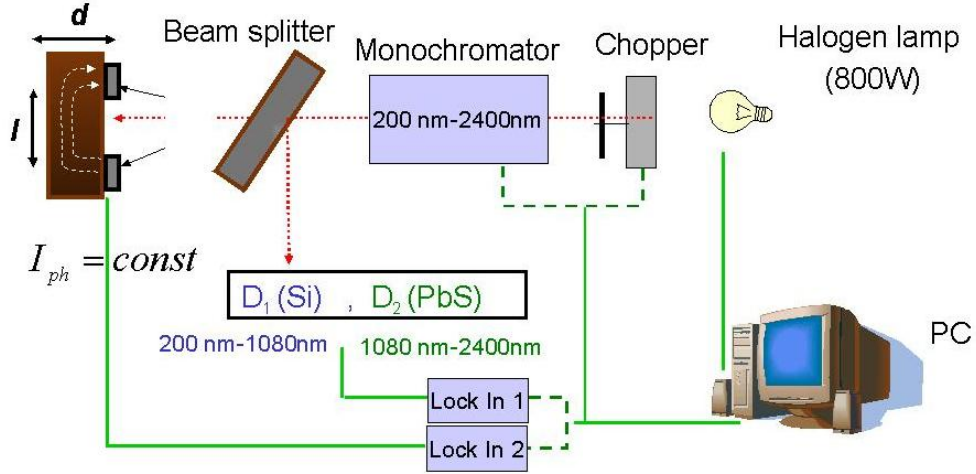
Constant Photocurrent Method

The Constant Photocurrent Method (CPM) is one of the methods used to measure the subgap absorption coefficient $\alpha(h\nu)$ of a-Si:H films [37]. $\alpha(h\nu)$ is calculated by measuring the photon flux $\Phi(h\nu)$ necessary to keep the photocurrent I_{ph} constant [2], under the assumption that the generation rate G is also constant and consequently, $\alpha(h\nu)$ is written as

$$\alpha = \frac{1}{\Phi} \frac{\sigma_{\mathrm{photo}}}{q\left(\mu_{\mathrm{n}}\tau_{\mathrm{n}} + \mu_{\mathrm{p}}\tau_{\mathrm{p}}\right)}. \tag{2.6}$$

Fig. 2.6 shows the setup of the CPM measurement. The intensity of the halogen lamp is controlled by the computer to keep the measured I_{ph} constant. The applied voltage is 100 V. However the application of lower voltages does not affect the measurement as will be discussed later. This measurement is carried out at room temperature and in air.

The absorption coefficient α_{CPM} measured by CPM is relative and therefore has to be calibrated at high energies of the absorption spectra against data obtained from the optical transmission measurements as shown in Fig. 2.7. The CPM spectrum is divided into three regions; in region α_{A}, the transitions of carriers from band to band occur due to the high energy of photons $h\nu > E_g$. In region α_{B}, the trapping of carriers at the tail states, which increase towards the mobility edges exponentially, contributes to the absorption of photons with $h\nu < E_{\mathrm{g}}$. The last region α_{C} provides information about the concentration of dangling bonds N_{s} [38].

[2]$I_{\mathrm{ph}} = \sigma_{\mathrm{ph}}Vwd/l$, similar to Eq. (2.1).

Fig. 2.6: Setup of the constant photocurrent method (CPM). The number of photons is adjusted to keep the photo current I_{ph} of the sample constant while the photon energy $h\nu$ of the incident light is varying. The CPM measurement is automatically controlled by a personal computer (PC).

A good and frequently verified relation between the CPM and density of dangling bonds is calculated by integrating the region α_C using the following formula [41]

$$N_s[cm^{-3}] = (1.9 \pm 0.3) \times 10^{16} \left(\int\limits_{h\nu_1}^{h\nu_2} \alpha[cm^{-1}] - \frac{1}{2} \frac{\alpha[cm^{-1}]h\nu_2}{(h\nu_2 - h\nu_1)} \right) dE[eV]. \qquad (2.7)$$

The integration limits, $h\nu_1$ and $h\nu_2$, are set empirically as in Fig. 2.7c, where $h\nu_2 = 1.2$ eV [39]. The exponential decay of the band tail states distribution is defined as the Urbach energy E_U [40]. The Urbach energy E_U hence quantifies the broadening of the bands and is determined from the slope of the linear part of the absorption spectrum of Fig. 2.7c as

$$\alpha = \alpha_0 \exp\left(\frac{E}{E_U} \right). \qquad (2.8)$$
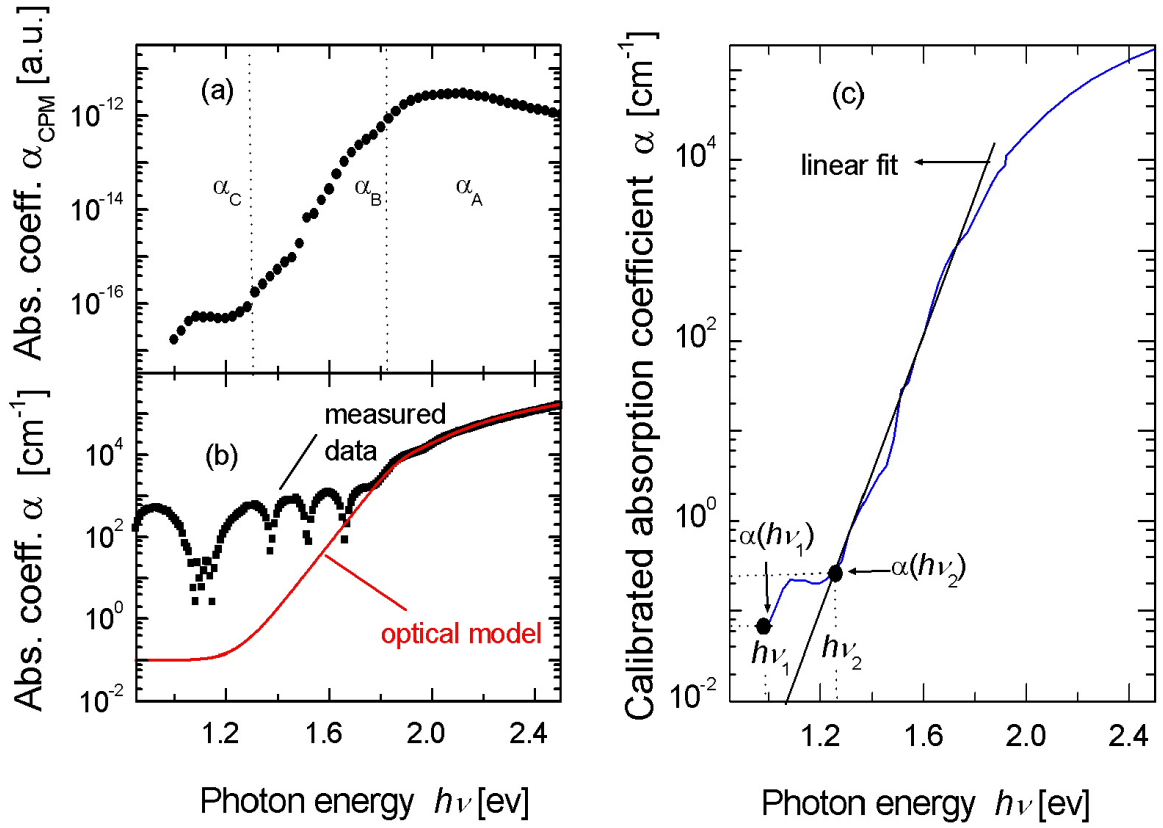
Fig. 2.7: Absorption coefficient $\alpha(h\nu)$ obtained from a) CPM measurement (electrical), b) transmission measurement (optical), and c) calibration of the electrical and optical measurements for an intrinsic a-Si:H film (AnM0507066). The spectrum of CPM is described by three different regions α_A, α_B, and α_C. In region α_A, due to $h\nu > E_g$ the transitions of carriers from band to band occur, while in region α_B, $h\nu < E_g$. In this region the trapping of carriers into the tail states, which increase exponentially towards the mobility edges, contributes to the absorption of photons. The last region α_C, where also $h\nu < E_g$, gives us information about the concentration of dangling bonds N_s. The Urbach energy E_U is determined from the slope of the linear part of the semi-logarithmic plot of the spectrum.

Steady-State Photocarrier Grating

The steady-state photocarrier grating (SSPG) method is used to determine the ambipolar diffusion length L_{amb} in intrinsic a-Si:H layers [42]. Contrary to σ_{photo}, the ambipolar diffusion length L_{amb} is linked to the mobility-lifetime product of

minority carriers [43, 44]

$$L_{\mathrm{amb}}^2 = V_{\mathrm{t}} \frac{\mu_{\mathrm{n}} \tau_{\mathrm{n}} \mu_{\mathrm{p}} \tau_{\mathrm{p}}}{\mu_{\mathrm{n}} \tau_{\mathrm{n}} + \mu_{\mathrm{p}} \tau_{\mathrm{p}}} C, \tag{2.9}$$

where $V_{\mathrm{t}} = kT/q$ is the thermal voltage and C is a correction constant between 1 and 2. The principle of SSPG technique is to measure the small-signal photocurrent in a sample exposed to optical fringes, and compare this photocurrent to the one obtained under uniform illumination, i.e. without fringes [45].

Fig. 2.8 illustrates the setup of measuring the ambipolar diffusion length L_{amb} of a-Si:H films. The two light beams I_1 and I_2 which illuminate the sample interfere and form a sinusoidally varying light intensity pattern [48]

$$I(x) = (I_1 + I_2) \left[1 + \gamma_0 \frac{2\sqrt{I_1 I_2}}{I_1 + I_2} \cos \left(\frac{2\pi x}{\Lambda} \right) \right], \tag{2.10}$$

where $0 < \gamma_0 < 1$ is a factor by which the fringe visibility is reduced because of partial coherence between the two beams, $\Lambda = \lambda/\left[2 \sin \left(\theta/2 \right) \right]$ is the grating period, λ is the wavelength of the laser source, θ is the angle between the two beams, and x is the coordinate perpendicular to the intersect between the two beams.

The interference of the two beams leads to the formation of a non-uniform distribution of carriers [46, 47] resulting in non-homogeneous conductivity in the x direction. Therefore, the term average conductivity (cf. Eq. (9) in [48])

$$\sigma_{\mathrm{g}} = \sigma(I_1 + I_2) \sqrt{1 - A_{\mathrm{pga}}^2}, \tag{2.11}$$

is used, where $A_{\mathrm{pga}} = 2\varphi\gamma_0\gamma\sqrt{I_1 I_2}/(I_1 + I_2)$ is the photocarrier grating amplitude with $\gamma = 1/\left(1 + (2\pi L_{\mathrm{amb}}/\Lambda)^2 \right)$, and $0.5 < \varphi < 1$ is the photoconductivity dependence on the generation rate. In the coherent case, the photocurrent signal measured by a lock-in amplifier, is proportional to $\sigma_{\mathrm{g}} - \sigma(I_1)$, then the measurement is repeated for the incoherent case where the measured signal is proportional to $\sigma(I_1 + I_2) - \sigma(I_1)$. The ratio between the two abovementioned signals is defined as

$$\beta = \frac{\sigma_{\mathrm{g}} - \sigma(I_1)}{\sigma(I_1 + I_2) - \sigma(I_1)}, \tag{2.12}$$
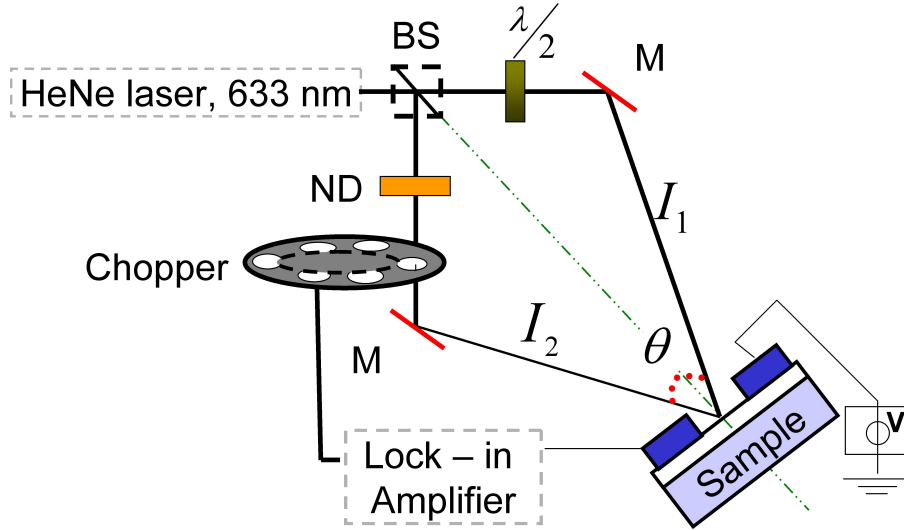
Fig. 2.8: Experimental setup for measuring the ambipolar diffusion length L_{amb} in SSPG. The HeNe laser beam, at $\lambda = 633$ nm, is split by means of a beam splitter BS and made to coincide on the sample by two mirrors M. The intensity I_2 of beam 2 is attenuated by a neutral density filter ND and chopped. The half-wave plate $\lambda/2$ rotates the polarization of beam 1. The lock-in amplifier measures the small changes in the photocurrent due to the chopping of I_2.

where $\sigma(I_1)$ and $\sigma(I_1)$ are the photoconductivities due to I_1 and I_2, respectively. Substituting Eq. (2.11) in Eq. (2.12) and assuming that $I_2 \ll I_1$, results in

$$\beta = -2\left(\varphi\gamma_0\gamma\right)^2, \tag{2.13}$$

$$= -2\frac{Q}{1 + (2\pi L_{\mathrm{amb}}/\Lambda)^2} + 1, \tag{2.14}$$

where $Q = \varphi\gamma_0$ is called grating "quality factor" (in contrast to $Q = \varphi\gamma_0^2$ as calculated from [48]). The ambipolar diffusion length L_{amb} is deduced by fitting β in Eq. (2.14) versus Λ which is changed by varying the angle θ. Fig. 2.9 shows the dependence of β on the grating period Λ. β is close to unity for L_{amb} much longer than the grating period Λ [49]. This is the case in which the diffusion blurs the grating and the signal is the same; whether I_1 and I_2 interfere and create grating or not. At the other extreme, if the diffusion length L_{amb} is much shorter than the grating period Λ, the carrier grating will sustain and β becomes negative.
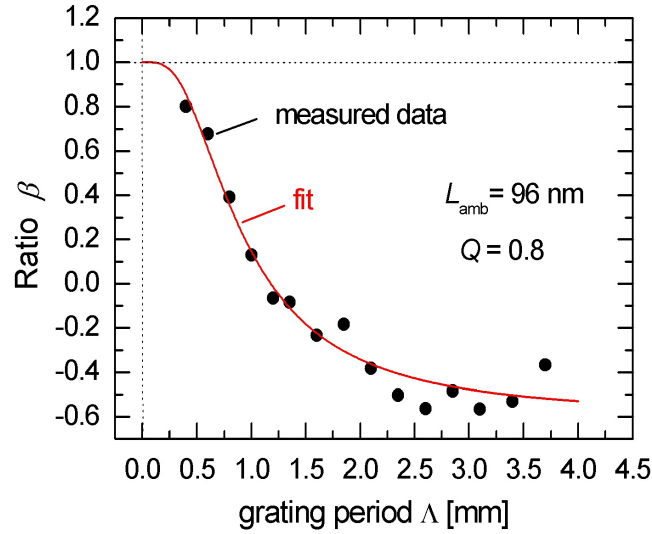
Fig. 2.9: Ratio β versus grating period Λ. The fit (solid line) of the measured data for an a-Si:H sample (closed circles) according to Eq. (2.14) results in a diffusion length L_{amb} and grating quality factor Q of 96 nm and 0.8, respectively.

Mechanical properties of plastic substrates

Amorphous silicon films can be deposited at low deposition temperatures. Therefore, the use of inexpensive flexible substrates for the a-Si:H solar cells could expand their field of applications. In this subsection, I present a comparison between the properties of amorphous polyethylene terephtalate (PET) and polyethylene naphtalene (PEN) foils. This comparison is summarized in Tab. 2.1 where it is clear that the PEN films have the advantage that they have a higher heat resistance than those of PET films. Also, PEN films have higher impermeability of gasses and water than of PET films. Therefore, the choice of PEN films for solar cells' application has to be taken into account.

The mismatch of thermal expansion coefficient between the a-Si:H films and the polymer substrates causes a high mechanical stress in the substrates after depositing a-Si:H films on those substrates. The most important parameters which determine the mechanics of the film structure are the elastic constants, i.e. Young's moduli Y_s, Y_f, and the thicknesses d_s, d_f of the substrate and the a-Si:H film itself, respectively, [52]. In the case where glass is the substrate, i.e. $Y_f d_f \ll Y_s d_s$, the stress in the substrate is small, the resulting curvature is very small and has a cylindrical shape

Tab. 2.1: Comparison between the properties of PET and PEN substrates [51].

Property	PET	PEN
Glass transition temperature [°C]	75	121
Tensile strength [kg mm^{-2}]	45	60
Oxygen permeation [rate]	5	1
Carbon dioxide permeation [rate]	5	1
Water vapor transmission [rate]	4	1
Water vapor transmission [°C]	260	269

and the bending radius R is given by

$$
R = \frac{d_\mathrm{s}\left[1 - \frac{Y_\mathrm{f}^*}{Y_\mathrm{s}^*}\left(\frac{d_\mathrm{f}}{d_\mathrm{s}}\right)^2\right]^2 + 4\frac{Y_\mathrm{f}^*}{Y_\mathrm{s}^*}\frac{d_\mathrm{f}}{d_\mathrm{s}}\left(1 + \frac{d_\mathrm{f}}{d_\mathrm{s}}\right)^2}{6\frac{Y_\mathrm{f}^*}{Y_\mathrm{s}^*}\frac{d_\mathrm{f}}{d_\mathrm{s}}\left[(\alpha_\mathrm{f} - \alpha_\mathrm{s})\Delta T + \varepsilon_\mathrm{bi}\right]\left(1 + \frac{d_\mathrm{f}}{d_\mathrm{s}}\right)}, \tag{2.15}
$$

where $Y_\mathrm{f}^* = Y_\mathrm{f}/(1 - \nu_\mathrm{f})$ and $Y_\mathrm{s}^* = Y_\mathrm{f}/(1 - \nu_\mathrm{s})$ are the biaxial strain moduli of the film and the substrate, respectively, and ν_f, ν_s are the corresponding Poisson ratios. ΔT is the difference between the deposition temperature T_dep and the ambient temperature. The mismatch strain ε_bi between the film and the substrate has two components [53]

(i) the difference in the thermal expansion coefficients $\alpha_\mathrm{f} - \alpha_\mathrm{s}$ of the film and of the substrate itself,

(ii) the built-in strain ε_bi in the deposited film.

The sign of the radius R of the substrate in Eq. (2.15) indicates the curvature of the substrate. If the film is under compression, i.e. $\alpha_\mathrm{f} < \alpha_\mathrm{s}$, the substrate will have a convex shape and R is negative, if the film is under tension, i.e. $\alpha_\mathrm{f} > \alpha_\mathrm{s}$, the substrate will have a concave shape and then R is positive.

In the case where the flexible foil is the substrate, the product of elastic modulus and thickness $Y_\mathrm{f}d_\mathrm{f}$ of the film becomes comparable to $Y_\mathrm{s}d_\mathrm{s}$ of the substrate. Therefore, the structure rolls into a cylinder instead of forming a spherical cap [53] and the structure rises to have a complicated situation resulting in an another formula of calculating the radius R [52] as

$$R = \frac{d_{\text{s}}}{6\frac{Y_{\text{f}}^*}{Y_s^*}\frac{d_{\text{f}}}{d_s}\left[(\alpha_{\text{f}} - \alpha_{\text{s}})\,\Delta T + \varepsilon_{\text{bi}}\right]} \frac{\delta_1\delta_2 + \delta_3 + \delta_4}{\delta_5}, \tag{2.16}$$

where the variables $\delta_{[1-5]}$ are defined as

$$\delta_1 = \left[1 - \frac{Y_f^*}{Y_s^*}\left(\frac{d_f}{d_s}\right)^2\right]^2 + 4\frac{Y_f^*}{Y_s^*}\frac{d_f}{d_s}\left(1 + \frac{d_f}{d_s}\right)^2 \tag{2.17}$$

$$\delta_2 = (1 - \nu_s^2) + \left(\frac{Y_f^*}{Y_s^*}\frac{d_f}{d_s}\right)^2(1 - \nu_f^2) \tag{2.18}$$

$$\delta_3 = 3\left(\frac{Y_f^*}{Y_s^*}\frac{d_f}{d_s}\right)^2\left(1 + \frac{d_f}{d_s}\right)^2\left[(1 - \nu_s^2) + (1 - \nu_f^2)\right] \tag{2.19}$$

$$\delta_4 = 2\frac{Y_f^*}{Y_s^*}\frac{d_f}{d_s}(1 - \nu_s\nu_f)\left(1 + \frac{Y_f^*}{Y_s^*}\frac{d_f}{d_s}\right)\left(1 + \frac{Y_f^*}{Y_s^*}\left(\frac{d_f}{d_s}\right)^3\right) \tag{2.20}$$

$$\delta_5 = \left(1 + \frac{d_f}{d_s}\right)\left(1 + \frac{Y_f^*}{Y_s^*}\frac{d_f}{d_s}\right)\left((1 - \nu_s^2)(1 + \nu_f) + \frac{Y_f^*}{Y_s^*}\frac{d_f}{d_s}(1 - \nu_f^2)(1 + \nu_s)\right) \tag{2.21}$$

If the poisson ratios ν_{s} and ν_{f} of the substrate and the films are equal, Eq. (2.16) is rewritten as

$$R = \frac{d_{\text{s}}\left[1 - \frac{Y_{\text{f}}}{Y_{\text{s}}}\left(\frac{d_{\text{f}}}{d_{\text{s}}}\right)^2\right]^2 + 4\frac{Y_{\text{f}}}{Y_{\text{s}}}\frac{d_{\text{f}}}{d_{\text{s}}}\left(1 + \frac{d_{\text{f}}}{d_{\text{s}}}\right)^2}{6\frac{Y_{\text{f}}}{Y_{\text{s}}}\frac{d_{\text{f}}}{d_{\text{s}}}\left[(\alpha_{\text{f}} - \alpha_{\text{s}})\,\Delta T + \varepsilon_{\text{bi}}\right]\left(1 + \frac{d_{\text{f}}}{d_{\text{s}}}\right)(1 + \nu)} \tag{2.22}$$

Tab. 2.2 shows the mechanical parameters of the substrates and of the films used in my work. I applied these parameters into Eq. (2.22) to simulate the effect of the film thickness d_{f} on the resulting radius R of the substrates after depositing a-Si:H films on them.

Tab. 2.2: Mechanical properties of PET ($d_\mathrm{s} = 25\ \mu$m) and PEN ($d_\mathrm{s} = 25\ \mu$m) substrates and a-Si:H films needed to calculate the curvature of the substrates after the deposition of a-Si:H films.

parameter	PET substrate	PEN substrate	a-Si:H film
$Y_\mathrm{f,s}$	5×10^9 [N/m^2]	6.08×10^9 [N/m^2]	10×10^{11} [N/m^2]
$\alpha_\mathrm{f,s}$	15×10^{-6} [1/°C]	13×10^{-6} [1/°C]	4×10^{-6} [1/°C]
$\nu_\mathrm{f,s}$	0.22	0.22	0.22

Fig. 2.10 shows that on the one side, the decrease of the thickness d_f of an a-Si:H film increases the resulting radius R of the substrate. On the other side, this calculation of R for both PEN and PET substrates shows that the PEN substrates tend to have larger values of radius R than the PET ones.
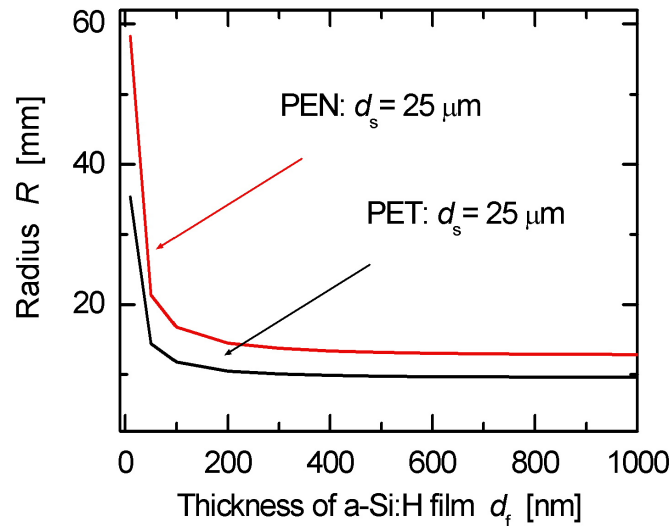

Fig. 2.10: Calculated radius R of the PET and PEN substrates, using Eq. (2.22), as function of thickness d_f of a-Si:H films. This simulation shows that the PEN substrates show larger values of radius R than of PET substrates indicating that the bending of PEN substrates is lower than of the PET substrates.

2.3.2   Cell characterization

This subsection reviews the standard measurement techniques allowing to characterize the performance of a-Si:H solar cells. The characterization techniques of a-Si:H solar cells relevant to my work are the current density/voltage (J/V) characteristics and the quantum efficiency QE.

Current density/voltage (J/V) characteristics

Current density/voltage (J/V) characteristic measurement is a primary characterization tool for a-Si:H solar cells to determine their conversion efficiencies [54–56]. To describe the electrical behaviour of a-Si:H solar cells, it is of importance to use their equivalent circuit. Fig. 2.11 shows the equivalent circuit generally used for solar cells in the presence of the parasitic resistances; series R_s and parallel R_p to describe the real solar cell behaviour. The equivalent circuit consists of a current source J_ph (generation of photocurrent) shunted by a diode (loss of photocurrent) with additional series and parallel resistances. In addition to this common representation of ohmic losses, I add an additional voltage dependent loss term (dashed line) to take into account voltage dependent recombination losses in the intrinsic layer of a-Si:H solar cells [57].
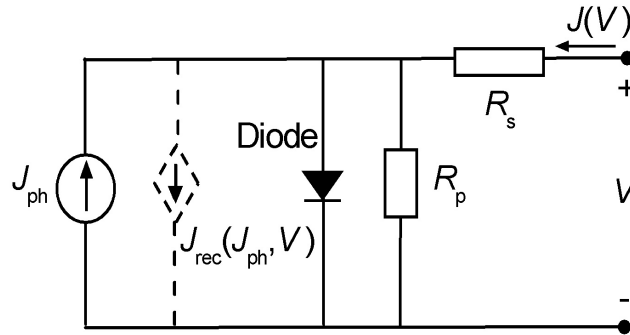
Fig. 2.11: An equivalent circuit for a-Si:H solar cells, with incorporating series R_s and parallel R_p resistances. The additional current sink (dashed lines) takes into account the current losses due to the voltage dependent recombination in the intrinsic layer of the a-Si:H solar cells.

From the equivalent circuit in Fig. 2.11, the J/V-characteristics of a-Si:H solar cells is given by

$$J(V) = J_0 \left\{ \exp\left(\frac{V - JR_\mathrm{s}}{n_\mathrm{id} V_\mathrm{t}} \right) - 1 \right\} + \frac{V - JR_\mathrm{s}}{R_\mathrm{p}} + J_\mathrm{rec}(J_\mathrm{ph}, V) - J_\mathrm{ph}, \qquad (2.23)$$

where J_0 is the reverse saturation current density, n_{id} is the diode quality factor and $V_t = kT/q$ is the thermal voltage which is equal to 25.9 meV at room temperature. The recombination current density $J_{rec}(J_{ph}, V)$ [50] is described as

$$J_{rec}(J_{ph}, V) = \frac{J_{ph} d_i^2}{\mu\tau (V_{bi} - V + JR_s)}, \tag{2.24}$$

where the product $\mu\tau$ represents the mobility and the recombination time of the photogenerated carriers, d_i is the thickness of the intrinsic layer, V_{bi} is the built-in voltage.

The setups of the current density/voltage (J/V) characteristics which I use throughout my work are two different types, depending on the presence of light source from one side and the contacting of solar cell on the other side. For a-Si:H solar cells with *n-i-p* deposition sequence on opaque substrates, both front and back contacts face the incident light, I use the J/V-setup built for CIGS solar cells where the light source is a single tungsten-halogen projector lamp (ELH type, 300 W, 120 V) [58].

For cells deposited in *p-i-n* sequence, the light enters through the transparent superstrates, and the contacts are only accessible from the back of the solar cells (in the direction of the incident light). For the *p-i-n* cells, I use the J/V-setup of a-Si:H solar cells where the light source is two halogen lamps, each of 100 W, 12 V, and one metal vapor lamp (1000 W). Fig. 2.12 shows a comparison of the spectra of ELH lamp, used as an artificial solar simulator for CIGS solar cells, and of the lamps used in the J/V-setup for a-Si:H solar cells.

The temperature of the measured a-Si:H solar cells in the J/V-setup of CIGS solar cells is kept constant with help of a large copper heat sink, just at the backside of the cells, cooled by a fan. In the case of the J/V-setup of a-Si:H solar cells, the light enters through a water-filled glass-box to keep the measured cells from being warmed since the water absorbs the infrared part of the light. Fig. 2.13 shows the spectral transmission of the glass-box (solid curve) used in the J/V-setup of a-Si:H solar cells. To enhance the transmission of the water-filled glass-box (dashed curve), about 5% of NaClO is added to the water which prevents any precipitate from being stuck at the insides of the box.

Due to the difference between the spectra of the CIGS and a-Si:H J/V-setups, I calibrate the J/V-characteristics of the a-Si:H solar cells measured in the CIGS J/V-setup by measuring their corresponding quantum efficiency which will be discussed in the next subsection. A typical J/V-characteristics (solid curve) of an a-Si:H solar
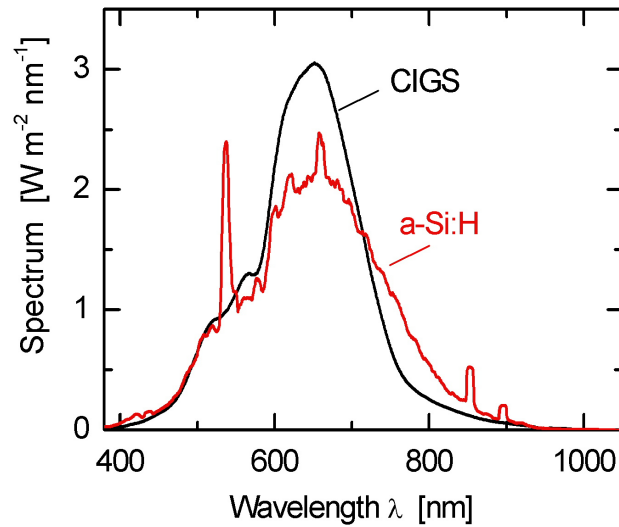
Fig. 2.12: Comparison of the spectra of ELH lamp, used as an artificial solar simulator for CIGS solar cells, and of the lamps used as artificial solar simulators for the J/V-setup of a-Si:H solar cells.
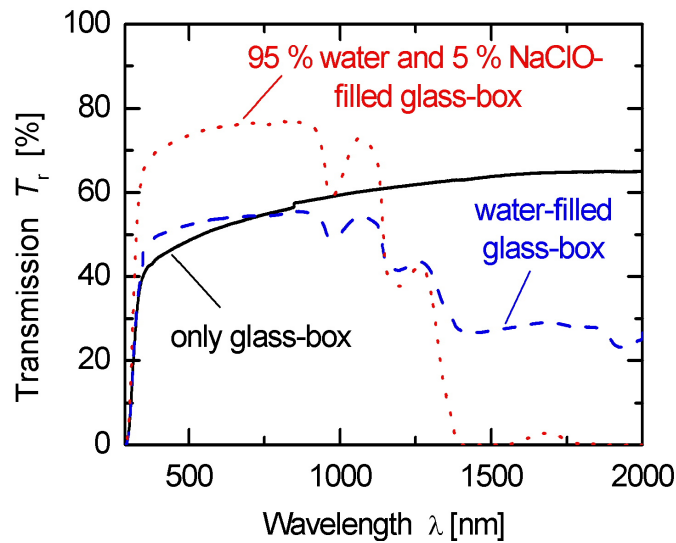
Fig. 2.13: Spectral transmission of the glass-box (solid curve) used in the J/V-setup of a-Si:H solar cells. Filling the box with water reduces the transmission in the infrared region (dashed curve). To remove any precipitate from being stuck at the insides of the box, about 5% of NaClO is added to the water, therefore the transmission is enhanced.

cell is shown in Fig. 2.14.
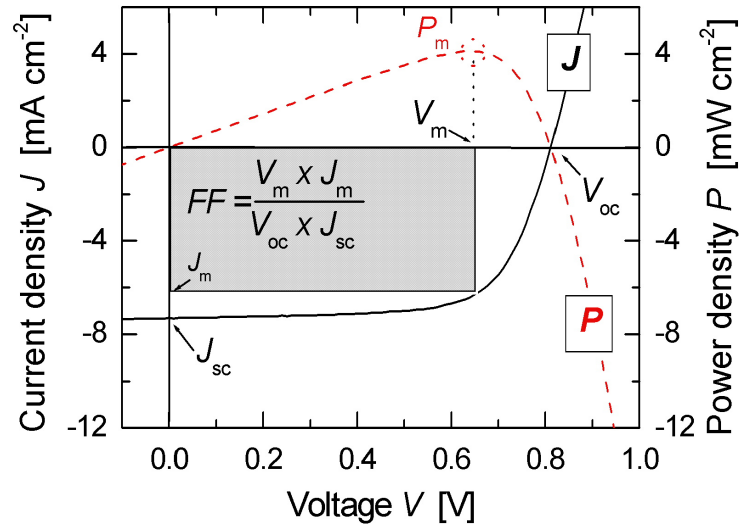
Fig. 2.14: An example of the J/V-characteristics (solid curve) and power density P (dashed curve) of an a-Si:H solar cell (sample AnM060331-1) of an area of $A = 0.33$ cm^2. The figure demonstrates the definitions of the open-circuit voltage V_{oc} and the short-circuit current J_{sc}. The value of $V_m J_m$ denotes the maximum power output $P_m = V_m J_m$.

The electrical performance of this cell (sample AnM060331-1) is characterized by

- The short-circuit current density J_{sc} is the current density which is produced by the solar cell if it is connected to a very small resistance. In this work, I use the current density J instead of the current I itself in order to normalize the effect of the solar cell area A which is equal to 0.33 cm^2 in this example. A high short-circuit current density J_{sc} requires a good material quality and an optimal design of the cell to absorb and trap as many incident photons as possible.

- The open-circuit voltage V_{oc} is the voltage which is built up across the solar cell if it is connected to a very large resistance. A high open-circuit voltage V_{oc} requires: efficient doping in the p- and n-layers, a high band gap and also good interfaces.

- The fill factor FF represents the curvature of the J/V-characteristics. FF is defined as the ratio between the maximum power output $P_m = V_m J_m$ and the

product $V_{oc}J_{sc}$. A high fill factor FF requires: low loss of the photogenerated carriers in the intrinsic layer and at the interfaces, strong electric field in the intrinsic layer and also good ohmic contacts.

- The efficiency η is defined by the three previous parameters as

$$\eta = \frac{J_{sc}V_{oc}FF}{\Phi}, \qquad (2.25)$$

where Φ is the intensity of the incoming light.

Quantum efficiency QE

The quantum efficiency QE defines the probability that an incident photon with an energy $h\nu$ contributes with one electron-hole pair to the photocurrent. This characterization technique contains valuable information about the collection losses of the solar cell. The photons that have energies much larger than the band gap of the absorber layer of the a-Si:H cell $h\nu >> E_g$ (blue photons) are absorbed near to its surface, whereas the photons which have $h\nu \leq E_g$ (red photons) penetrate through the absorber layer. Therefore, one gets an information about the front and back sides of the cell. Fig. 2.15 shows a typical quantum efficiency measurement of a-Si:H solar cell (solid curve) and also the ideal quantum efficiency (dashed line), i.e. being unity at photon wavelengths above the band gap (at $\lambda \leq 730$ nm), and zero at wavelengths below (i.e. at $\lambda \geq 730$ nm). The filled area in Fig. 2.15 represents the losses in this a-Si:H solar cell. Therefore, the quantum efficiency of a-Si:H solar cells gives key information about the optical and electrical losses in the device structure.

The quantum efficiency also serves to determine the short-circuit current density J_{sc} in the absorber layer of a-Si:H solar cells [59] as

$$J_{sc} = q \int_{\lambda_{min}}^{\lambda_{max}} QE(\lambda)\Phi(\lambda)\frac{\lambda}{hc}d\lambda, \qquad (2.26)$$

where λ/hc is the inverse of the energy carried by a photon of wavelength λ. The value of J at $V = 0$ of the J/V-characteristics should be equal to the value of J_{sc} of Eq. (2.26), i.e. the J/V-characteristics of solar cells can be cross-checked by quantum efficiency measurements.
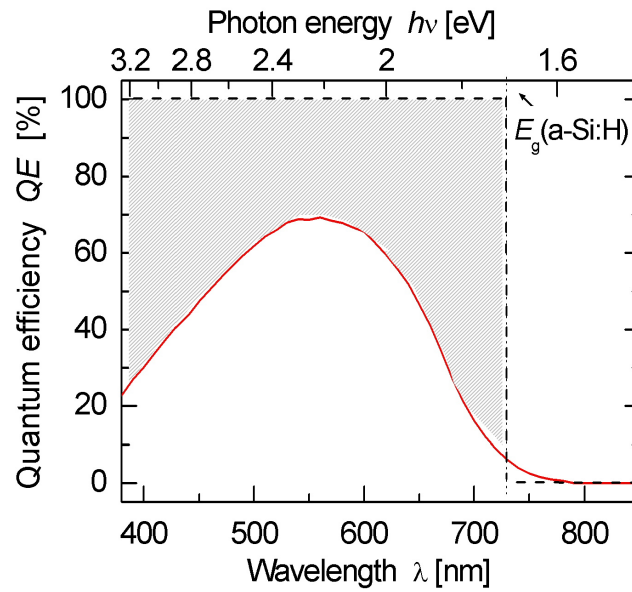
Fig. 2.15: An example of the quantum efficiency QE of an a-Si:H solar cell. In the ideal case, the quantum efficiency is a step-like function, i.e. being unity at photon wavelengths above the band gap (at $\lambda \leq 730$ nm), and zero at wavelengths below (i.e. at $\lambda \geq 730$ nm). The filled area represents the losses in a-Si:H solar cells.

2.4 Description of *p-i-n* solar cells

2.4.1 Numerical modelling

For numerical modelling of a-Si:H solar cells, I use a comprehensive simulation program called Amorphous Semiconductor Analysis (ASA), which has been developed at Delft University of Technology [60, 61] in order to gain a better understanding of these devices. This program is a one-dimension of steady-state device simulator, based on the solution of Poisson equation and the continuity equations which are discretized according to the integral expressions of Gummel [62]. The resulting set of equations is solved by a fully coupled Newton iteration method.

The main features of the ASA program include:

(i) separate calculation of the light induced charge carrier generation profile, which is based on the thin film optics assuming flat interfaces in the device,

(ii) models describing a complete density of states distribution as function of energy, which include both the extended and localized (tail and defect) states with corresponding recombination-generation statistics,

(iii) calculation of the defect state distribution in a layer according to the defect-pool models (DPM) [63, 64].

The ASA program incorporates optical and electrical modelling based on thin film optics and a set of basic semiconductor equations. Optical modelling is important to determine the generation rate of the generated carriers. Therefore, the refractive index n_{rix} and the extinction coefficient κ as a function of wavelength λ are required. The optical modelling is applied for all defined layers of the solar cell.

Electrical modelling parameters are required to describe the properties of the semiconductor layers. These parameters include the mobility gap E_{opt}, the activation energy E_{act} and the mobilities of electrons/holes $\mu_{\text{e/h}}$. The electrical modelling calculates the recombination rate in a-Si:H solar cells applying various models [65].

By the ASA program, several characteristics of a-Si:H solar cells can be simulated; such as dark and illuminated current density/voltage (J/V) characteristics and quantum efficiency QE.

2.4.2 Analytical description

Crandall's model

In Crandall's approach [66], a model for *p-i-n* solar cells was derived, and simple relations between the short-circuit current and material properties were established. However, this model does not hold for the whole range of the J/V-characteristics because it does not take into account the diffusion currents. Therefore, it is not accurate for the calculation of the open-circuit voltage of *p-i-n* solar cells.

Taretto's model

Taretto et. al. [67] obtained a general analytical expression for the J/V-characteristics in p-i-n solar cells by solving the continuity equations considering drift and diffusion. The main physical simplifications assumed within Taretto's model are: i) the electric field in the intrinsic layer is uniform, ii) the photogeneration rate is homogeneous within the *i*-layer, and iii) the carrier mobilities μ and lifetimes τ have the same values for electrons and holes.

2.5   *p-i-n* and *n-i-p* amorphous silicon solar cells

The a-Si:H solar cells have two configurations depending on their deposition sequence; superstrate and substrate designs. In the superstrate design, also called *p-i-n* configuration, the *p*-layer is first deposited onto transparent conducting oxide (TCO) coated transparent superstrates such as glass, polyethylene terephthalate (PET), polyethylene naphthalate (PEN) and polyimide (PI), which serve as a window to the cell. Then, the *i*-layer, followed by the *n*-layer, and a final back-contact, as shown in Fig. 2.5a.

In the substrate design, or n-i-p configuration, the first a-Si:H layer is the *n*-layer deposited on electrically conductive back-contact on cheap superstrates such as Al-coated substrates (glass, PET, PEN, PI, and special fabrics). The *i*-layer is deposited and then followed by the deposition of the *p*-layer and a final transparent front contact (TCO$^{(2)}$), see Fig. 2.5b. The insertion of the TCO$^{(1)}$ between the Al-coated substrate and the *n*-layer is used because I have not had any working n-i-p solar cell without this inserting this TCO because the fill factor was below 30 %, more details are in [69]. The layer thicknesses of both configurations are summarized in Tab. 2.3.

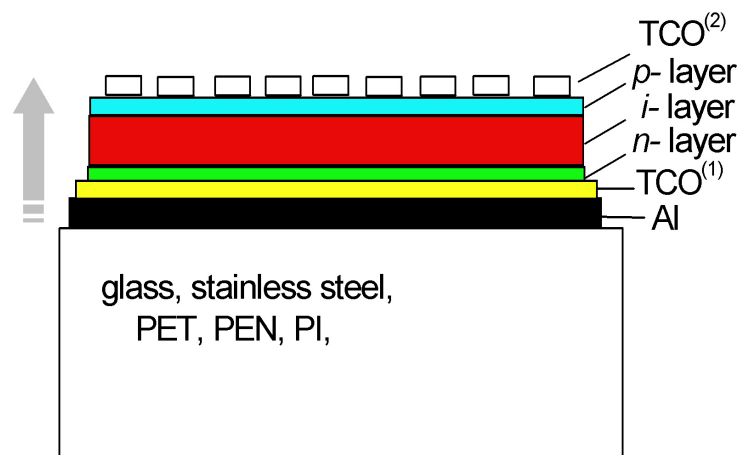**Tab. 2.3:** Typical thicknesses of *p-i-n* and *n-i-p* solar cells.

Film type	Thickness [nm]
TCO, TCO$^{(2)}$	500-800
p-layer	15
i-layer	250
n-layer	20
TCO$^{(1)}$	50
Al	500

The n-i-p configuration has an advantage in that the band gap of the intrinsic layer can be increased by gradually reducing the deposition temperature [25] in order to adjust the band gap profile. A second advantage of this configuration is that the *p*-layer is the last deposited layer. In this case, the *p/i*-interface, which is very important in determining the performance of a-Si:H solar cells [70, 71], is not exposed to subsequent plasmas combined with elevated deposition temperatures.

In both configurations, the light enters the cells through the *p*-layer for two reasons: i) the fact that most of the incident light Φ_0 is absorbed close to the surface

Al
n- layer
i- layer
p- layer
TCO

Deposition sequence

glass, PET, PEN, PI

(b)

TCO$^{(2)}$
p- layer
i- layer
n- layer
TCO$^{(1)}$
Al

glass, stainless steel,
PET, PEN, PI,
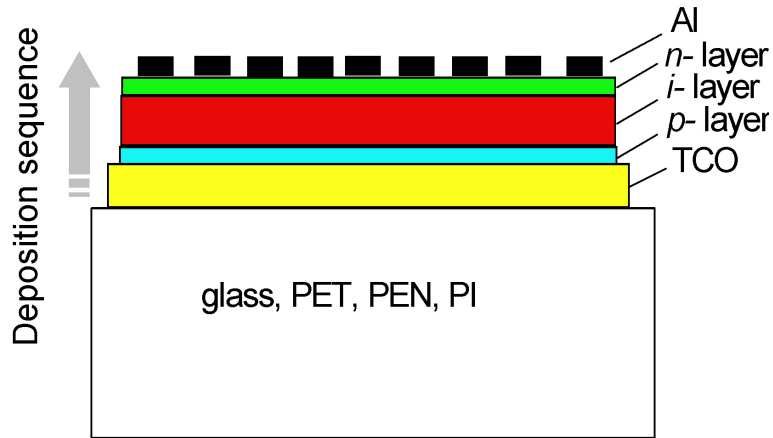
(b)

Fig. 2.16: *p-i-n* a-Si:H solar cell (superstrate design), where the first a-Si:H deposited layer is the *p*-layer, a) and *n-i-p* a-Si:H solar cell (substrate design), where the first deposited a-Si:H layer is the *n*-layer, b). Both configurations have the same working principle and also the light penetrates both of them through the *p*-layer.

of the illuminated layer following the Beer's law, where the intensity of the light decreases with distances exponentially in materials, and generates electron-hole pairs there, and ii) the lower mobility carriers (holes) have to be efficiently collected by the p-layer before they recombine with other electrons [7]. The collection of the electrons is not so critical as of the holes since the electrons have higher mobilities μ_n and life times τ_n than of holes, $\mu_n\tau_n > 50\mu_p\tau_p$ [76], and they are more capable to be collected by the n-layer. The electric field generated between the p- and the n-layers is responsible for the collection of the generated carriers in the i-layer. In other words, to collect most the generated holes efficiently, they have to have a short collection path.

Chapter 3

Results

3.1 Novel analytical modelling of amorphous silicon solar cells

In this section, I present a novel analytical expression for the current density/ voltage (J/V) characteristics of a-Si:H solar cells to demonstrate the dependency between the physical parameters and the output characteristics of the solar cells. In this model, I extend the existing analytical models of the J/V-characteristics in order to have a more realistic description of p-i-n-type solar cells. This novel model solves the continuity equations of electrons and holes at every position within the intrinsic i-layer. It allows for different mobilities μ_n, μ_p and different lifetimes τ_n, τ_p for electrons and holes, and applies a photogeneration rate $G(\lambda)$ as a function of wavelength λ. The basic idea of this model is the solution of the transport equations in two different parts of the cell. In each part, I first solve the continuity equations for the minority carriers, and then enter this solution into the equations for majority carriers, which are solved subsequently. The solution of the two second order differential equations in the two different regions altogether with the boundary conditions yields a set of eight algebraic equations. These equations are finally solved with a Jacobian matrix inversion. Thus, I obtain an analytical solution of the problem.

3.1.1 Model

Outline

My model considers the *p*-*i*-*n* structure of a-Si:H solar cells, with two highly doped
(*p*- and *n*-) layers that are photovoltaically inactive. Electron/hole pairs photogen-
erated in one of those layers do not contribute to the short-circuit current of the
solar cell [68]. Therefore, my calculations are restricted to the *i*-layer of the solar
cell.

The main physical simplification assumed within my model is that the *i*-layer has
a negligible concentration of charged impurities, therefore the electric field F within
the *i*-layer is spatially uniform [68, 75]. This assumption also helps to analytically
solve the continuity equations of the carriers by defining the electric field as

$$|F| = \left| \frac{V - V_{\mathrm{bi}}}{W} \right|, \tag{3.1}$$

i.e., the electric field F depends only on the applied voltage V and on the thickness
W of the *i*-layer, where V_{bi} is the built-in voltage.

Assumptions

This model takes into account the following physical assumptions:

(i) The photogeneration rate $G(x, \lambda) = \alpha(\lambda) N_{\mathrm{ph}}(\lambda) \exp(-\alpha(\lambda)x)$ depends on
the wavelength λ of the solar spectrum and the position x within the *i*-layer
as illustrated in Fig. 3.1. This assumption accounts for the large absorption
coefficient $\alpha(\lambda)$ of amorphous silicon based films in the blue region of the
AM1.5 spectrum $N_{\mathrm{ph}}(\lambda)$.

The condition of a constant photogeneration rate is only assumed if the thick-
ness W of the *i*-layer is smaller than the absorption length $L_\alpha = 1/\alpha(\lambda)$ [68]
as in region B of Fig. 3.2 while the generation rate is not constant in region
A where $W > L_\alpha$.

(ii) The back reflection R_{ref} at the back contact is taken into account. In thin
films, where the whole spectrum is not absorbed within the *i*-layer, the current
generated due to the absorption of the reflected photons at the back contact
has to be considered. In this case $G(x, \lambda)$ is written as
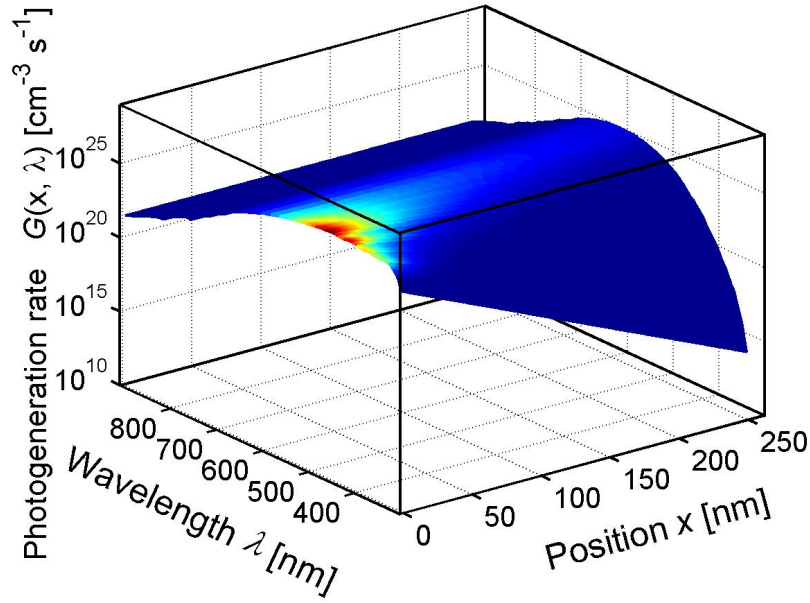
Fig. 3.1: Photogeneration rate $G(x, \lambda)$ of an a-Si:H solar cell used in solving the continuity equations of electrons and holes. It is clear that $G(x, \lambda)$ depends on both the position within the absorber layer (Lambert-Beer's model) and on the wavelength λ of the photons especially for low values of λ because of the high absorbance of a-Si:H-based materials in this region of wavelengths.

$$G(x, \lambda) = \quad \alpha(\lambda) N_{\text{ph}}(\lambda) e^{-\alpha(\lambda)x} \left[1 + R_{\text{ref}} e^{-2\alpha(\lambda)[W + d_n - x]} \right], \qquad (3.2)$$

where W, d_{n} are the thicknesses of the i- and n-layers, assuming without loss of generality that the cell is illuminated through the p-layer. The contribution of the back reflection is represented in the second part of the square brackets in Eq. (3.2).

(iii) The carrier mobilities μ_{n}, μ_{p} and lifetimes τ_n, τ_p of electrons and holes do not have the same values, typically in amorphous silicon based materials, $\mu_{\text{n}}\tau_{\text{n}} > 50 \, \mu_{\text{p}}\tau_{\text{p}}$ [76],

(iv) The doping concentrations of the doped p- and n-layers should not have the same values. This assumption is applied due to the application of μc-Si:H p-layers in a-Si:H solar cells [102] where the active doping increases due to the crystallinity of the μc-Si:H films.
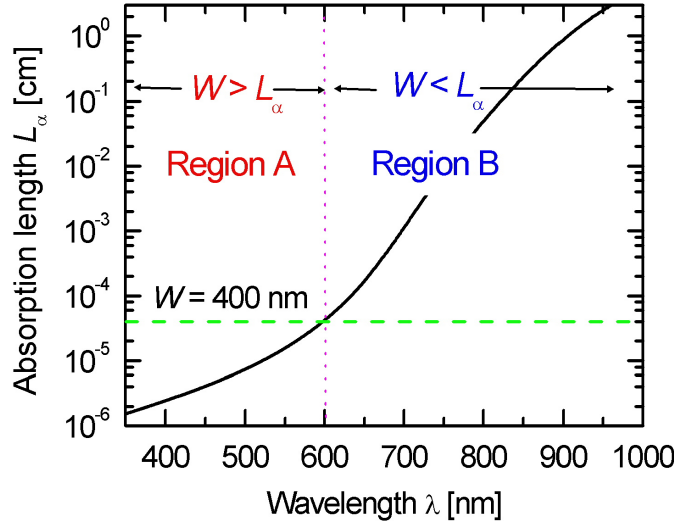
Fig. 3.2: Absorption length $L_\alpha(\lambda)$ of an a-Si:H solar cell. The Photogeneration rate $G(x,\lambda)$ is only approximated to be constant in region B, while in region A it is not. The application of a constant photogeneration rate over the complete spectrum of light is not accurate for high-absorbing films.

Fig. 3.3 shows the band diagram of *p-i-n* type a-Si:H solar cell where both the *p*- and *n*-layers are much thinner than the *i*-layer. Under thermal equilibrium, the electron concentration n_{p0} in the *p*−layer is given by $n_{p0} = n_i^2/N_A$ and the hole concentration p_{nw} in the *n*-layer is given by $p_{nw} = n_i^2/N_D$, where n_i is the intrinsic concentration of the given semiconductor and is equal to 1.88×10^7 cm^{-3} for a-Si:H [77]. N_A and N_D are the effective doping densities of the *p*- and *n*-layers, respectively.

Under equilibrium conditions, the quasi-Fermi levels E_{Fn} and E_{Fp} of electrons and holes are equal and constant throughout the device, and therefore no current flows. Under non-equilibrium conditions (e.g. applied voltage), the quasi-Fermi levels E_{Fn} and E_{Fp} of electrons and holes shift away from the intrinsic Fermi level depending on the applied voltage V. The energy difference between $E_{Fn}(W)$ and $E_{Fp}(0)$ equals qV. The generated built-in voltage V_{bi} represents the energy difference between the *p*- and *n*-layers, i.e. it is produced due to the difference in the doping of the doped layers and equals $V_t \ln(N_A N_D/n_i^2)$ where $V_t = kT/q$ is the thermal voltage, k is the Boltzmann constant, T is the absolute temperature, and q is the elementary charge.
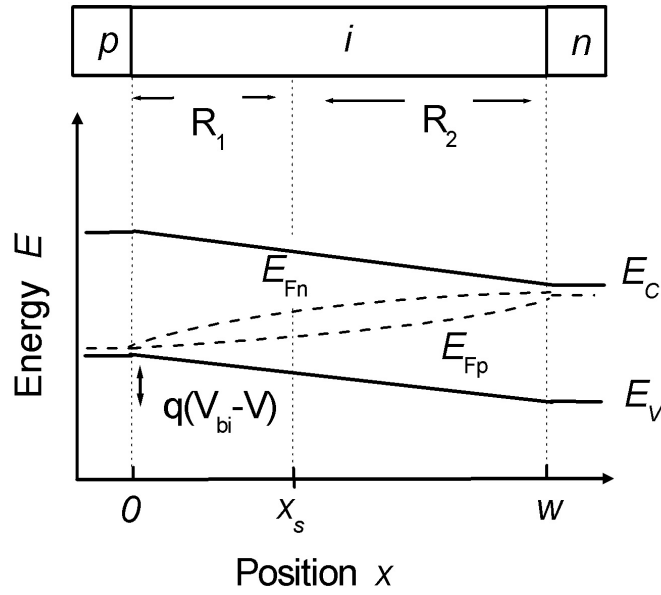
Fig. 3.3: Sketch of the *p-i-n* structure under forward bias voltage V. The energy difference between the quasi-Fermi levels (dashed lines) $E_{\mathrm{Fn}}(W)$ and $E_{\mathrm{Fp}}(0)$ of electrons and holes equals the quantity qV which reduces the energy difference between the *p-* and *n*-layers. The generated built-in voltage V_{bi} represents the energy difference between the *p-* and *n*-layers.

Carrier concentration

Taretto et. al. [67] solved the continuity equations [78–80] for one type of carriers in the corresponding region of the minority carriers, i.e. for electrons $n(x)$ in region R_1 and then assumed the symmetry for the holes $p(x)$ in region R_2 shown in Fig. 3.3. In this subsection, I apply non-equal values of carrier mobilities μ_{n} and μ_{p}, lifetimes τ_{n} and τ_{p} for electrons and holes, respectively. Therefore, I solve the continuity equations for both types of carriers in both regions R_1 and R_2 of the *i*-layer.

The basic idea for solving the coupled continuity equations for electrons and holes is the separation of the *i*-layer into two regions where either electrons or holes are the minority carriers. The recombination rate R_r in region R_1 of Fig. 3.3, where electrons are minority carriers, is determined by the lifetime τ_{n} of electrons, i.e. $R_{\mathrm{r}} = (n - n_0)/\tau_{\mathrm{n}}$. Thus, the continuity equations in region R_1 read

$$\mu_{\mathrm{n}} F \frac{dn(x)}{dx} + D_{\mathrm{n}} \frac{d^2 n(x)}{dx^2} = \frac{n(x) - n_0(x)}{\tau_{\mathrm{n}}} - G(x), \tag{3.3}$$

and

$$\mu_{\mathrm{p}} F \frac{dp(x)}{dx} - D_{\mathrm{p}} \frac{d^2 p(x)}{dx^2} = -\frac{n(x) - n_0(x)}{\tau_{\mathrm{n}}} + G(x). \tag{3.4}$$

The fact that Eq. (3.3) only depends on the electron density $n(x)$, allows us to solve Eq. (3.3) first. Then, I apply the solution of Eq. (3.3) into Eq. (3.4) and solve for $p(x)$. Therefore, I determine the electron J_{n} and hole J_{p} currents in region R_1.

I apply the last principle for the calculation of the electron J_{n} and the hole J_{p} currents in region R_2 with the role of electrons and holes interchanged, i.e. by solving first for $p(x)$ and then for $n(x)$ in region R_2 where the continuity equations in this region read

$$\mu_{\mathrm{n}} F \frac{dn(x)}{dx} + D_{\mathrm{n}} \frac{d^2 n(x)}{dx^2} = \frac{p(x) - p_0(x)}{\tau_{\mathrm{p}}} - G(x), \tag{3.5}$$

and

$$\mu_{\mathrm{p}} F \frac{dp(x)}{dx} - D_{\mathrm{p}} \frac{d^2 p(x)}{dx^2} = -\frac{p(x) - p_0(x)}{\tau_{\mathrm{p}}} + G(x), \tag{3.6}$$

where D_{n}, D_{p} are the diffusion constants of electrons and holes, respectively. The photogeneration rate $G(x)$ is already defined in Eq. (3.2). The general solutions of Eqs. (3.5) and (3.6) are given in appendix 5.1.

Boundary conditions

The unique solution for the four second-order differential equations [Eqs. (3.3) - (3.6)] is defined by eight boundary conditions. The calculation of the eight coefficients determining the final solution is achieved by a matrix equation inversion. The final matrix equation is given in Appendix 5.2. The position $X = X_{\mathrm{s}}$ separates region R_1 and region R_2. Note that all the following equations are valid for arbitrary X_{s}. During the calculations, I start with $X_{\mathrm{s}} = W/2$. From the solution, I determine the position X_{c} where both carrier concentrations are equal and then repeat the calculation with $X_{\mathrm{s}} = X_{\mathrm{c}}$ to obtain the final result. The eight boundary conditions are defined as follows:

1. The carrier concentration $n(x)$ of electrons is continuous at position X_{s} (arbitrary position within the i-layer).

$$n(X_{\mathrm{s}})|_{R_1} = n(X_{\mathrm{s}})|_{R_2}. \tag{3.7}$$

2. The carrier concentration $p(x)$ of holes is also continuous at position X_s

$$p(X_s)|_{R_1} = p(X_s)|_{R_2}. \tag{3.8}$$

3. The carrier concentration of electrons is differentiable at position X_s

$$\frac{dn(x)}{dx}|_{X_s,R_1} = \frac{dn(x)}{dx}|_{X_s,R_2}. \tag{3.9}$$

4. The carrier concentration of holes is also differentiable at position X_s

$$\frac{dp(x)}{dx}|_{X_s,R_1} = \frac{dp(x)}{dx}|_{X_s,R_2}. \tag{3.10}$$

5. An extra-current due to interface recombination is present at the p/i interface ($x = 0$). With a surface recombination velocity S_n of the minority carriers (electrons) [81], the recombination current density at this interface is $qS_n(n|_{x=0} - n_{p0})$, where n_{p0} is the equilibrium-carrier density in the p-layer. The concentration of electrons $n|_{x=0}$ is calculated from

$$S_n(n|_{x=0} - n_{p0}) = \mu_n F n|_{x=0} + D_n \frac{dn}{dx}|_{x=0}. \tag{3.11}$$

6. An extra-current due to interface recombination is present at the i/n interface ($x = W$). With a surface recombination velocity S_p of the minority carriers (holes), the recombination current density at this interface is $qS_p(p|_{x=W} - p_{nw})$, where p_{nw} is the equilibrium-carrier density in the n-layer. The concentration of holes $p|_{x=W}$ is calculated from Eq. (3.12)

$$S_p(p|_{x=W} - p_{nw}) = \mu_p F p|_{x=W} - D_p \frac{dp}{dx}|_{x=W}. \tag{3.12}$$

Note that for majority carriers, the interfaces behave as ohmic contacts [82] and the corresponding surface recombination velocities are very high. Therefore, the majority carrier concentrations are independent of the current density, i.e.

$$n|_{x=W} = N_D, \tag{3.13}$$

and

$$p|_{x=0} = N_A. \tag{3.14}$$

Current density

Now, I express the whole system of differential equations in a matrix form in order to calculate the eight quantities C_1, C_2, ..., C_8 which are the coefficients needed to solve the carrier concentrations and their corresponding currents at each point within the i-layer by solving the matrices given in appendix 5.2. Since the photogeneration rate is a function of the wavelength λ, the photogenerated current is also a function of wavelength and has to be integrated over the solar spectrum while the dark current is of course independent of the illumination intensity and wavelength. The dark and the photogenerated currents are calculated at one arbitrary position within the i-layer since they are independent of position. For simplification, I use $x = 0$ for the calculation of the currents.

$$
\begin{aligned}
J_{\text{Dark}} =\ & J_{n_{\text{Dark}}}(x=0) + J_{p_{\text{Dark}}}(x=0) && \text{(3.15)} \\
=\ & q\mu_n F \left(C_{1_{Dark}} + C_{2_{Dark}} + Z_1 e^{-\frac{V_{bi}}{V_t}} \right) \\
& + qD_n \left(C_{1_{Dark}} \Lambda_1 + C_{2_{Dark}} \Lambda_2 + Z_1 \frac{V_{bi}}{WV_t} e^{-\frac{V_{bi}}{V_t}} \right) \\
& + q\mu_p F \left(C_{5_{Dark}} + C_{6_{Dark}} + Z_3 + Z_4 + Z_5 e^{-\frac{V_{bi}}{V_t}} \right) \\
& - qD_p \left(C_{6_{Dark}} \frac{\mu_p F}{D_p} + Z_3 \Lambda_1 + Z_4 \Lambda_2 + Z_5 \frac{V_{bi}}{WV_t} e^{-\frac{V_{bi}}{V_t}} \right), && \text{(3.16)}
\end{aligned}
$$

and

$$
\begin{aligned}
J_{\text{Photo}} =\ & J_{n_{\text{Photo}}}(x=0) + J_{p_{\text{Photo}}}(x=0) \\
=\ & q\mu_n F \left(C_{1_{\text{Photo}}} + C_{2_{\text{Photo}}} + Z_2 \right) \\
& + qD_n \left(C_{1_{\text{Photo}}} \Lambda_1 + C_{2_{\text{Photo}}} \Lambda_2 - Z_1 \alpha \right) \\
& + q\mu_p F \left(C_{5_{\text{Photo}}} + C_{6_{\text{Photo}}} + Z_3 + Z_4 + Z_6 \right) \\
& - qD_p \left(C_{5_{\text{Photo}}} \frac{\mu_p E}{D_p} + Z_3 \Lambda_1 + Z_4 \Lambda_2 - Z_6 \alpha \right).
\end{aligned}
$$

$$
\text{(3.17)}
$$

The coefficients $C_{i_{\text{Dark}}}$, $C_{i_{\text{Photo}}}$ ($i = 1, ..., 8$), Z_i ($i = 1, ..., 6$), and Λ_i ($i = 1, ..., 4$) are defined in appendix 5.1. The total current J_{tot} with incident light of several wavelengths λ_i is expressed as

$$J_{\text{tot}} = J_{\text{Dark}} + \sum_{\lambda_i=0}^{\lambda_i=\infty} J_{\text{Photo}}(\lambda_i). \tag{3.18}$$

Eq. (3.18) states that the total current density is the superposition of the dark current and the photocurrents generated by illumination with different wavelengths λ_i. Note that this superposition holds only if all current densities are calculated for the given voltage bias V.

3.1.2   Results of the analytical description

As a first test, I checked the results of my model against those of Taretto's model [67]. Fig. 3.4 compares the hole and electron concentrations $p(x)$ and $n(x)$ for two cases: $\mu_n\tau_n = \mu_p\tau_p$ (Taretto's model) and $\mu_n\tau_n \gg \mu_p\tau_p$ (my model). The assumption of equal values of mobilities and lifetimes of electrons and holes $\mu_n\tau_n = \mu_p\tau_p$ in Fig. 3.4a leads to the intersection of $p(x)$ and $n(x)$ exactly at the middle of the i-layer, i.e. $X_{c1} = X_{c2} = X_{c3} = W/2$ for different applied voltages. Since in a-Si:H-based films the last assumption is not fulfilled, I prefer to apply $\mu_n\tau_n \gg \mu_p\tau_p$. As a result, the position X_c within the i-layer where $p(x) = n(x)$ is not always at the middle of the i-layer but it is dependent on the applied voltage. The intersection $p(x) = n(x)$ moves from $X_{c1} = 3W/4$ at 0 V to $X_{c2} = 5W/8$ at 0.4 V and $X_{c3} = W/2$ at 0.8 V. Therefore, I introduce a term $\triangle_x$ which defines the difference between the actual intersection X_c of carriers and the middle of the i-layer as follows

$$\triangle_x = \left| 1 - \frac{X_c}{W/2} \right| \tag{3.19}$$

For quantifying the effect of the varying X_c, I first apply $X_c = X_s = W/2$, where W is the thickness of the i-layer, then calculate the carrier concentrations of electrons and holes, and again look for the position within the i-layer where both carrier concentrations are equal, e.g. X_c. After that, I solve the problem for $x = X_c$. The extended model presented in subsection 3.1.1 also accounts for the contribution of photons reflected at the back contact, according to Eq. (3.2), in the calculation of the current density $J(V)$. Fig. 3.6 shows the J/V-characteristics of an a-Si:H solar cell with different back side reflection coefficients R. The increase of the back side reflection enhances the probability of absorbing more photons, especially in the red region of the spectrum, and consequently the current density rises.
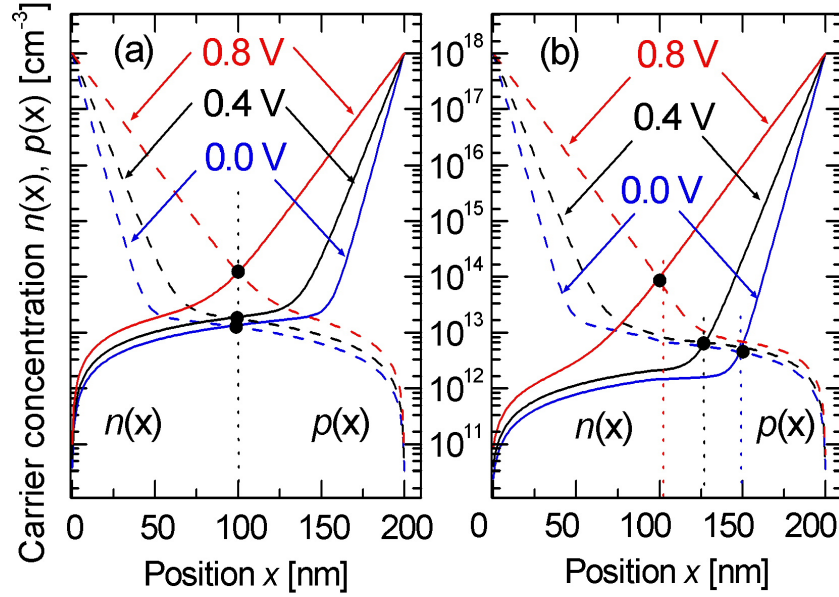
Fig. 3.4: Dependence of hole (dashed lines) and electron (solid lines) concentrations $p(x)$ and $n(x)$ as a function of the position within the i-layer and of the applied voltage (0.0 V, 0.4 V, 0.8 V). a) illustrates that the assumption of equal values of mobilities and lifetimes $\mu_n \tau_n = \mu_p \tau_p$ of electrons and holes (Taretto's model [67]) leads to the intersection of $p(x)$ and $n(x)$ exactly at the middle of the i-layer independent of the applied voltage, i.e. $X_c = W/2$. b) refers to the assumption (iii) and assumes $\mu_n \tau_n = 100\ \mu_p \tau_p$. The corresponding intersections of $p(x)$ and $n(x)$ within the i-layer at different applied voltages do not occur at a constant position, but are voltage-dependent.

3.1.3 Comparison to experiment

In order to test the validity of the extended analytical model presented in subsection 3.1.1, I deposit two a-Si:H solar cells at different deposition temperatures $T_{\rm dep}$ of the absorber layer using plasma enhanced chemical vapor deposition (PECVD) [9]. Subsequently, I measure the corresponding illuminated J/V-characteristics of these cells. The a-Si:H solar cells studied in this subsection are deposited on Asahi-U coated glass superstrates, and the light enters through the p-layer of the solar cell. The solar cells differ in the deposition temperature $T_{\rm dep}$ of the absorber layer in order to check the effect of the deposition temperature $T_{\rm dep}$ on the mobility-lifetime products $\mu_n \tau_n$ and $\mu_p \tau_p$ of electrons and holes . Fitting the measured J/V-
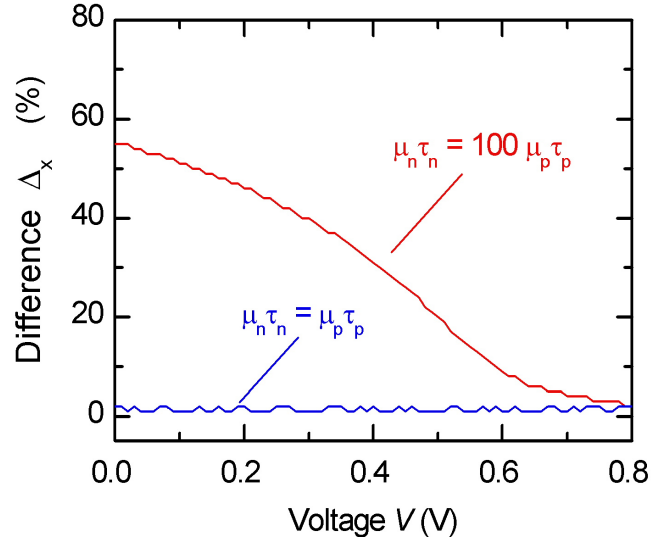
Fig. 3.5: The relative difference $\triangle_x$ between the intersection of the carriers within the i-layer X_c and its middle $W/2$ as a function the applied voltage. The assumption of non-equal values of the mobilities and the lifetimes of the carriers leads to divergence of X_c from $W/2$.

characteristics by the analytical model in subsection 3.1.1, results in different $\mu\tau$ products for different T_{dep}. Fig. 3.7 shows that the analytical model (solid lines) well reproduces the measured J/V-characteristics (symbols) of a-Si:H solar cells deposited at deposition temperatures (a) $T_{\text{dep}} = 135$ ºC and (b) $T_{\text{dep}} = 120$ ºC.

On the one hand, the deduced values $\mu_n\tau_n$ and $\mu_p\tau_p$ of electrons and holes for the abovementioned solar cells show an increase with the increase of the deposition temperature T_{dep} of the absorber layer of the solar cell. According to the analytical model, the electronic transport represented by the mobility-lifetime products of the charge carriers is enhanced with the increase of the deposition temperature T_{dep}. On the other hand, the model proves that to reproduce the J/V-characteristics, the values of the mobility-life time products $\mu_p\tau_p$ of holes have to be smaller than $\mu_n\tau_n$ of electrons.

The model in subsection 3.1.1 also describes the current density J of a-Si:H solar cells with the light entering either through the p-layer or through the n- layer. Fig. 3.8 shows that the generated current for the first case is higher than for the second case. This is due to i) Beer's absorption law, according to which most of the incident light is absorbed close to the front of the illuminated layer [7], and ii) the mobility-lifetime product $\mu_p\tau_p$ of holes in a-Si:H is lower than $\mu_n\tau_n$ for electrons. The best fit
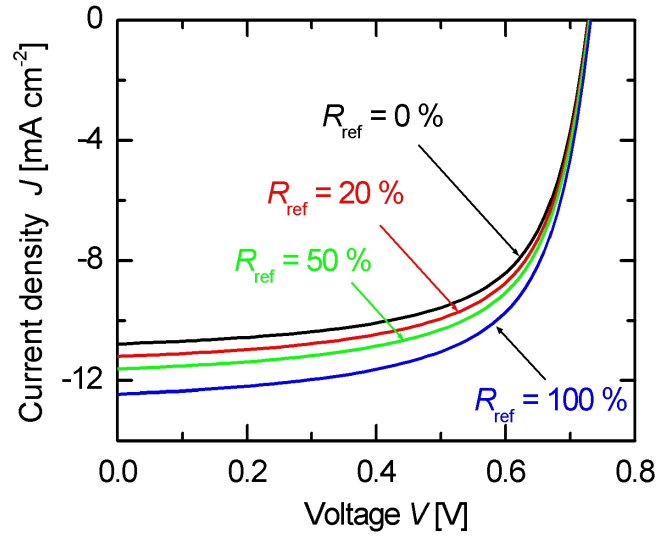
Fig. 3.6:   Current density/voltage (J/V) characteristics for different values of reflection R_{ref} at the back contact. The increase of the back reflection increases the probability of absorbing more photons, especially in the red region of the spectrum, resulting in a higher photogenerated current.

values of $\mu_n\tau_n$ and $\mu_p\tau_p$ that well reproduce the experimental J/V-characteristics are $\mu_n\tau_n = 6.2 \times 10^{-6}$ cm^2/V, and $\mu_p\tau_p = 6.6 \times 10^{-10}$ cm^2/V.

Fig. 3.9 demonstrates that the $\mu\tau$ products of both kinds of carriers are reasonably good fitting parameters. The graph is normalized to the error of the minimum deviation.
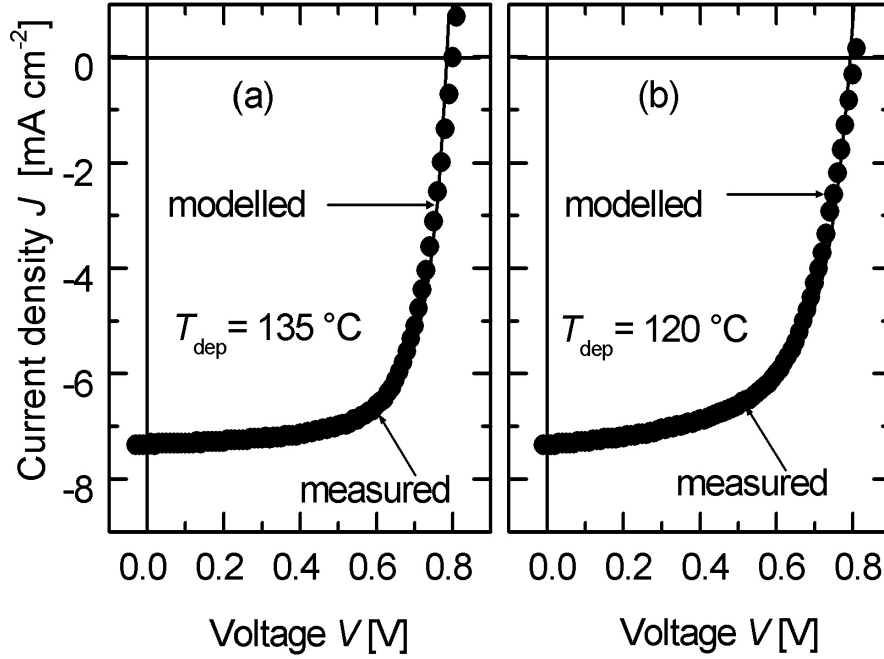
Fig. 3.7: Illuminated current density/voltage (J/V) characteristics of two *p-i-n* a-Si:H solar cells deposited at a) $T_{\text{dep}} = 135$ °C, and b) $T_{\text{dep}} = 120$ °C. The curves of J/V-characteristics (symbols) according to the handed model (solid lines) are modelled by the following parameters: a) $\mu_n\tau_n = 6.3 \times 10^{-5}$ cm^2/V, $\mu_p\tau_p = 2.2 \times 10^{-9}$ cm^2/V, $N_{\text{D}} = 0.45 \times 10^{13}$ cm^{-3}, $N_{\text{A}} = 1.2 \times 10^{15}$ cm^{-3}, $S_{\text{n}} = 0.51 \times 10^4$ cm/s, and $S_{\text{p}} = 1.8 \times 10^6$ cm/s. For b), $\mu_n\tau_n = 0.36 \times 10^{-8}$ cm^2/V, $\mu_p\tau_p = 0.53 \times 10^{-9}$ cm^2/V, $N_{\text{D}} = 0.29 \times 10^{13}$ cm^{-3}, $N_{\text{A}} = 2.4 \times 10^{15}$ cm^{-3}, $S_{\text{n}} = 0.24 \times 10^4$ cm/s, and $S_{\text{p}} = 1.3 \times 10^6$ cm/s.
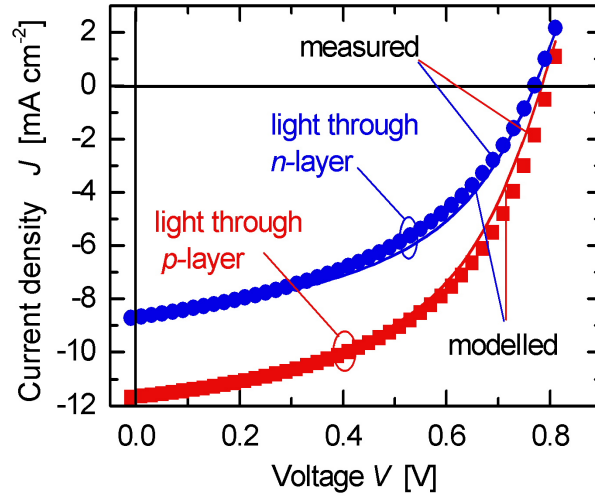
Fig. 3.8: Current density J of a bifacial a-Si:H solar cell where the light can enter through the p-layer or the n-layer. Due to the assumption of $\mu_n \tau_n \gg \mu_p \tau_p$, the generated current in the first case is higher than that of the second case. The analytical model (solid lines) agrees well with the measured data (symbols). The best fit parameters are: $\mu_n \tau_n = 6.2 \times 10^{-6}$ cm^2/V, $\mu_p \tau_p = 6.6 \times 10^{-10}$ cm^2/V.
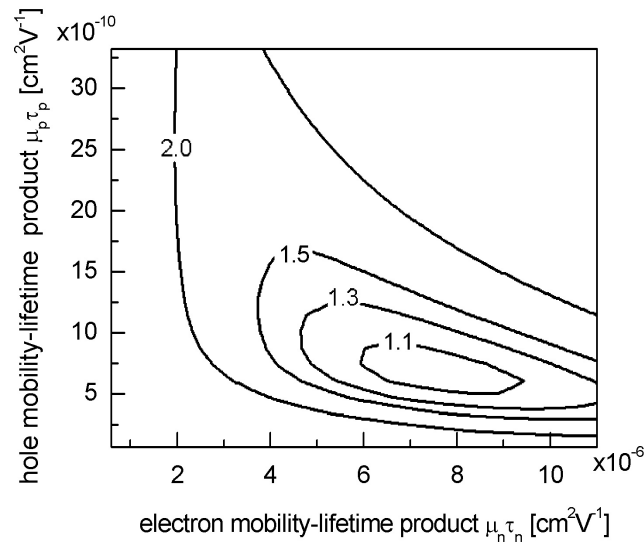
Fig. 3.9: Contour plot of the root mean square error between the measured and the modelled J/V-characteristics. The data are normalized to the optimum value for the data in Fig. 3.8.

3.2 Amorphous silicon at low deposition temperatures

To optimize flexible, unbreakable, and light-weight a-Si:H-based devices on the available plastic films, the deposition temperature should be reduced below 150 ºC to not exceed the glass transition temperature of the substrate foils [83]. However, the decrease of the deposition temperature T_{dep} (substrate temperature) strongly affects the quality of a-Si:H-based materials.

This section investigates the effect of the deposition temperature 80 ºC $< T_{\mathrm{dep}} <$ 180 ºC on the deposited a-Si:H films for approximately 60 minute deposition times. The silane flow rate [SiH$_4$] was set at 10 sccm without any hydrogen dilution, the total pressure P_{r} in the chamber at 400 mTorr, the plasma power density P_{in} at 8.9 mW/cm^2, and the plasma frequency f at 13.56 MHz.

3.2.1 Properties of amorphous silicon at low temperatures

It is well established that the deposition temperature T_{dep} affects the electronic properties of a-Si:H-based materials [84, 85]. Fig. 3.10 shows the dark conductivity σ_{dark} and the activation energy E_{act} measured at room temperature (T = 300 K) of intrinsic a-Si:H films as a function of the deposition temperature T_{dep}. It shows that the dark conductivity σ_{dark} decreases by two orders of magnitude while the activation energy E_{act} increased from 720 meV to 873 meV as the deposition temperature decreases from $T_{\mathrm{dep}} = 180$ ºC to 80 ºC.

The increase of the deposition temperature increases the diffusion of the deposited atoms of the a-Si:H-based materials and therefore the resulting film is homogenous and dense as shown in Fig. 3.11a. On the contrast, the decrease of the deposition temperature increases the probability that the deposited atoms be adsorbed on the surface of the substrate before they diffuse, resulting in thicker films of lower structural and electronic quality as shown in Fig. 3.11b. Fig. 3.12 shows that the decrease of the deposition temperature T_{dep} increases the a-Si:H deposition rate $r = d_{\mathrm{film}}/t_{\mathrm{dep}}$ where d_{film} is the film thickness and t_{dep} is the deposition time.

Veen and Schropp [86] showed that the decrease of the deposition temperature increases the hydrogen concentration in the a-Si:H films. Smets [87] observed that the surface hydride configuration depends on the surface temperature, i.e. the transition from dominant $\equiv$SiH at high deposition temperature to dominant $-$SiH$_3$ at low deposition temperature. Therefore, the decrease of the deposition temperature
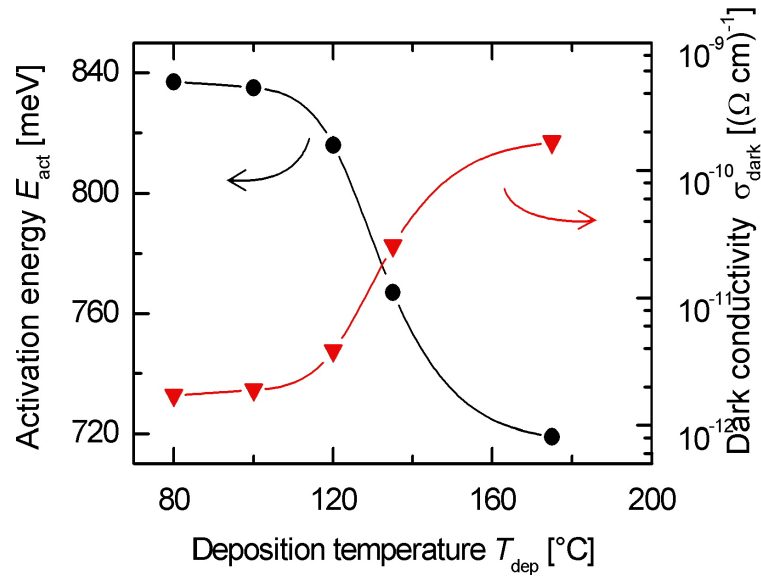
Fig. 3.10: Dark conductivity σ_{dark} (triangles) and activation energy E_{act} (circles) at room temperature (T=300 K) of intrinsic a-Si:H films as a function of the deposition temperature T_{dep}. The dark conductivity σ_{dark} decreases by two orders of magnitude while the activation energy E_{act} increases from 720 meV to 873 meV as the deposition temperature decreases from $T_{\text{dep}} = 180$ ºC to 80 ºC.
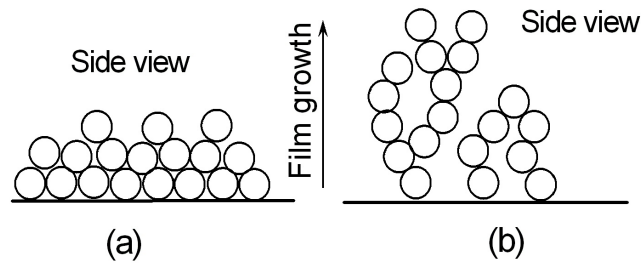
Fig. 3.11: Illustration of the growth morphology of a-Si:H films where the deposition temperature T_{dep} in a) is higher than in b). At low deposition temperature T_{dep} the surface mobility of the deposited atoms is low, resulting in a columnar growth and therefore the deposition rate r is high. On the other hand, increasing the deposition temperature T_{dep} increases the surface mobility of the deposited atoms and therefore the deposition rate r drops.

T_{dep} favors hydrogen incorporation and formation of micro voids due to the presence of SiH_2 and SiH_3 units incorporated into the bulk of the a-Si:H films. At low de-
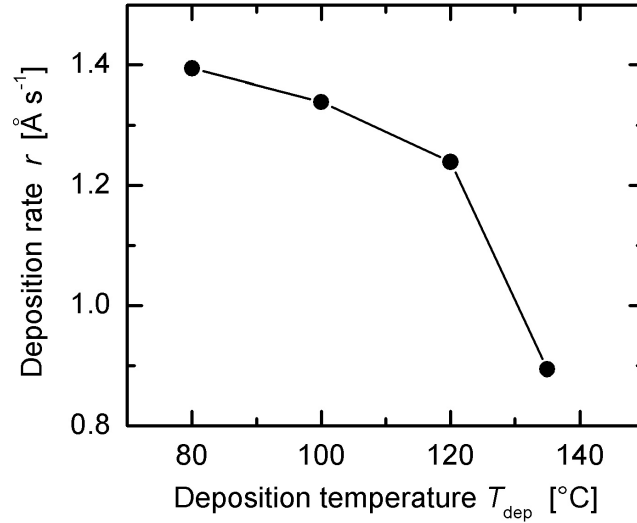
Fig. 3.12: Deposition rate r of intrinsic a-Si:H films as a function of deposition temperatures T_{dep}. The line is to help the eye. The decrease of the deposition temperature T_{dep} increases the probability that the deposited atoms be adsorbed on the surface of the substrate before they diffused resulting in high deposition rates. The deposition rate r is defined as the ratio between the film thickness and the deposition time.

position temperatures, it is therefore mandatory to apply a high hydrogen dilution of the process gases and very high frequency (VHF) excitation of the deposition plasma, in order to control the increasing of SiH_2 and SiH_3 units [88]. The Tauc gap E_g increases due the decrease of the deposition temperature T_{dep}. Fig. 3.13 shows the increase of $E_g \approx 1.74$ eV at $T_{dep} = 180$ ºC to $E_g = 1.84$ eV at $T_{dep} = 80$ ºC.

The Urbach energy E_U reflects the disorder broadening of the bands which give rise to states in the gap. Therefore, the low quality a-Si:H-based materials have high values of the Urbach energy E_U [89]. Fig. 3.14 shows that the Urbach energy E_U increases from ≈ 50 meV at $T_{dep} = 180$ °C to $E_g = 85$ meV at $T_{dep} = 80$ °C.

The defect density N_s is calculated from the integration of the absorption coefficient α_{CPM} determined by the CPM measurement. The decrease of the deposition temperature T_{dep} gives rise to the formation of the defect density N_s although the decrease of T_{dep} increases the hydrogen content since the quality of the a-Si:H-based materials strongly depends on the way of incorporating the hydrogen rather than the hydrogen content itself [90].
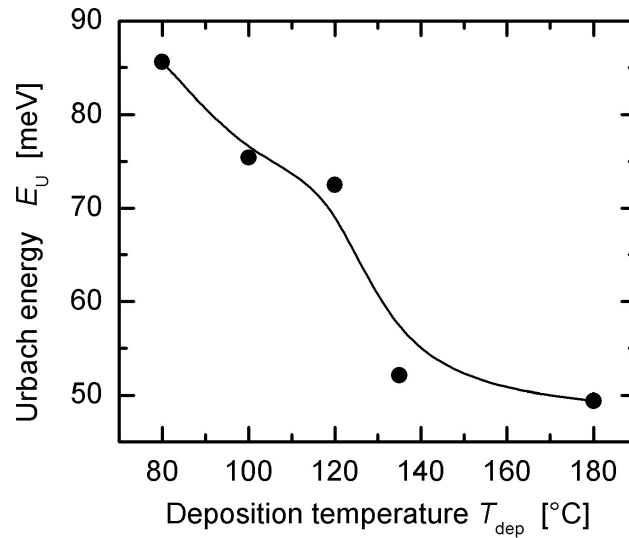
Fig. 3.15 shows that the defect density N_s calculated from CPM increases from
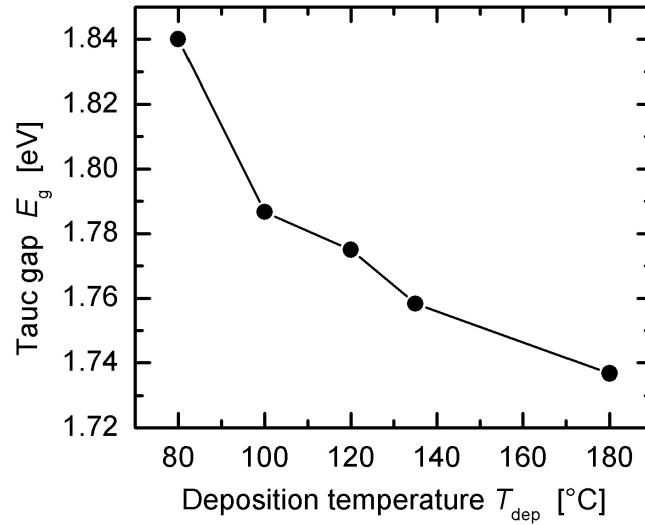
Fig. 3.13: Tauc gap E_g of intrinsic a-Si:H films as a function of the deposition temperature T_{dep}. The Tauc gap E_g increases from approximately 1.74 eV at T_{dep} = 180 °C to E_g = 1.84 eV at T_{dep} = 80 °C.

2.0 × 10^{15} cm^{-3} at T_{dep} = 135 °C to 6.0 × 10^{16} cm^{-3} at T_{dep} = 120 °C.

Fig. 3.14: Urbach energy E_U of intrinsic a-Si:H films as a function of the deposition temperature T_{dep}. The Urbach energy E_U increases from ≈ 50 meV at T_{dep} = 180 °C to E_g = 85 meV at T_{dep} = 80 °C.
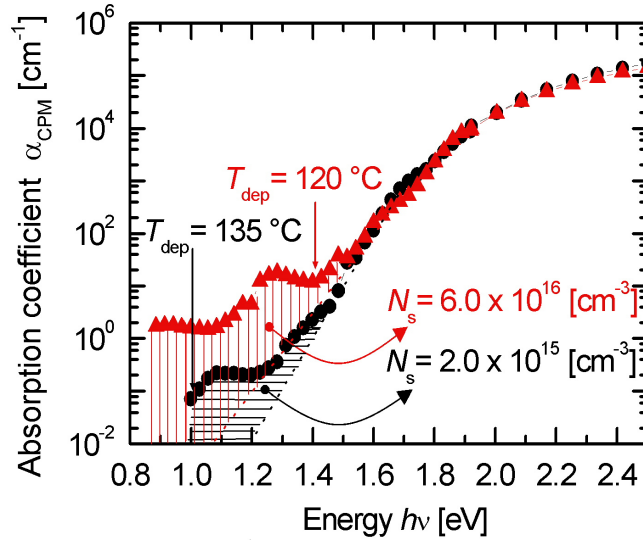
Fig. 3.15: Absorption coefficient α_{CPM} determined by the CPM measurement versus photon energy $h\nu$. The defect density N_{s}, integrated from α_{CPM} below the Urbach edge, of intrinsic a-Si:H films increases from 2.0×10^{15} cm^{-3} at $T_{\mathrm{dep}} = 135$ °C (horizontal black lines) to 6.0×10^{16} cm^{-3} at $T_{\mathrm{dep}} = 120$ °C (vertical red lines).

## 3.2.2 Optimization of amorphous silicon at low temperatures

Deposition pressure

In this subsection, I characterize and optimize amorphous silicon based films deposited at a deposition temperature $T_{\mathrm{dep}} = 120$ °C as a function of the deposition pressure P_{r}. The silane SiH$_4$ flow rate was kept constant at 10 sccm without any hydrogen dilution. The plasma frequency f and the plasma power P_{in} were also kept constant at 13.56 MHz and 2 W, respectively. For this purpose, I deposited four a-Si:H layers using the abovementioned deposition parameters while the deposition pressure P_{r} was only changed from 200 mTorr to 600 mTorr.

Since the material quality of a-Si:H layers depends on the deposition pressure P_{r} [86] by affecting the mean free path length of the dissociated silane SiH$_4$ atoms, I measured their temperature-dependent dark conductivity $\sigma(T)$ and calculated the dark conductivity σ_{dark} at room temperature and the activation energy E_{act} as a function of the deposition pressure P_{r} as shown in Fig. 3.16. The optimum values of the dark conductivity σ_{dark} (minimum) and the activation energy E_{act} (maximum)
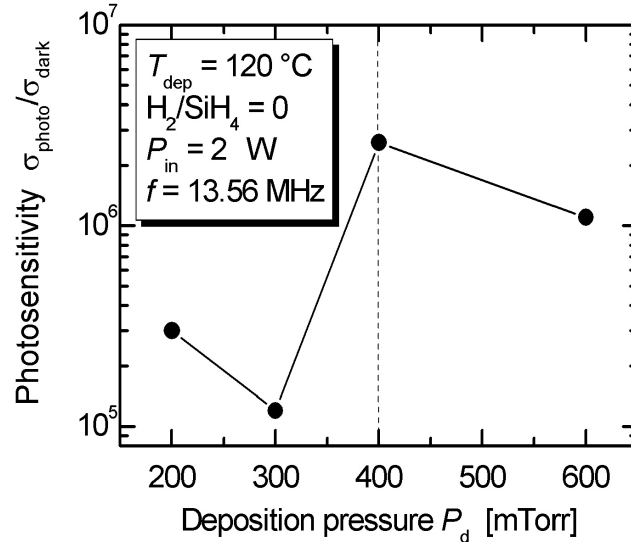
occur at deposition pressure $P_r = 400$ mTorr.
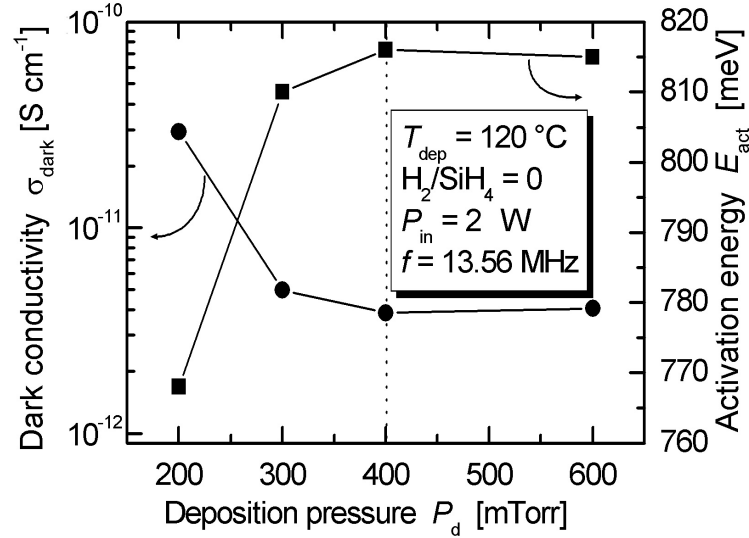
Fig. 3.16: Deposition pressure P_r dependence of the dark conductivity σ_{dark} (circles) and the activation energy E_{act} (squares). The best performance of a-Si:H films that has maximum value of E_{act} or minimum value of σ_{dark} in this series occurs at deposition pressure $P_r = 400$ mTorr.

I also measured the photosensitivity $\sigma_{photo}/\sigma_{dark}$ (ratio of the photoconductivity to dark conductivity) at room temperature of the abovementioned samples and I found that the same sample which showed the best performance at a deposition pressure $P_r = 400$ mTorr with respect to activation energy E_{act} also exhibits the highest photosensitivity at the same value of the deposition pressure $P_r = 400$ mTorr as shown in Fig. 3.17.

The deposition pressure P_r also affects the deposition rate r of the a-Si:H films. At very low pressure regime (≤ 37.5 mTorr) [86], the rate of silane dissociation increases as the deposition pressure P_r increases resulting in an increase of the deposition rate r of the a-Si:H films, while at higher values of deposition pressure P_r, the silane supply becomes limited leading to a decrease in the deposition rate r of the a-Si:H films [91]. Fig. 3.18 shows that the deposition rate r of a-Si:H films decreases from ~ 1.2 Å/s at a deposition pressure P_r of 200 mTorr to ~ 0.75 Å/s at a deposition pressure P_r of 600 mTorr.

I applied the optimized i-layer from Fig. 3.17 ($P_r = 400$ mTorr) in an n-i-p ordered a-Si:H solar cell where the substrate is Asahi-U coated glass. The resulting a-Si:H cell had an efficiency $\eta = 5.9$ %. Fig. 3.19 shows the J/V-characteristics of this

Fig. 3.17: Dependence of photosensitivity $\sigma_{\mathrm{photo}}/\sigma_{\mathrm{dark}}$ (ratio of the photoconductivity to dark conductivity) at room temperature on the deposition pressure P_{r}. The highest value of the photosensitivity occur at deposition pressure $P_{\mathrm{r}} = 400$ mTorr.
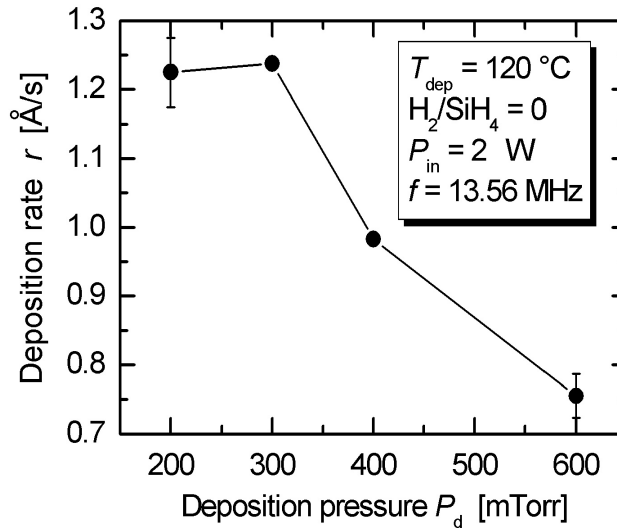
Fig. 3.18: Dependence of the deposition rate r of the a-Si:H films on the deposition pressure P_{r}. The deposition rate r decreases from ~ 1.2 Å/s at $P_{\mathrm{r}} = 200$ mTorr to ~ 0.75 Å/s at $P_{\mathrm{r}} = 600$ mTorr due to the limitation of the silane supply at higher deposition pressures P_{r}.

optimized a-Si:H solar cell and it shows also that the analytical model of subsection

3.1.1 (solid line) of the J/V characteristics very well fits the experimental data (symbols) by assuming $\mu_n\tau_n = 3.5 \times 10^{-5}$ cm^2/V and $\mu_p\tau_p = 1 \times 10^{-7}$ cm^2/V as modelling parameters.
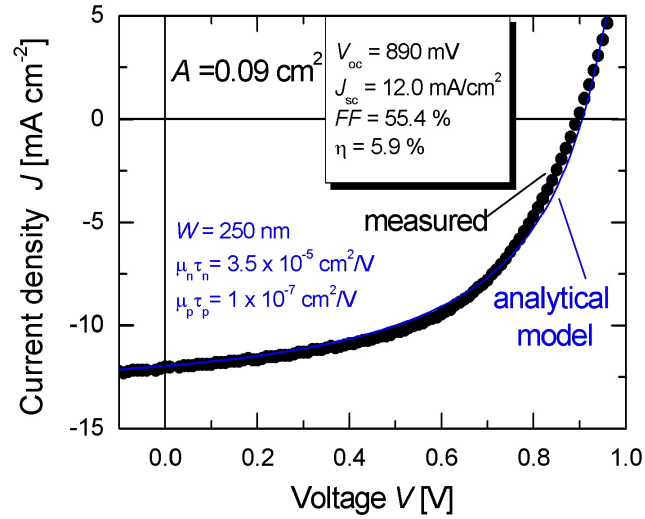
Fig. 3.19: Plot of illuminated current density/voltage (J/V) characteristics of *n-i-p* a-Si:H solar cell. The experimental data of the J/V-characteristics (symbols) are explained by the analytical model, discussed in subsection 3.1.1, (solid line) by applying the following parameters: $\mu_n\tau_n = 3.5 \times 10^{-5}$ cm^2/V, $\mu_p\tau_p = 1 \times 10^{-7}$ cm^2/V.
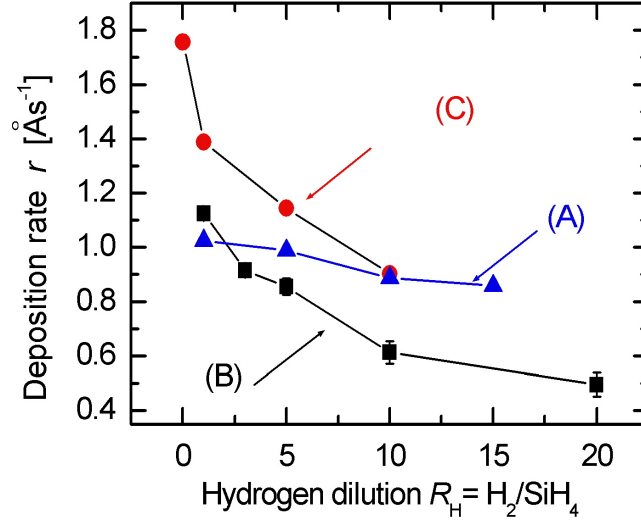
Hydrogen dilution

In this subsection, I investigate the influence of the hydrogen dilution R_H, defined by the ratio between the hydrogen H_2 flow rate and the silane SiH_4 flow rate, on the optical and electronic properties of a-Si:H-based films. The insertion of hydrogen during the deposition of a-Si:H at low temperature deposition T_{dep} is important due to the deterioration of the electronic properties of a-Si:H films at low temperature deposition T_{dep} [92–94] by increasing the defect density. Fig. 3.20 shows that the increase of the hydrogen dilution R_H reduces the absorption coefficient α at low energies, i.e. the contribution of the defects in the absorption decreases with the increase of the hydrogen dilution.
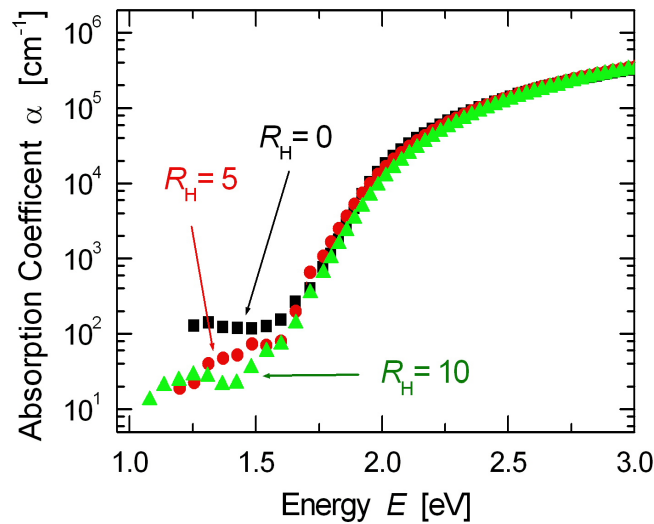
Fig. 3.20: Absorption coefficient α of i-layer a-Si:H for different values of hydrogen dilutions R_H. The increase of R_H reduces the defect density within the band gap of the film leading to the enhancement of the film quality.

The insertion of hydrogen H_2 as an excess gas during the deposition of a-Si:H based films increases the etch rate of the growing surface and helps to find energetically more favorable sites [95] leading to a more ordered structure. Therefore, one expects that the increase in hydrogen dilution R_H decreases the deposition rate r of the a-Si:H-based films as shown in Fig. 3.21. The samples (B) in Fig. 3.21 are deposited at deposition temperature T_{dep} of 120 °C while the samples (C) are deposited at deposition temperature T_{dep} of 135 °C , therefore, one expects the deposition rate r to be higher for samples (B) than for samples (C), which is, however,

not the case in Fig. 3.21. The explanation for this is the that distance between the electrode and the substrate of the deposition chamber of the *i*-layer was reduced from 18 mm to 13 mm in the period between the depositions of the samples (B) and (C), leading to higher power density for the deposition of samples (C).

Fig. 3.21: Dependence of the deposition rate r on the hydrogen dilution R_H, which is defined as the ratio between the H_2 and SiH_4 flow rates. The deposition parameters of (A) are: deposition temperature $T_{dep} = 135$ °C, deposition pressure $P_r = 400$ mTorr, plasma power $P_{in} = 5$ W, and plasma frequency $f = 80$ MHz and the deposition parameters of (B) are: deposition temperature $T_{dep} = 120$ °C, deposition pressure $P_r = 600$ mTorr, plasma power $P_{in} = 2$ W, and plasma frequency $f = 13.56$ MHz while the deposition parameters of (C) are: deposition temperature $T_{dep} = 135$ °C, deposition pressure $P_r = 600$ mTorr, plasma power $P_{in} = 2$ W, and plasma frequency $f = 13.56$ MHz.

The insertion of hydrogen during the deposition of a-S:H strengthens the bonds between the atoms of the a-Si:H structure due to the incorporation of the hydrogen atoms resulting in the increase of the Si-H bonds that have energies higher than Si-Si bonds [96]. Therefore, the Tauc gap E_g increases due the increase of the hydrogen dilution R_H as shown in Fig. 3.22 where one also notices the increase of Tauc gap E_g for different deposition conditions.

An optimum *i*-layer should have the best electronic properties, indicated by a high photosensitivity (measured from the dark- and photoconductivity) and a large ambipolar diffusion length L_{amb} (calculated from the SSPG method). Fig. 3.23
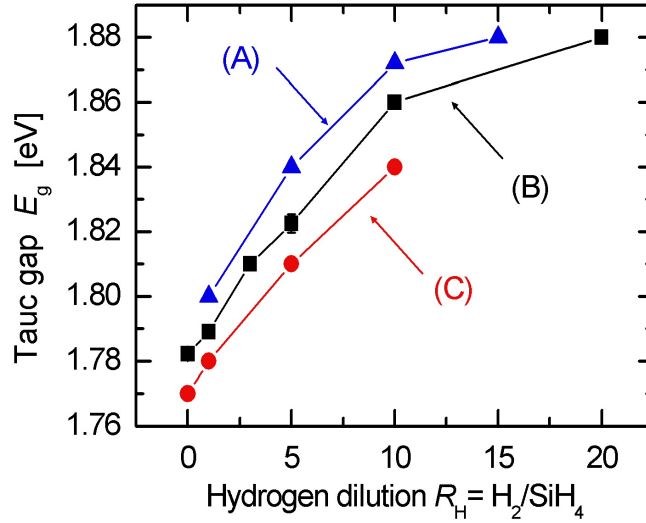
Fig. 3.22: Dependence of the Tauc gap E_g on the hydrogen dilution R_H, which is defined as the ratio between the H_2 and SiH_4 flow rates. The set of deposition parameters (A), (B), and (C) is the same as in Fig. 3.21.
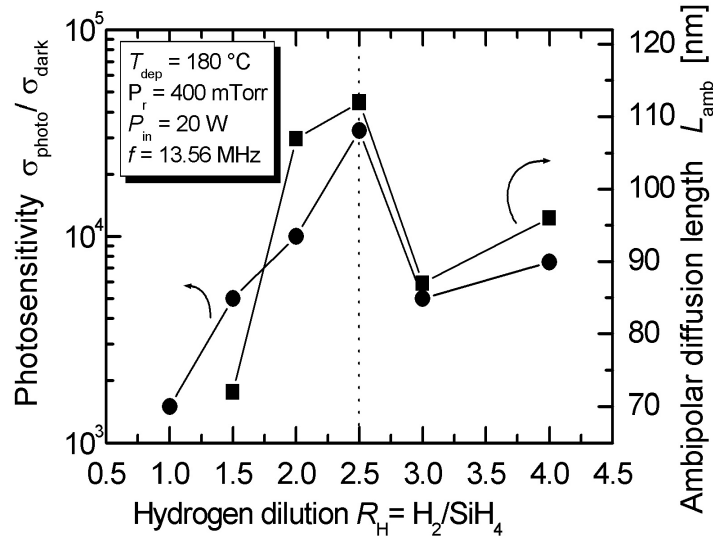
shows the dependency of the photosensitivity (circles) and the ambipolar diffusion length L_{amb} (squares) on the hydrogen dilution rate R_H, and it shows that the best *i*-layer needs a hydrogen dilution $R_H = 2.5$.

I apply the optimum *i*-layer in a *p-i-n* a-Si:H solar cell and the resulting efficiency η is 6.8 %. Fig. 3.24 shows the experimental (symbols) and the analytical model (curve) of the *J/V*-characteristic of the *p-i-n* a-Si:H solar cell with an *i*-layer of $R_H = 2.5$. The modelling parameters are $\mu_n\tau_n = 4 \times 10^{-4}$ cm^2/V for electrons and $\mu_p\tau_p = 1.5 \times 10^{-6}$ cm^2/V for holes.

The optimum *i*-layer is deposited by radio frequency (RF) $f = 13.56$ MHz, and by this frequency it is difficult to achieve homogeneous deposition especially at higher hydrogen dilution R_H. Therefore, I investigate very high frequency (VHF) excitation at $f = 80$ MHz of the plasma deposition. Fig. 3.25 shows the hydrogen dilution R_H dependence of both photosensitivity (circles) and the conductivity σ (triangles). The maximum photosensitivity occurs at $R_H = 10$. The abrupt decrease of the photosensitivity above $R_H = 10$ indicates that the material starts to change its structure from the amorphous into microcrystalline.

When changing the deposition pressure P_r from 400 mTorr to 200 mTorr the maximum of the photosensitivity still occurs at hydrogen dilution $R_H = 10$, as shown in Fig. 3.26.
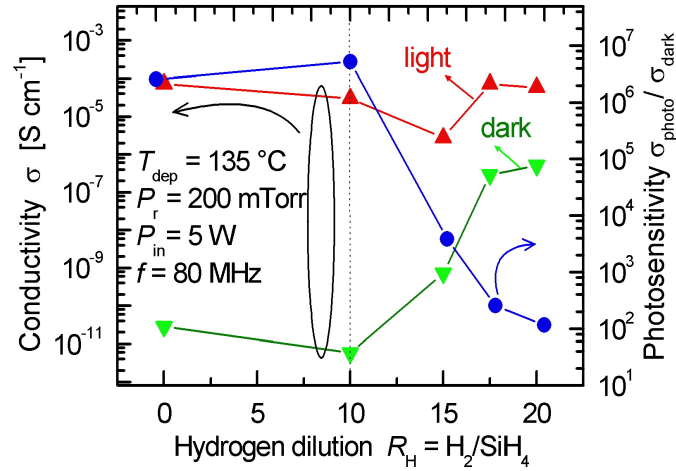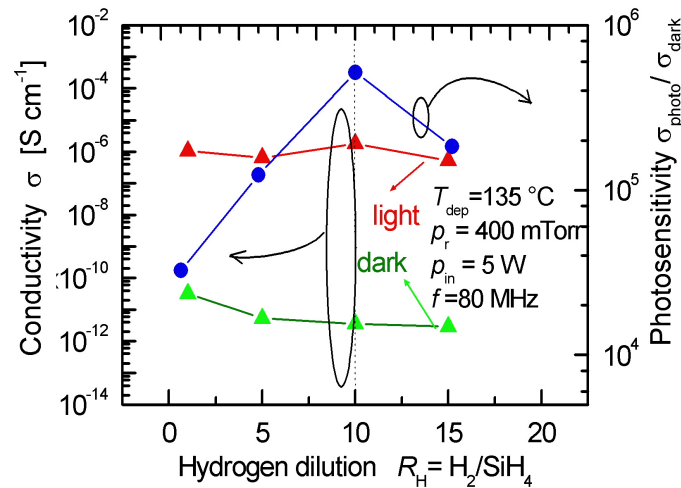
Fig. 3.23: Dependence of the photosensitivity (circles) and the ambipolar diffusion length L_{amb} (squares) on the hydrogen dilution R_{H}. The optimized i-layer shows a diffusion length L_{amb} of 112 nm and a photosensitivity of 3×10^4.
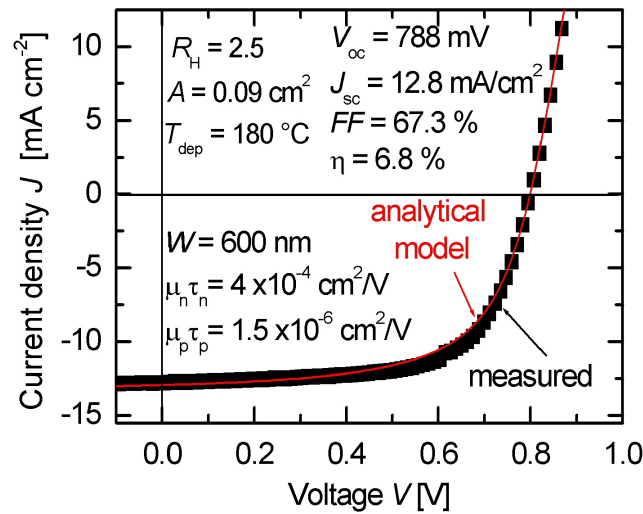
Fig. 3.24: Current density/voltage (J/V) characteristics of p-i-n a-Si:H solar cell that has an hydrogen dilution R_{H} of the i-layer, where $R_{\mathrm{H}} = 2.5$. The analytical model (curve) of the J/V-characteristics of a-Si:H solar cells produces the experimental data (symbols) by applying the mobility-life times $\mu_{\mathrm{n}}\tau_{\mathrm{n}} = 4 \times 10^{-4}$ cm^2/V for electrons and $\mu_{\mathrm{p}}\tau_{\mathrm{p}} = 1.5 \times 10^{-6}$ cm^2/V for holes as modelling parameters.

Fig. 3.25: Dependence of the photosensitivity (circles) and of the dark- and light-conductivity σ (triangles) on the hydrogen dilution R_H. The optimized i-layer at a deposition pressure of 200 mTorr shows a photosensitivity of 5.2×10^6 at R_H = 10. The abrupt increase of the dark conductivity σ (downward triangles) represent the change in the structure of the i-layer from the amorphous phase to the microcrystalline phase.

Fig. 3.26: Dependence of the photosensitivity (circles) and of the dark- and light-conductivity σ (triangles) on the hydrogen dilution R_H. The optimized i-layer at a deposition pressure of 400 mTorr shows a photosensitivity of 5.17×10^5 at $R_H = 10$ which is the same optimum hydrogen dilution as in Fig. 3.25.

3.3 Amorphous silicon solar cells with *p-i-n* and *n-i-p* structures

## 3.3.1 Improvement of *p-i-n* a-Si:H solar cells

This subsection presents the beneficial effect of incorporating a very thin microcrystalline *p*-layer on the performance of a-Si:H solar cells deposited on TCO-coated glass. The TCO/*p*-layer interface in a-Si:H solar cells is a very sensitive region [97], and therefore needs to be well optimized. Two different TCOs are used here as front contacts: ZnO:Al which is deposited in the sputtering chamber of a cluster tool at *ipe* and SnO_2:F (called Asahi-U) is obtained from Asahi company.

**Choice of the transparent front contact**

This subsection compares a-Si:H solar cells deposited on ZnO:Al contact from one side, and on Asahi-U contact from the other side as shown in Fig. 3.27a.

To study the effect of the TCO type, I deposit two very similar a-Si:H solar cells in the same deposition run, but on different TCOs. Both cells have the same window *p*-type layer, which is alloyed with CH_4 in order to widen the band gap and to better exploit the blue part of the solar spectrum [98].

Fig. 3.28 shows that the output characteristics of both solar cells is not the same. The current density/voltage (J/V) characteristics of a-Si:H solar cells deposited on ZnO:Al-coated glass show an S-shape (bending), due to the rectifying behavior between the *p*-a-SiC:H layer and the ZnO:Al contact, while the cell on Asahi-U exhibit a much better solar cell characteristics. The values of the short-circuit current J_{sc} and the open-circuit voltage V_{oc} are approximately the same in both cases but the additional barrier on ZnO:Al deteriorates the fill factor FF.
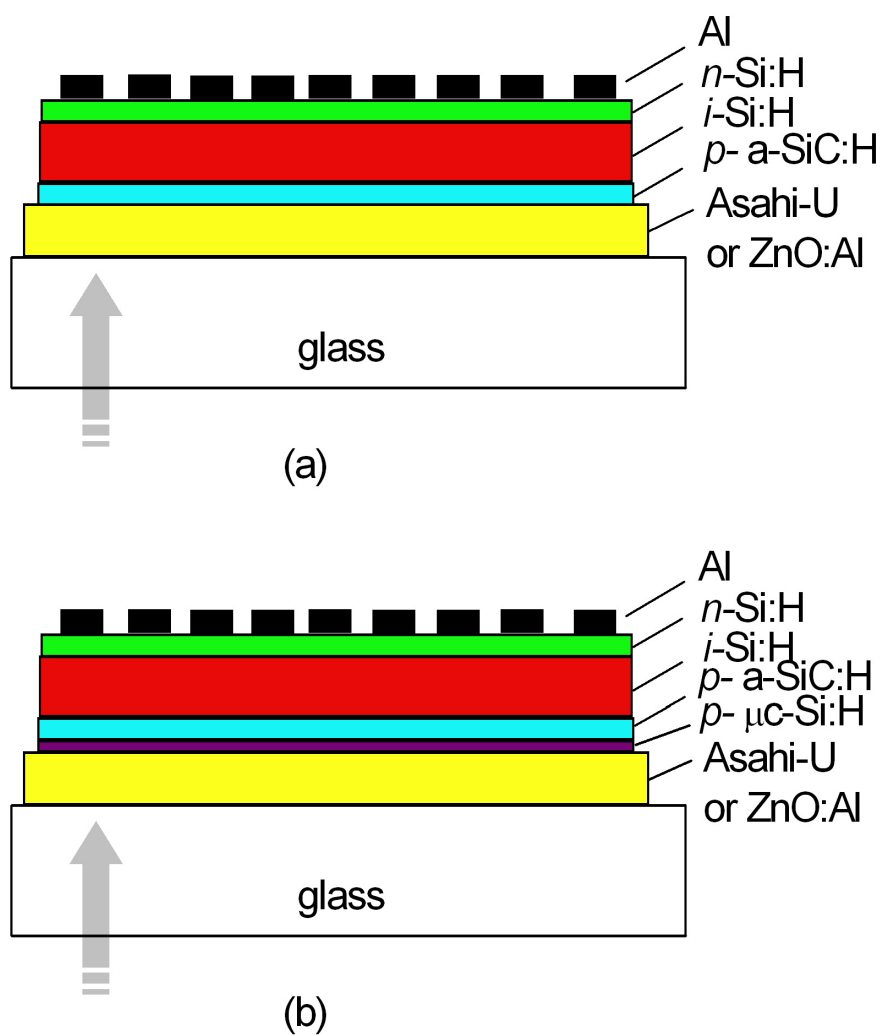
Fig. 3.27: Two a-Si:H solar cell structures deposited on two different types of front contacts: ZnO:Al and Asahi-U. In a), the *p*-type a-SiC:H layer is deposited directly on top of the TCO contact, while in b), a very thin microcrystalline *p*-type μc-Si:H layer is inserted between the *p*-type a-SiC:H layer and the TCO contact.
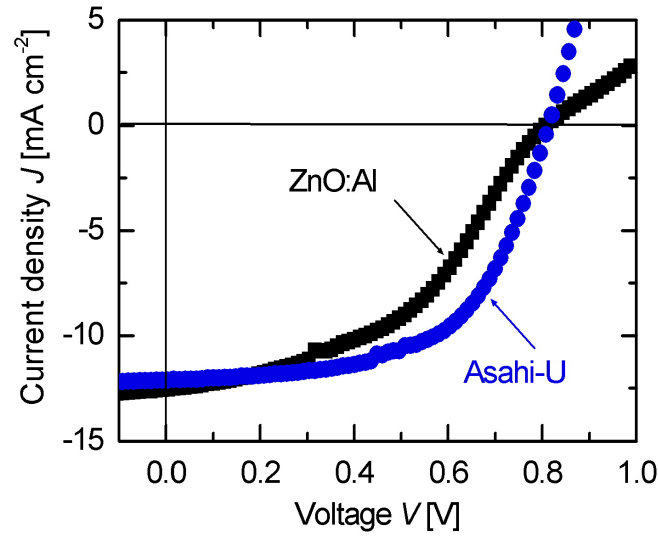
Fig. 3.28: Current density/voltage (J/V) characteristics of a-Si:H cells deposited on ZnO:Al-coated glass (black rectangles) and on an Asahi-U front contact (blue circles) at $T_{dep} = 176$ °C. The S-shape of the J/V-characteristics occurs when applying p-type a-SiC:H layer directly on top of the ZnO:Al contact.

Incorporation of a p-type μc-Si:H layer

The window layer in a-Si:H solar cells has to be a wide band gap layer in order to enhance the photogenerated current in the absorber layer. One of the significant improvements to the p-i-n solar cell structure was the use of p-type hydrogenated amorphous silicon carbide a-SiC:H films [99, 100] which decrease the absorption of the solar spectrum within the window layer by increasing the Tauc gap E_g. Fig. 3.29 shows the methane ratio R_M dependency of the Tauc gap E_g of p-type a-SiC:H layers deposited at different deposition temperatures T_{dep}. The Tauc gap E_g decreases at higher deposition temperatures due to the decrease of the hydrogen content in the deposited films. However, the problem of barrier formation between the p-layer and the ZnO:Al, due to the interaction of hydrogen with the ZnO:Al surface leading to a thicker depletion zone in the p-layer [101], is solved by the insertion of highly doped layer between the p-layer and the ZnO:Al front contact, in my work it is microcrystalline p-type μc-Si:H. Arch [102] as well as Dasgupta et.al. [103] reported on the importance of the p-layer/front contact on the performance of a-Si:H solar cells.
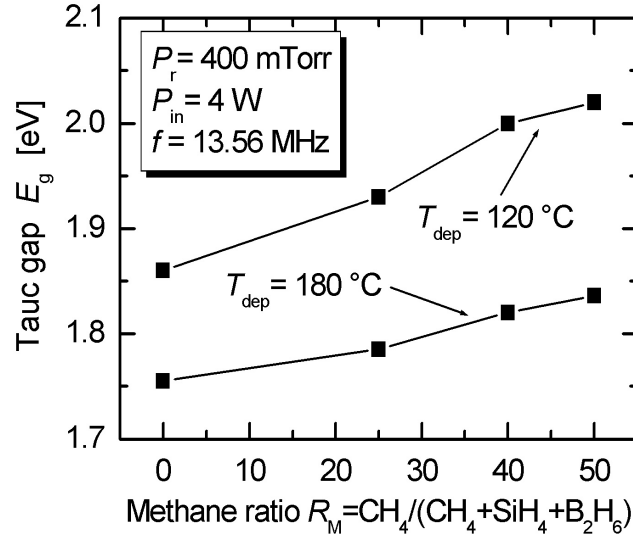
Fig. 3.29: Tauc gap E_g of as a function of methane ratio R_M of a-SiC:H p-layer. The increase of the methane ratio increases the percentage of carbon inside the film and therefore increases the Tauc gap E_g of the film. The Tauc gap E_g at deposition temperature $T_{dep} = 180$ °C is lower than at deposition temperature $T_{dep} = 120$ °C due to the decrease of the hydrogen content at higher deposition temperatures.

The p-type microcrystalline buffer layer used in this work, with a hydrogen-to-silane $R_H \approx 80$, shows a band gap of 2.0 eV and an activation energy of 30 meV. Ferreira et.al. [104] showed that this layer has to have a high hydrogen-to-silane flow ratio (typically 50-200). I insert this μc-Si:H p-layer (~ 5 nm) between the amorphous p-type a-SiC:H layer and the ZnO:Al contact in p-i-n-based a-Si:H solar cells to improve the contact between the front contact and the a-Si:H solar cell. Fig. 3.30 compares the open-circuit voltage V_{oc}, the short-circuit current density J_{sc}, the fill factor FF, and the conversion efficiency η with (open symbols), and without (closed symbols) insertion of p-type μc-Si:H layer for solar cells of different areas. Fig. 3.30 shows that the incorporation of a p-type μc-Si:H layer mainly enhances both the fill factor FF and the open-circuit voltage V_{oc} [105] due to the reduction of the large potential drop at the p/i interface [106]. The short-circuit current density J_{sc} decreases due to the absorption within this layer. The resulting efficiency η is clearly improved.
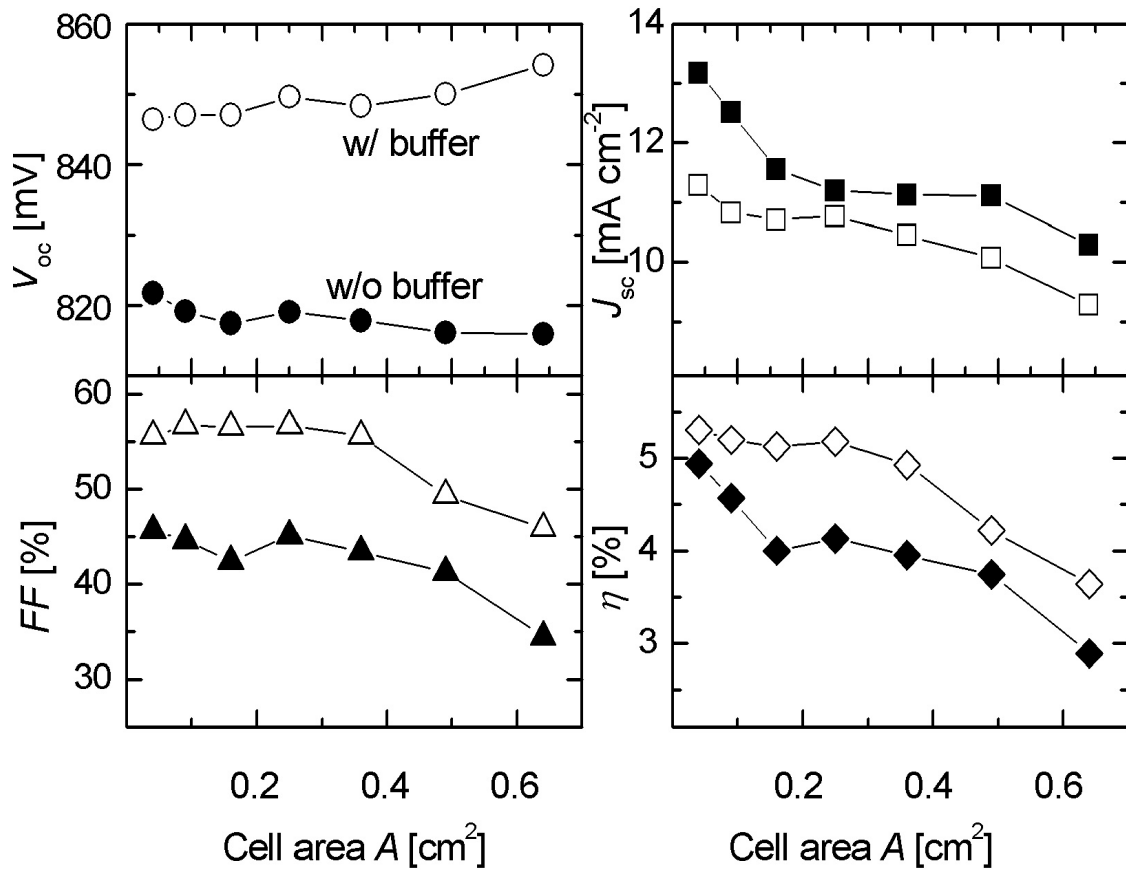
Fig. 3.30: Effect of the insertion of *p*-type μc-Si:H layer (open symbols) between the a-SiC:H *p*-type layer and the ZnO:Al front contact on the open-circuit voltage V_{oc}, the short-circuit current density J_{sc}, the fill factor FF, and the efficiency η for solar cells of different area. The incorporation of *p*-type μc-Si:H buffer layer enhances the efficiency η by improving both the fill factor FF and the open-circuit voltage V_{oc}, although the short-circuit current density J_{sc} decreases due to a small parasitic absorption of this buffer layer.

The incorporation of the *p*-type μc-Si:H bufferlayer improves the performance of the *p-i-n* solar cells as clearly evident from Fig. 3.28. The enhancement of the J/V-characteristics with ZnO:Al as front contact in Fig. 3.31b, is more pronounced than for the Asahi-U being used as a front contact in Fig. 3.31a.
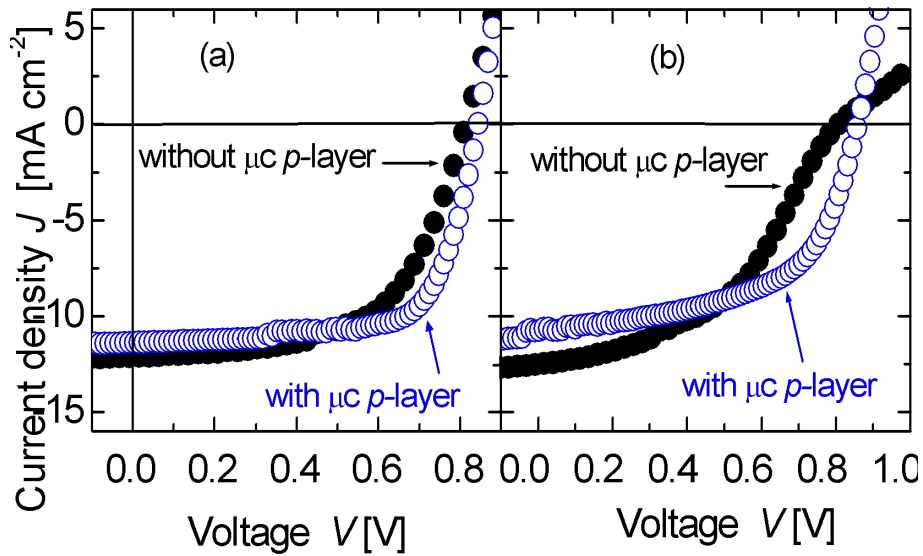
Fig. 3.31: Current density/voltage (J/V) characteristics of a-Si:H cells deposited on a) Asahi-U coated glass, and b) on ZnO:Al-coated glass. The enhancement of the J/V-characteristics where the front contact is ZnO:Al by the incorporation of a p-type μc-Si:H layer (closed symbols) is more pronounced than for Asahi-U as a front contact.

Insertion of an amorphous buffer between p^+- and i-layer

This subsection presents the effect of inserting an amorphous p-layer as a buffer layer in the p^+-i-n a-Si:H solar cells between the p^+-layer and the i-layer. I analyze two a-Si:H solar cells, one without a buffer layer and the other with a buffer layer, for different cell areas. The performance of p^+-i-n a-Si:H solar cells is drastically increased by inserting a very thin p-type buffer layer due the enhancement of the contact between the p^+-layer and the i-layer. Fig. 3.32 shows a comparison between p^+-i-n (closed symbols) and p^+p-i-n (open symbols) a-Si:H solar cells where the insertion of the buffer layer mainly enhances the fill factor FF and therefore the efficiency η.

Moreover, the insertion of the buffer layer enhances the spectral response of a-Si:H solar cells and reduces the degradation of the a-Si:H solar cell. Fig. 3.33 shows that the quantum efficiency QE of p^+-i-n (closed symbols) a-Si:H solar cells degrades about 48.6 % of its original values, while the insertion of a buffer layer limits this degradation to only 25.3 %.
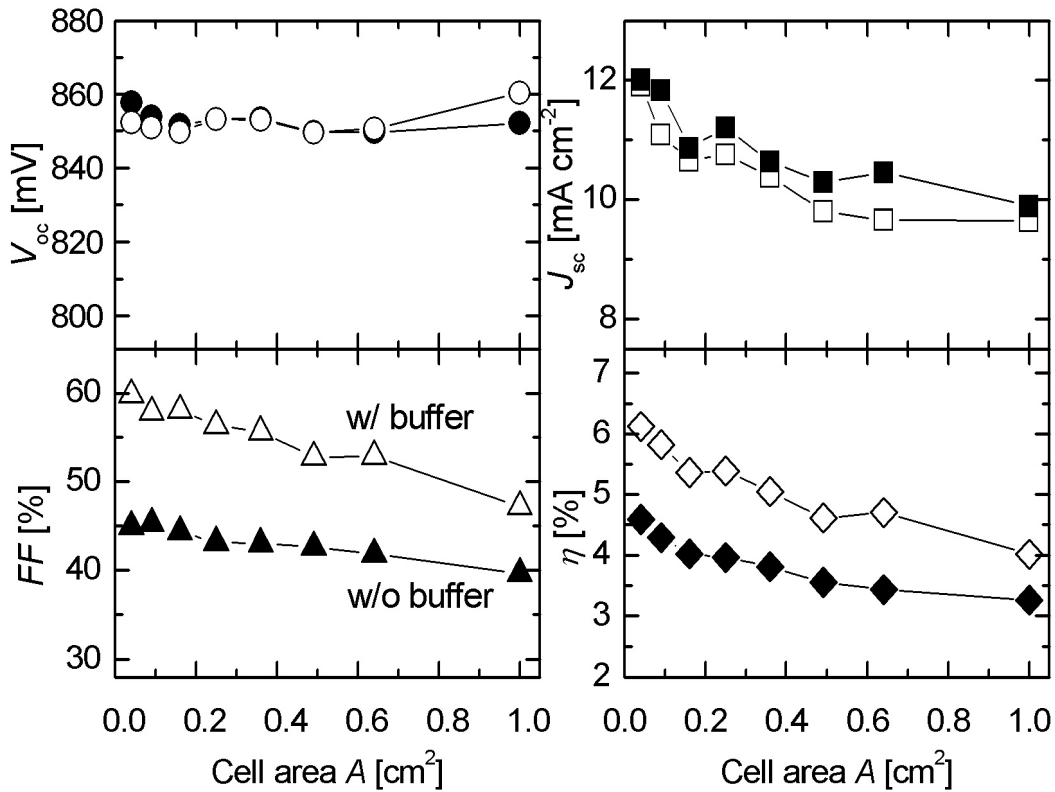
Fig. 3.32: Beneficial effect of insertion of p-type a-Si:H buffer layer (open symbols) between the p-type μc-Si:H layer and the i-layer: the open-circuit voltage V_{oc}, the short-circuit current density J_{sc}, the fill factor FF, and the efficiency η for different solar areas. The incorporation of p-type a-Si:H layer enhances efficiency η by improving both the fill factor FF and the open-circuit voltage V_{oc} although the short-circuit current density J_{sc} decreases due to the small absorption of this layer.

Since the parallel resistance R_p in a-Si:H solar cells represents the leakage throughout the i-layer, Fig. 3.34 shows a comparison between the deduced values of parallel resistance R_p from the output characteristics for both cases, i.e. with and without buffer layer. Fig. 3.34 proves that inserting a buffer layer clearly enhances the parallel resistance R_p of a-Si:H solar cells and therefore decreases the leakage within the i-layer.

3.3.2   Back contact of n-i-p a-Si:H solar cells

This subsection analyzes the effect of the back contact on the performance of a-Si:H solar cells. Fig. 3.35 shows the structure of the n-i-p a-Si:H solar cells where the
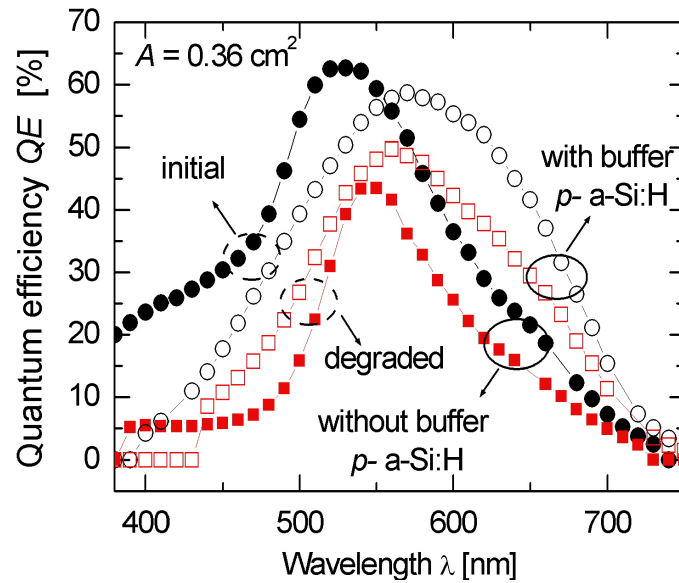
Fig. 3.33: Quantum efficiency QE of an a-Si:H solar cell showing the effect of the *p*-type a-Si:H buffer layer. The cells are degraded under an AM1-like spectrum at 50 °C for 24 hours. The QE of a-Si:H solar cells without a *p*-type buffer layer (closed symbols) suffers a degradation of 48.6 %, whereas inserting a *p*-type buffer layer (open symbols) decreases the degradation to 25.3 %.

back contact in Fig. 3.35a is Asahi-U ($\sim$ 700 nm), Fig. 3.35b is Al ($\sim$ 500 nm), Fig. 3.35c is Cr($\sim$ 10 nm)/ZnO:Al($\sim$ 70 nm), and Fig. 3.35d is Cr($\sim$ 10 nm)/Al($\sim$ 500 nm)/ZnO:Al($\sim$ 70 nm).

   The corresponding J/V-characteristics of the solar cells of Fig. 3.35 are measured and compared in Tab. 3.1. In Fig. 3.35b, the aluminium Al is directly evaporated on glass. The disadvantage of this, is that the probability of forming pin holes during the deposition is high enough to shunt the solar cell and therefore the characteristics of the corresponding cell are bad as shown in Tab. 3.1. To solve this problem, I insert a very thin layer of chromium Cr of about 10 Å between the Al layer and the glass for better adhesion. This enhances the resulting characteristics of the a-Si:H cell. A step further in enhancing the performance of *n-i-p* a-Si:H solar cells, I deposit an ZnO:Al layer between the Al layer and the *n*-layer, as shown in Fig. 3.35d. This enhances the absorption of the photons due to the increase of the reflection at the back contact of the cell reflected in the increase of J_{sc} as clearly evident from in Tab. 3.1.

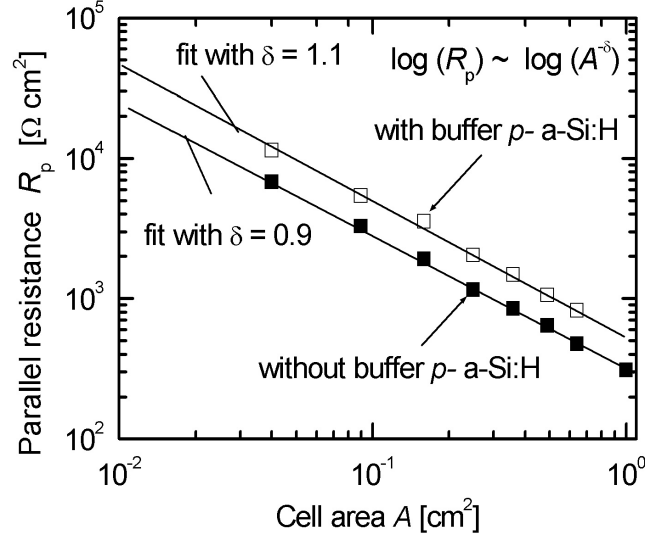**Fig. 3.34:** Parallel resistance R_{p} (symbols) of a-Si:H solar cells showing that the insertion of p- a-Si:H buffer layer (open symbols) between the p-type μc-Si:H layer and the i-layer reproducibly enhances the parallel resistance R_{p} for different cell areas A. The parallel resistance R_{p} is experimentally fitted (lines) using the empirical relation: $R_p \sim A^{-\delta}$.

Tab. 3.1: Comparison between the characteristics of similar n-i-p cells deposited on different back contacts.

Substrate type	Cell area [cm^2]	V_{oc} [mV]	J_{sc} [mA cm^{-2}]	FF [%]	η [%]
(a)	0.49	889	9.2	49.0	4.2
(b)	0.09	685	8.1	27.9	1.5
(c)	0.49	872	8.2	48.8	3.5
(d)	0.52	887	10.2	54.4	4.9
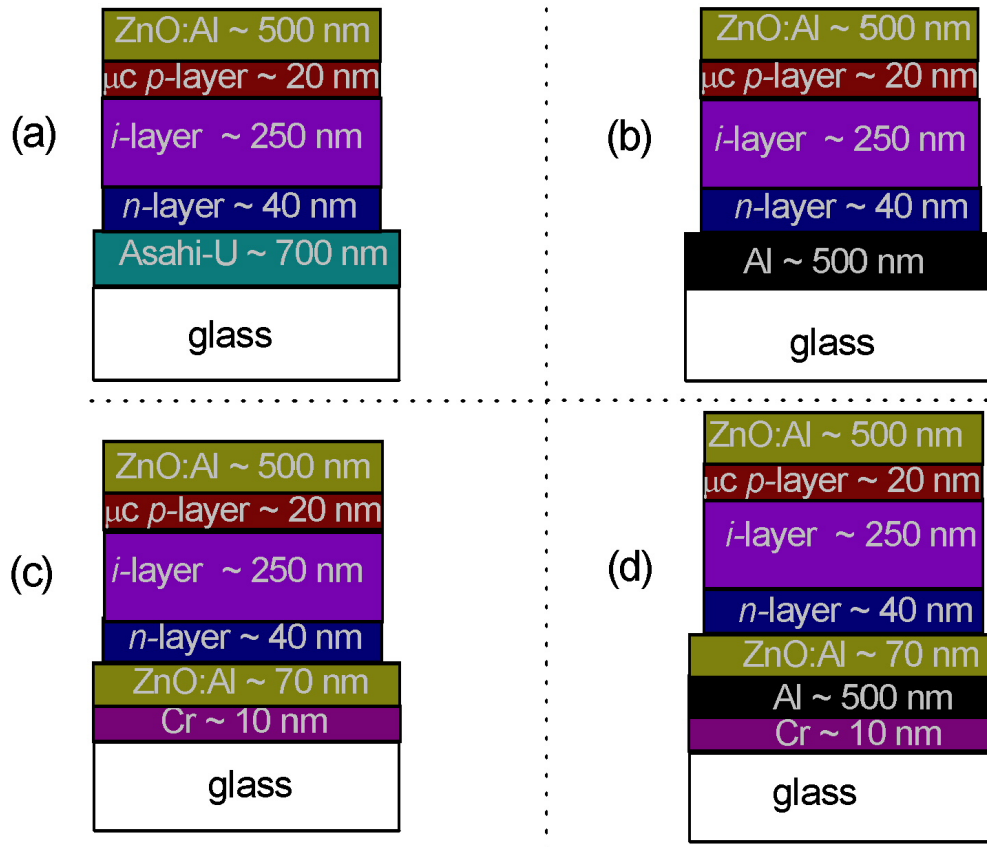
Fig. 3.35: Similar *n-i-p* a-Si:H solar cells deposited on glass-coated a) Asahi-U, b) Al, c) Cr/ZnO:Al, and d) Cr/Al/ZnO:Al to investigate the effect of the back contact on the cell performance.

3.4 Flexible solar cells

3.4.1 Heating PET substrates

Since the release of adsorbed gases or moisture from polymer substrates during the deposition of the solar cells deteriorates the quality of the a-Si:H, especially the *i*-layer, the substrates were pre-heated inside a vacuum chamber and the corresponding pressure increase was measured. Plastic substrates consist of hydrocarbon molecules which release their additives, such as oxygen, hydrogen and water vapor, as soon as the substrates are heated [107]. It is assumed that H_2O occluded in the substrates to release and decompose causing oxygen atoms to be incorporated in the a-Si:H films as dopants [108]. Those additives contaminate the vacuum chamber during the deposition of a-Si:H-based materials and therefore affect the optoelectronic properties of a-Si:H by increasing its defect density [109–111]. Therefore, before the deposition of a-Si:H is carried out, the plastic substrates should be outgassed, i.e. preheated outside the deposition chambers.

Fig. 3.36 shows the increase of the chamber pressure, upon heating of the PET substrates, from $P_r = 10^{-6}$ mbar at a heating temperature $T = 60$ °C to $P_r = 10^{-3}$ mbar where the heating temperature T reaches $T = 110$ °C. After about 30 minutes at $T = 110$ °C, the pressure decreases again indicating that the film is outgassed.

Fig. 3.37 shows the monitoring of the residual gases from heated PEN substrates using a residual gas analyzer (RGA). In the first 60 minutes, the outgassing of the PEN substrate is constant at $T = 27$ °C. Between the minutes 60 and 190, the temperature reaches $T = 100$ °C in the chamber and the pressure of some relevant gases rises. The outgassing of H_2O increases to a pressure of $P_r = 10^{-4}$ Torr and H_2 to $P_r = 10^{-6}$ Torr. O_2 shows no increase at these temperatures. After 190 minutes the temperature reaches $T = 150$°C which is close to the glass transition temperature T_g of PEN. H_2O and H_2 pressures increase again, but also the O_2 increases, which is interpreted as the beginning of the break down of the PEN structure.

The basic conclusion is therefore, that before the deposition of a-Si:H is carried out, it is necessary to outgas the plastic substrates in order to make sure that possible contamination is released before the deposition process.
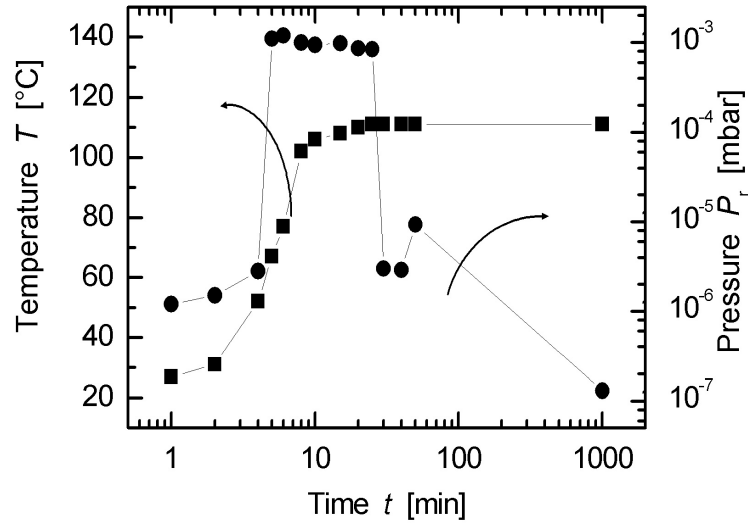
Fig. 3.36: Dependence of the heating temperature T (squares) and the chamber pressure P_r on the heating time t of PET substrate. The pressure of the heating chamber starts to increase due to the increase of the outgassing of the PET which seems to decrease after about 30 minutes of heating the PET substrate at temperature of $T = 110$ °C.

3.4.2 Thin films on plastic substrates

Interaction between a-Si:H films and substrate

The main purpose of this subsection is to find how to keep the substrates flat after the fabrications of the a-Si:H films, i.e. to maximize the value of the radius R in Eq. (2.16). This can be done by

- maximizing the thickness d_s of the substrate,

- minimizing the thickness d_f of the film,

- minimizing the temperature difference Δ_T, i.e. decreasing the deposition temperature of a-Si:H films,

To study the curvature of the PET and PEN substrates, I deposited a-Si:H films with different thicknesses $d_f \sim [100, 500, 1000]$ nm on different thicknesses $d_s \sim [23, 50, 125]$ μm of PET and $d_s \sim [25, 50, 100]$ μm of PEN substrates. I attach the PET and PEN substrates on a rigid carrier, glass in this case, to suppress the bending of the substrates during the deposition of a-Si:H films. The substrates are
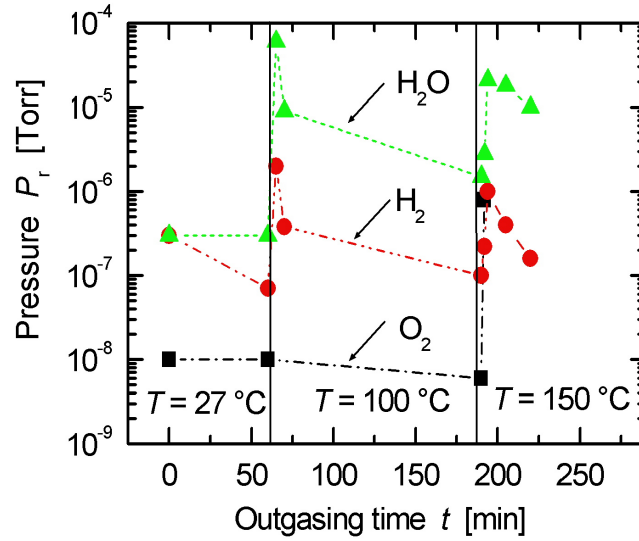
**Fig. 3.37:** Outgassing process of PEN substrate showing the chamber pressure P_r for three regions of temperatures. In the first region where the heating temperature is around room temperature $T = 27$ °C, the outgassing is constant. As soon as the heating temperature reaches $T = 100$ °C, the water vapor H_2O increases the pressure to 10^{-4} Torr and H_2 to 10^{-6} Torr. On the other side, the O_2 does not affect the pressure. After 190 minutes the temperature reaches $T = 150$ °C which is close to the glass transition T_g of PEN. H_2O and H_2 pressures increase again, but also the O_2 increases, which could be interpreted as beginning of the break down of the PEN structure.

fixed on the glass using adhesive whose glass transition temperature is much higher than of the substrates themselves. After the deposition of the film on the substrate took place, I remove the adhesive and track the changes occurred to the shape of the substrates, see Fig. 3.38, and then measure the resulting radius R of the substrates.

I deposited a-Si:H on three PET substrates of thicknesses $d_s = 23$ μm, 50 μm, and 125 μm. The thicknesses d_f of the a-Si:H films range from 50 nm up to 800 nm. Fig. 3.39 shows that depositing a-Si:H on PET substrate which has a thickness d_s of 23 μm yields smaller radii R than on thicker substrates. The PET substrate is flat for the case when the thickness of the a-Si:H is less than 100 nm, i.e. the radius is very large.

Fig. 3.40 compares between the resulting radius R of a-Si:H coated PET and PEN substrates of equal thickness, $d_s = 25$ μm, when the thickness of the a-Si:H film ranges between 30 nm and 400 nm. The measured values of the resulting radius
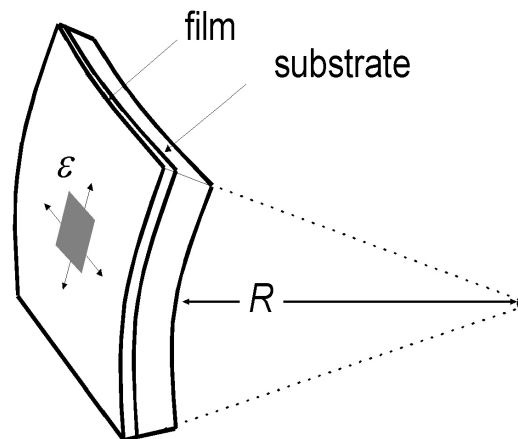
Fig. 3.38: Sketch of a-Si:H film deposited on flexible substrate where the structure bends to have a cylindrical form of a radius R leading to produce a strain ε on the surface of a-Si:H film.

R of the PEN substrates are larger than those of PET substrates. This result is consistent with the expectation from Eq. (2.22).
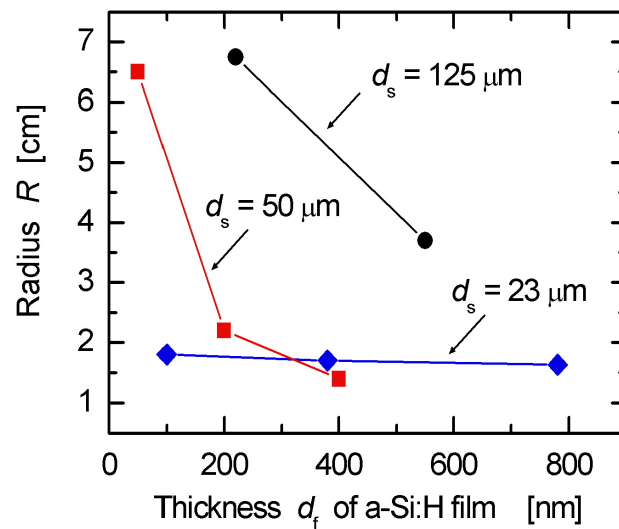
Fig. 3.39: Measured radius R of PET substrates as a function of the thickness d_f of the a-Si:H films on top. The radius R decreases as the thickness d_s of the substrate gets smaller. The PET substrates remain flat for the case where $d_f = 100$ nm.
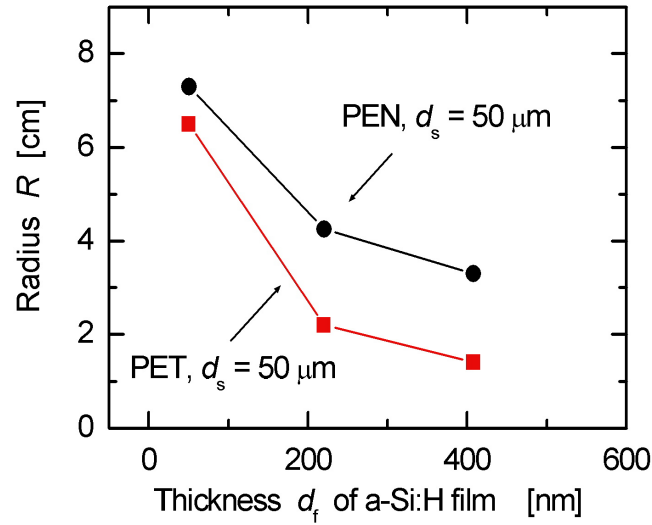
Fig. 3.40: Comparison between the measured radius R of PET and PEN substrates as a function of the thickness d_f of the a-Si:H films. The thicknesses d_s of the substrates are 50 μm. The PEN substrates show a better performance than of the PET ones since the radius R of the PEN substrates exhibit larger values than for the PET substrates.

ZnO:Al coating

One of the deposition parameters that affects the growth of ZnO:Al is the deposition pressure P_r inside the chamber. To test the effect of the deposition pressure P_r on the PET substrates, I varied P_r from 2 mTorr to 30 mTorr and then investigated the resulted curvature of the substrates. The thickness of the ZnO:Al films was about 450 nm and the thickness of the PET substrates was 23 μm. Fig. 3.41 shows that to decrease the bending of the substrate, the deposition pressure during ZnO:Al sputtering has to be as large as possible.

3.4.3   a-Si:H solar cells on PET substrates

I deposit an a-Si:H solar cell of optimized layers on PET substrates, where the thicknesses of the substrates are 23 μm and 50μm. The substrates were preheated at 200 °C for 30 minutes in a vacuum chamber to get rid off the gases from the substrates. Fig. 3.42 shows the output characteristics of the solar cells deposited on the PET substrates. The cells on thinner PET substrates show a better performance than those on thicker substrates due to the lower amount of contamination from the
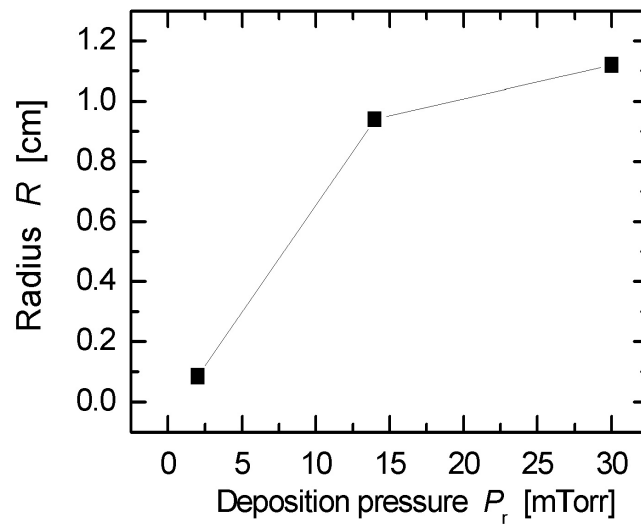
Fig. 3.41: Radius R of PET substrates as a function of the deposition pressure R_r of ZnO:Al films. The thicknesses d_s of the substrate is 23 μm. The increase of R_r decreases the bending of the substrate and therefore the radius R increases.

substrate.

The current density/voltage (J/V) characteristics shown in Fig. 3.42 are measured in the J/V-setup of CIGS solar cells, refer to subsection 2.3.2, and therefore are calibrated using the photogenerated current from the spectral response of the solar cells from quantum efficiency measurements. Fig. 3.43 shows the quantum efficiency of the a-Si:H solar cell deposited on PET substrate of thickness $d_s = 23$ μm
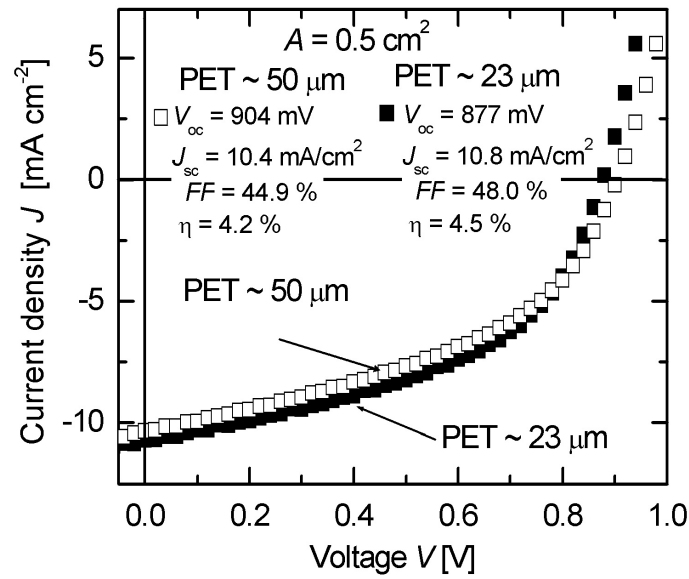
Fig. 3.42: Current density/voltage (J/V) characteristics of a-Si:H solar cell of area $A = 0.5$ cm^2 deposited on PET films which have thicknesses of 23 μm (closed symbols) and of 50 μm (open symbols). The fill factor FF of a-Si:H solar cells deposited on PET of 50 μm is lower than that on PET of 23 μm due the increase of the contamination as the thickness of the PET films increases.
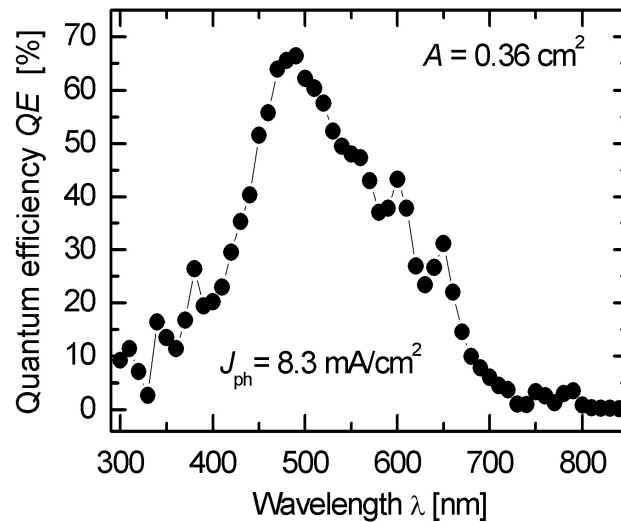
Fig. 3.43: Quantum efficiency of an a-Si:H solar cell of area $A = 0.36$ cm^2 deposited on flexible PET substrate of 23 μm thicknesses.

3.5 Parasitic resistances of a-Si:H solar cells under different illumination intensities

This section studies the behaviour of the parallel resistance R_p and the series resistance R_s under different illumination intensities.

The conventional method of calculating R_s, represented in [112] and summarized in Appendix 5.3, is called Werner plot. The Werner plot is a plot of the small signal conductance which is divided by the current density G/J versus the conductance G. If the abovementioned dependency has a curvature, the determination of R_s depends on the region of fitting and therefore results in different values. In the following subsections, I express the dependency of the parallel resistance R_p on the illumination intensity Φ, also I present an alternative method of determination of R_s without having the problem of curvature.

3.5.1 Modelling the parallel resistance

In this subsection, I explain the dependence of R_p on the illumination intensity Φ. Due to the construction and layer sequence of a-Si:H based thin film solar cells, considering the parallel resistance R_p to be distributed over the whole area of the solar cell, seems to be a well justified assumption. Under this assumption, R_p relates to the photoconductivity σ_{ph} of the intrinsic layer. The photoconductivity σ_{ph} is defined as

$$\sigma_{ph} = q(\mu_n n_{ph} + \mu_p p_{ph}), \tag{3.20}$$

where the densities n_ph and p_ph of the photogenerated carriers depend on the photogeneration rate G_ph [113] as

$$n_\mathrm{ph} \sim (G_\mathrm{ph})^{\gamma_n}, \tag{3.21a}$$

$$p_\mathrm{ph} \sim (G_\mathrm{ph})^{\gamma_\mathrm{P}}, \tag{3.21b}$$

with γ_n and γ_p being material dependent constants. Inserting Eq's. (3.21a) and (3.21b) into Eq. (3.20) leads to

$$\sigma_\mathrm{ph} \sim (G_\mathrm{ph})^{\gamma}, \tag{3.22}$$

$$\Rightarrow \quad \gamma = \frac{\partial log(\sigma_\mathrm{ph})}{\partial log(G_\mathrm{ph})}, \tag{3.23}$$

where γ is the power-law exponent of the conductivity. In this work, I found that the parallel resistance R_p (leakage through the i-layer in a-Si:H based solar cells) is a photo-resistive element and its resistance R_p is inversely proportional to the photoconductivity σ_{ph}. Therefore, using Eq. (3.22):

$$R_\mathrm{p}(\Phi) = R_p(\Phi_0) \left(\frac{\Phi}{\Phi_0}\right)^{-\gamma}, \tag{3.24}$$

$$log(R_\mathrm{p}(\Phi)) = log\left(R_p(\Phi_0)\right) - \gamma log\left(\frac{\Phi}{\Phi_0}\right), \tag{3.25}$$

where Φ_0 is the full illumination intensity delivered by the solar simulator. Fig. 3.44 displays the comparison between R_p values derived from experimental data (circles), and the modelling (solid line) of the experimental R_p data according to Eq. (3.25) with the only modelling parameter γ.

The cells in Figs. 3.44a and 3.44b have the same intrinsic layer and the corresponding power-law exponent γ is found to be equal while the cell in Fig. 3.44c has a different intrinsic layer. Therefore, the samples which have very similar intrinsic layers, have equal value of γ. On the log-log scale of Fig. 3.44, the values of $R_\mathrm{p}(\Phi)$ are linear over two orders of magnitude. They follow a power-law as expected from Eq. (3.25), and thereby support my assumption of a distributed $R_\mathrm{p}(\Phi)$.

3.5.2 Determination of ideality factor

In Werner plot, the series resistance R_s and the ideality factor n_id are evaluated simultaneously by linearly fitting the conductance divided by the current density versus the conductance, refer to step 5 in Appendix 5.3. In this work, I apply the method of different illumination levels in the calculation of the ideality factor n_id from the relationship between the open-circuit voltage V_oc and the short-circuit current J_sc as follows

$$J_\mathrm{sc} = J_0 \exp\left(\frac{V_\mathrm{oc}}{n_\mathrm{id}V_\mathrm{t}}\right) + \frac{V_\mathrm{oc}}{R_\mathrm{p}}, \tag{3.26}$$

Eq. (3.26) is rearranged as

$$\ln\left(J_\mathrm{sc} - \frac{V_\mathrm{oc}}{R_\mathrm{p}}\right) = \ln\left(J_0\right) + \frac{1}{n_\mathrm{id}V_\mathrm{t}}V_\mathrm{oc}, \tag{3.27}$$
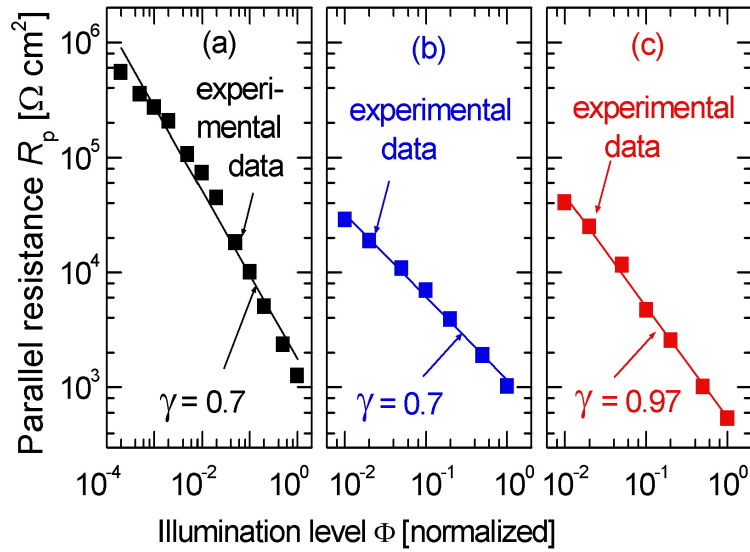
Fig. 3.44: Modelling the illumination dependence of the parallel resistance $R_{\mathrm{p}}(\Phi)$ of a-Si:H solar cells using Eq. (3.25). The decrease of $R_{\mathrm{p}}(\Phi)$ follows a power law. The experimental R_{p} data (circles) are derived from the inverse slope of the J/V-characteristics at $V = 0$, while my model (solid lines) explains the illumination-dependent parallel resistance with the modelling parameter γ. The cells in a) and b) have the same deposition conditions of the intrinsic layer, while the cell in c) has a different intrinsic layer.

The ideality factor n_{id} is determined directly from linearly fitting the L.H.S. of Eq. (3.26) (in the logarithmic scale) with the open-circuit voltage V_{oc} (in the linear scale) in the R.H.S. of the same equation. Fig. 3.45 shows that the ideality factor is independent of the illumination intensity Φ and it can be directly determined from the slope of the data. Therefore, I apply the method of different illumination intensities for the determination of the ideality factor n_{id}.

3.5.3   Determination of series resistance

After determining the value of the ideality factor n_{id}, the series resistance is evaluated from Eq. (3.28) by fitting the term $\ln\left(J + J_{\mathrm{sc}} - V/R_{\mathrm{p}}\right) - \ln\left(J_0\right)$ versus the current density J. The series resistance R_{s} equals to the slope of the data, in Fig. 3.46, multiplied by the ideality factor n_{id}, which is evaluated from Eq. (3.27), and the thermal voltage V_{t}.
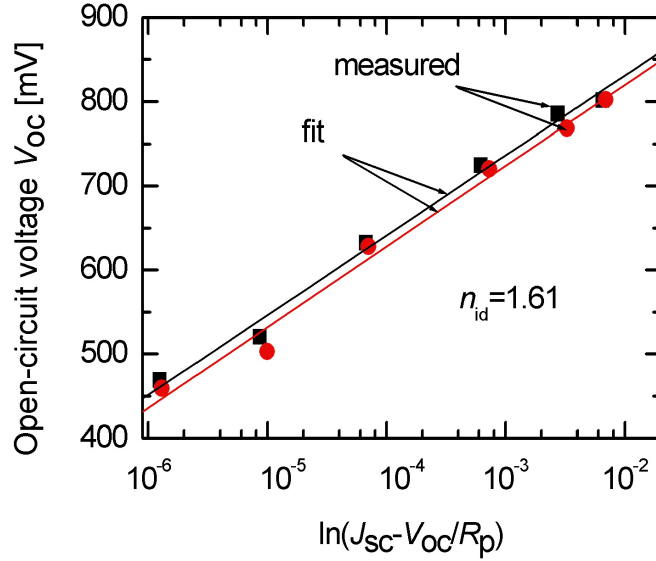
Fig. 3.45: Calculation of the ideality factor n_{id} from the slope of the fitted data at different illumination intensities. The data of the same solar cell but for two different positions on the superstrate are plotted in order to justify the calculation of the ideality factor.

$$\ln\left(J + J_{sc} - \frac{V}{R_p}\right) - \ln\left(J_0\right) = -\frac{R_s}{n_{id}V_t}J, \tag{3.28}$$

Fig. 3.46 shows the resulting curves calculated from Eq. (3.28) which are easily linear fitted.

3.5.4 Comparison between the Werner plot and the alternative method

This subsection compares the values of the series resistance R_s and the ideality factor n_{id} calculated from Werner plot and the alternative method according to section 3.5.2. Fig. 3.47 shows that the series resistance R_s does not follow a clear trend as a function of the illumination intensity for both samples in Fig. 3.47a and in Fig. 3.47b. The deposition temperature T_{dep} of the i-layer of sample (a) is 135 °C while it is 120 °C for sample (b). The rest of the deposition conditions of both samples were kept constant. The decrease of the deposition temperature T_{dep} is reflected on the increase of values of the series resistance R_s as shown in Fig. 3.47.
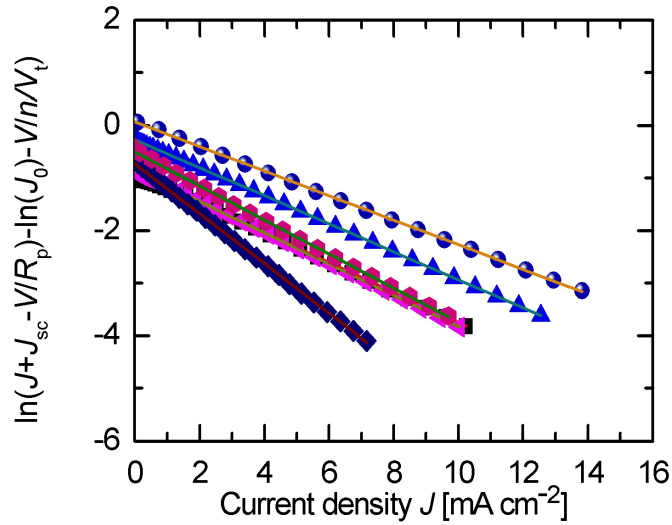
Fig. 3.46: Calculation of the series resistance R_{s} by the alternative method from the slope of the fitted data at different illumination intensities.
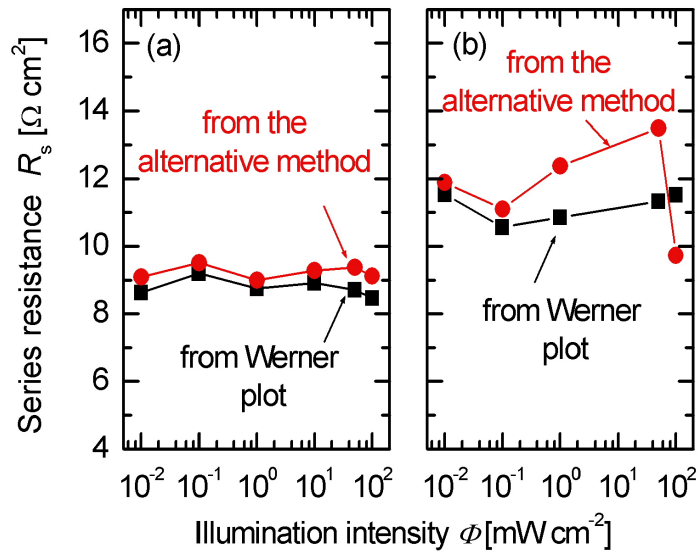
Fig. 3.47: A comparison between the calculated series resistance R_{s} from the Werner plot and from the alternative method represented by Eq. (3.28). a) is for sample M060331-1, while b) is for sample M060327-1.

The linear behaviour of the relation between the L.H.S. and the open-circuit voltage V_{oc} of Eq. (3.27) leads to the conclusion of the independency of the ideality factor n_{id} on the illumination intensity Φ. The evaluated values of ideality factor

n_{id} from the Werner plot, refer to step 5 of Appendix 5.3 shows that the ideality factor increases at higher illumination intensities Φ. Fig. 3.48 compares between the calculated values of the ideality factor n_{id} from the Werner plot and the alternative method.
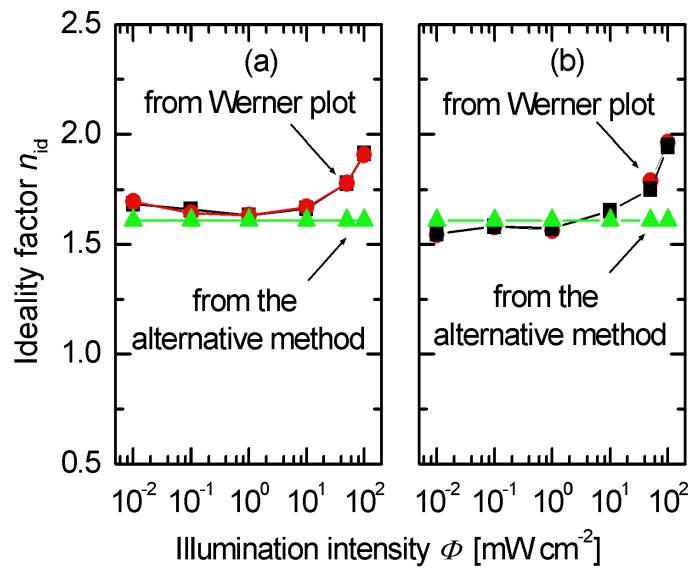
Fig. 3.48: Calculation of ideality factor n_{id} from Werner plot (circles and squares) compared to the alternative method (triangles). a) is for sample M060331-1, while b) is for sample M060327-1.

# 3.6 Characterization of amorphous silicon based modules

This section investigates the performance of amorphous silicon based photovoltaic modules by separating the shunting effects of individual component cells inside the module under different illumination intensities Φ. In a completed thin film photovoltaic module, several component cells are series connected without granting access to the electrical contacts of each individual cell. The considerations start from the most simple equivalent circuit model of a real solar cell including series and parallel resistances. Measurements of the current-voltage characteristics yield an illumination-intensity dependent parallel resistance $R_p(\Phi)$ rather than a constant one, cf. section 3.5.1. The decrease in parallel resistance R_p with illumination intensity Φ follows a power law which I ascribe to the photoconductivity of parallel resistances distributed over the whole solar cell area. I characterize the parallel resistance of each cell inside a module without accessing the contacts of each cell. Physically contacting individual cells requires removal or destruction of the lamination, which I avoid by recording the global current density vs. voltage characteristics of the whole module. During the measurement, each component cell is subsequently exposed to a reduced illumination intensity Φ while all other cells of the module are fully illuminated. Testing this partial shading method on three different types of commercial thin film modules yields the parallel resistances of the individual component cells inside the modules, and proves useful for identifying quality problems, e.g. laser scribing induced defects.

In this section, I will i) study the parallel (frequently denoted as shunt resistance) resistance R_p under different illumination intensities Φ, ii) track the effect of shunting one component cell on the global current density vs. voltage J/V-characteristics of a module; and iii) characterize each cell of the series-connected cells of the series-connected module by global J/V measurements on the module.

3.6.1 Effect of shunting a solar cell on the module

An important feature of thin film photovoltaics (PV) is the possibility of establishing an electrical series connection of the individual solar cells in a photovoltaic module by monolithic integration during the manufacturing process [114,115]. Most applications need this electrical series connection for the PV modules to provide a sufficiently high output voltage for operating common loads and devices. In this

subsection, I track the effect of shunting one component cell on the global current density vs. voltage (J/V) characteristics of a module. Fig. 3.49 presents the equivalent circuit generally applied for photovoltaic modules; it consists of M current sources $I_{ph,i}$, $(1 = i = M)$ in parallel to M diodes, where M is the number of the series-connected a-Si:H solar cells in the module. When including the resistive elements $R_{s,i}$ and $R_{p,i}$, the circuit of Fig. 3.49a reasonably well represents the behavior of real solar cell [57]. Fig. 3.49b simplifies the representation of each solar cell element by a box and then introduces a virtual external shunt to the component cells inside the module in order to separate the effects of the individual component cells.

(a)   (b)
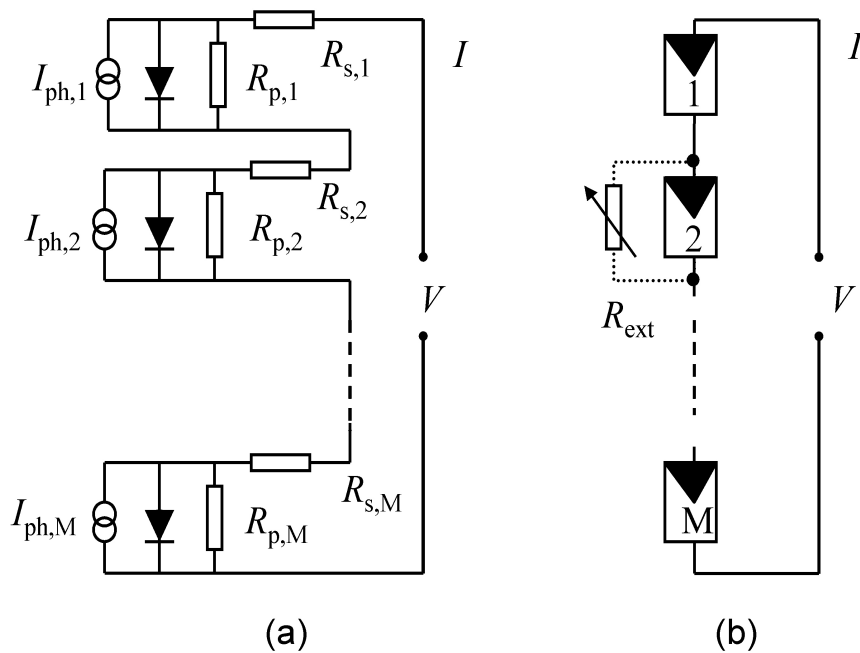
Fig. 3.49: Equivalent circuit for thin film photovoltaic modules; a) consisting of M-cells connected in series, and b) incorporating a virtual external shunt resistance R_{ext} to mimic shunting a single cell.

To illustrate the effect of shunting one solar cell within the module on the output characteristics of the whole module, I add a virtual external resistance R_{ext} to the measured J/V-characteristics of a single component cell and then recalculate the J/V-characteristics of the whole module for different values of R_{ext}. Small values of R_{ext} in Fig. 3.50(a)a represent bad quality (shunted) solar cells where the open-circuit voltage V_{oc} of the corresponding cell drastically decreases [116], and therefore the generated power density of the whole module consequently deteriorates as shown

in Fig. 3.50b.
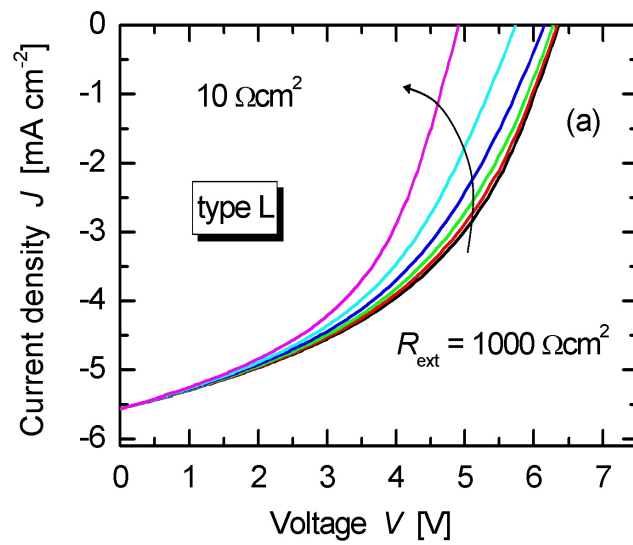
(a)
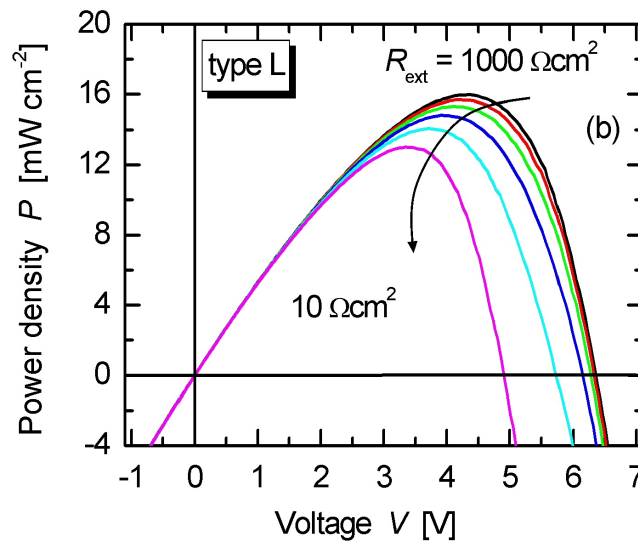
(b)

Fig. 3.50: a) Current density/voltage (J/V) characteristics (type L); and b)the corresponding electrical output power density P (type L3) of a complete module recalculated for different values of the virtual external resistance R_{ext} according to Fig. 3.49b. The external resistance R_{ext} simulates the shunts of the corresponding solar cell. The figure clearly illustrates the loss in V_{oc} due to one shunted cell only, which drastically decreases the electrical output power of the whole module.

Due to the wide spread applications of a-Si:H solar cells and modules at low illumination conditions, I explain here the effect of R_{ext} on the open-circuit voltage V_{oc} under different illumination conditions.

Under open-circuit conditions, i.e. $J = 0$, the correlation between the open-circuit voltage V_{oc} of a solar cell and the short-circuit current density, and therefore the illumination intensity, is given by the relation

$$V_{oc} = n_{\text{id}} V_t \ln \left(\frac{J_{sc} - V_{oc}/R_p^{new}}{J_0} \right), \tag{3.29}$$

$$R_p^{new} = R_{ext} // R_p, \tag{3.30}$$

where n_{id}, V_t, J_{sc}, and J_0 are the diode ideality factor, the thermal voltage which equals to 25.9 meV at room temperature, the short-circuit current density, and the saturation current density, respectively. The illumination dependence of $V_{\text{oc}}(\Phi)$ in Eq. (3.29) is linear in the semi-log scale as long as the value of $V_{\text{oc}}/R_{\text{p}}^{\text{new}} \ll J_{\text{sc}}$, i.e. the solar cell exhibits a sufficiently high parallel resistance R_{p}. Decreasing the value of R_{ext}, and therefore $R_{\text{p}}^{\text{new}}$, breaks the linearity in the semi-log scale of the relation in Eq. (3.29) and the open-circuit voltage starts to decrease more rapidly with decreasing illumination intensity Φ, as shown in Fig. 3.51. Therefore, the study of shunting effect is essential especially at lower illumination intensities.

Fig's. 3.50 and 3.51 illustrate the effect of defective component cells, or lowering shunt resistances in single component cells of a monolithically series-connected thin film module. Both figures start from measured global J/V-characteristics of a type L module, and recalculate the module performance after adding different values of virtual external shunt resistances R_{ext}.

3.6.2 Experimental setup

I test my method on three different types of commercial a-Si:H based thin film modules: Module type L incorporates four series-connected tandem cells. Type N comprises a series connection of twelve single p-i-n cells, and type S contains five single cells in series connection.

The previous method is applied to modules (type L) where one can access the contacts of each solar cell of the module by removing some the lamination just over the contacts. However, removal of lamination may lead to damage the connection of the series-connected cells of the module (e.g type N) and destruction of the modules
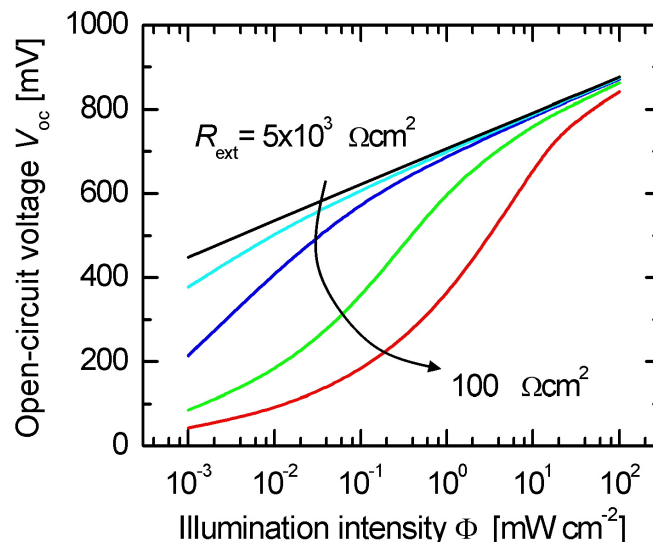
Fig. 3.51: Open-circuit voltage V_{oc}, calculated from using Eq. (3.29), for different illumination intensities Φ and different values of an external resistance R_{ext}. The decrease of R_{ext} lets the open-circuit voltage V_{oc} decrease more rapidly with decreasing illumination intensity Φ.

is generally not acceptable for industrial testing. Therefore, I propose a partial shading for characterizing the performance of each component cell as a convenient and destruction-free method of module testing.

In this work, I analyze the different modules under halogen lamp illumination with an intensity close to AM1.5, but under spectral conditions which are significantly red-shifted with respect to an AM1.5 solar spectrum. A relatively simple experimental realization for introducing the virtual external shunt of Fig. 3.49b, is subsequent partial shading of the individual component cells in the module. Therefore, I fully illuminate *M-1* cells, whereas only one cell is partially shaded by a neutral density filter with an optical transmission of 20 % which is moveable along the module, refer to Fig. 3.52. I subsequently measure the global J/V-characteristics of the module for $m = 1 \ldots M$ with *M-1* cells being 100 % illuminated at a time, and only cell m facing a 20 % illumination intensity. The corresponding global J/V data then subsequently yield the parallel resistances of the shaded cells.
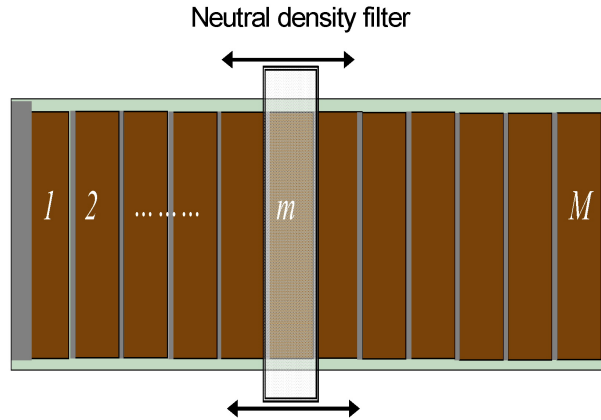
Fig. 3.52: *M-1* fully Illuminated series-connected a-Si:H solar cells in a photovoltaic module. Only one m cell ($1 \leq m \leq M$) is partially illuminated using a neutral density filter (optical transmission of 20%).

3.6.3   Characterization of modules

In this subsection, I verify my analytical model of $R_p(\Phi)$ on two types of modules (types N and L) under varying the illumination intensity Φ. Experimentally, the intensity is adjusted by changing the distance r between the light source and the module position. Fig. 3.53 shows that the short-circuit current density J_{sc} of type L modules is lower than that of type N since the component cells of the latter type consist of tandem devices with two *p-i-n* diodes stacked on top of each other.

The model well fits the illumination-intensity dependence of the parallel resistance $R_p(\Phi)$ by adjusting the value of the power-law exponent γ of the photoconductivity. Fig. **??** compares the parallel resistance R_p of type N modules under different illumination intensities Φ, derived from the slope of the J/V-characteristics at short-circuit ($V = 0$), with the modelled data using $\gamma = 0.79$ (solid line).

3.6.4   Tracking the quality of series-connected cells

Before experimentally investigating the performance of each component cell of a series-connected a-Si:H module, I describe the parallel resistance R_p of the module as a function of the position of the neutral density filter.

Case A:

$R_p = R_{p,\text{module}}(\Phi_1)$ with $\Phi_1 = \Phi_0$, i.e. the whole module is fully illuminated.
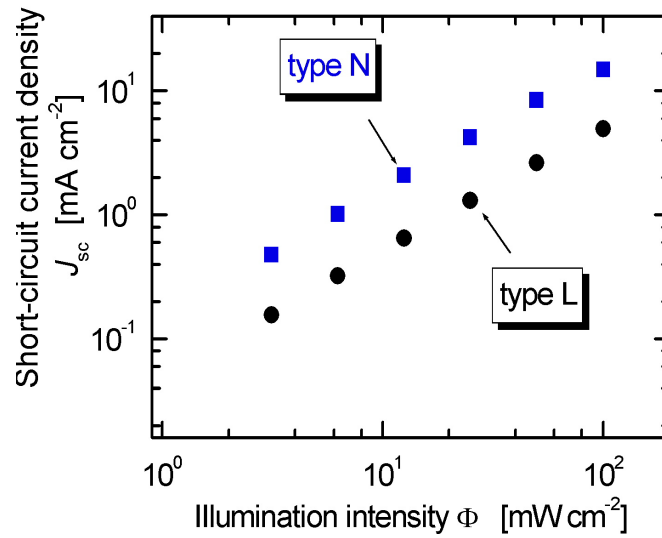
Fig. 3.53: Intensity dependence of the short-circuit current density J_{sc} of two types of modules (type N and type L). The illumination intensity Φ is adjusted by changing the distance between the module position and the light source.
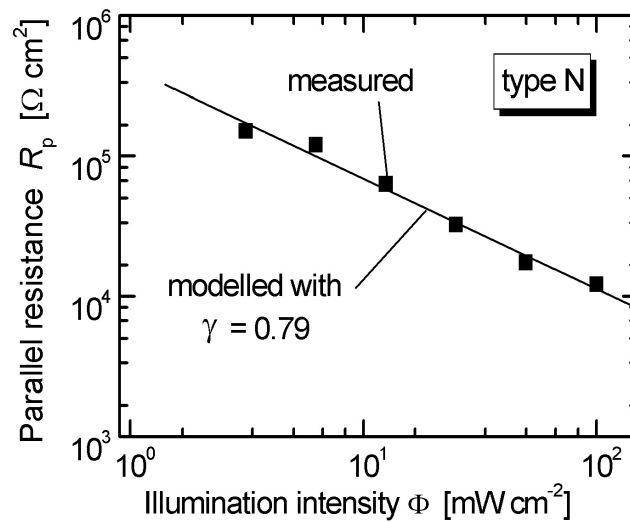
Fig. 3.54: Calculated parallel resistance R_p (symbols) of the module of type N under different illumination intensities Φ are modelled (line) by Eq. (3.25) applying $\gamma = 0.79$.

Case B:

$R_\mathrm{p} = R_\mathrm{p,partial}$ with *M-1* cells of the module being illuminated at $\Phi_1 = \Phi_0$, but cell m being shaded to $\Phi_2 = 0.2\,\Phi_0$.

The parallel resistance of the complete module $R_\mathrm{p,module}$ is defined as the sum of the parallel resistances of the series-connected component cells

$$R_\mathrm{p,module} = \sum_{i=1}^{M} R_\mathrm{p,i}(\Phi_1), \tag{3.31}$$

$$= \sum_{i=1,\,i\neq m}^{M} R_\mathrm{p,i}(\Phi_1) + R_\mathrm{p,m}(\Phi_1) \tag{3.32}$$

where $R_\mathrm{p,m}(\Phi_1)$ with $(1\leq m \leq M)$ is the parallel resistance when cell m is fully illuminated at $\Phi_1 = \Phi_0$. According to Eq. 3.24, I express the parallel resistance $R_\mathrm{p,m}(\Phi_2)$ of cell m under $\Phi_2 = 0.2\,\Phi_0$ as follows

$$R_\mathrm{p,m}(\Phi_2) = 0.2^{-\gamma} R_\mathrm{p,m}(\Phi_0) \tag{3.33}$$

and

$$R_\mathrm{p,m}(\Phi_1) = 1^{-\gamma} R_\mathrm{p,m}(\Phi_0). \tag{3.34}$$

Relating $R_\mathrm{p,m}(\Phi_1)$ to $R_\mathrm{p,m}(\Phi_2)$ by combining Eq's (3.33) and (3.34) leads to

$$R_\mathrm{p,m}(\Phi_1) = 5^{-\gamma} R_\mathrm{p,m}(\Phi_2). \tag{3.35}$$

Therefore, the parallel resistance in case B is written as

$$R_\mathrm{p(module)}^{*} = \sum_{i=1,\,i\neq m}^{M} R_\mathrm{p,i}(\Phi_1) + R_\mathrm{p,m}(\Phi_2). \tag{3.36}$$

Inserting Eq. (3.36) into Eq. (3.35) results in

$$R_\mathrm{p(module)}^{*} = R_\mathrm{p(Module)}(\Phi_1) + (5^{\gamma} - 1)\,R_\mathrm{p,m}(\Phi_1). \tag{3.37}$$

I conclude from Eq. (3.37) that the higher second term is, the better the corresponding cell m ($1 \leq m \leq M$) will be. Therefore, this method characterizes the parallel resistance of each cell of the module without accessing the contacts of the single component cells. Fig. 3.55 shows the parallel resistance $R_\mathrm{p} = R_\mathrm{p,partial}$ (squares) of a type S module. Each data point in Fig. 3.55 represents one measurement with the corresponding cell shaded to $\Phi_2 = 0.2 \, \Phi_0$ whereas all other cells of the module are fully illuminated at $\Phi_1 = \Phi_0$. Full illumination of all cells in the module results in $R_\mathrm{p(Module)}(\Phi_1)$ (circle) according to case A defined above. Fig. 3.55 proves that my method is suitable for testing the module quality. It reveals the best cell of the module being cell 4, and cell 1 causing most of the losses.
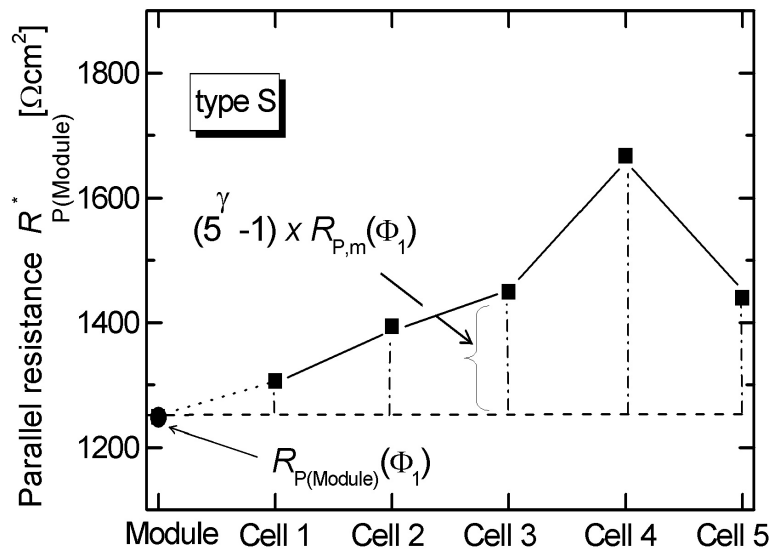
Fig. 3.55: Parallel resistance $\widetilde{R}_{\mathrm{p}(Module)}^{(\mathrm{m})}$ (square symbols) of module where each data means that the corresponding cell is only 20% illuminated while the other cells of the module are 100% illuminated. The circle symbol means that the whole module is 100% illuminated.

Chapter 4

Conclusions

The feasibility of growing a-Si:H films at low deposition temperatures on inexpensive flexible foils, motivates the study of mechanical strain in a-Si:H films on flexible foils. The a-Si:H films deposited on polyethylene naphtalene foils show a better performance than those deposited on polyethylene terephtalate, since they exhibit less resulting curvature. This thesis characterizes and optimizes a-Si:H single layers as well as a-Si:H solar cells deposited by PECVD at low deposition temperatures.

The resulting photovoltaic conversion efficiency of an a-Si:H solar cell having an optimized intrinsic layer amounts to $\eta = 6.8$ % at a deposition temperature $T_{\mathrm{dep}} = 180$ ºC. The hydrogen dilution for growing the optimum intrinsic layer is $R_{\mathrm{H}} = 2.5$. The deposition pressure P_{r} affects the mean free path length of dissociated silane atoms. Optimizing P_{r} yields an efficiency of $\eta = 5.9$ % at a deposition temperature $T_{\mathrm{dep}} = 135$ ºC. To overcome the deterioration of a-Si:H film quality at low deposition temperatures, a higher hydrogen dilution of the process gases is needed. However, to achieve homogeneous a-Si:H films at higher H_2 dilution ratios, the plasma excitation frequency has to be increased. Therefore, I investigated the very high frequency (VHF) excitation at $f = 80$ MHz. The best electronic properties of intrinsic a-Si:H layers deposited by VHF excitation occurs at $R_{\mathrm{H}} = 10$, for deposition pressures from $P_{\mathrm{r}} = 400$ mTorr to $P_{\mathrm{r}} = 200$ mTorr.

A novel analytical description of the J/V-characteristics of a-Si:H solar cells considers both diffusion and drift currents in calculating the current/voltage characteristics of a-Si:H p-i-n solar cells where the assumption of $\mu_n \tau_n >> \mu_p \tau_p$ is more accurate than of $\mu_n \tau_n = \mu_p \tau_p$ as it was used in previous analytical approaches. Due to the high absorbance of amorphous silicon based materials, the extended model accounts for the generation rate as a function of wavelength and position inside the

intrinsic layer of a-Si:H solar cells.

With the realistic assumption $\mu_n\tau_n >> \mu_p\tau_p$, the model proves that the performance of a-Si:H solar cells which are illuminated through the p-layer is better than of those illuminated through the n-layer. In addition, the intersection of electron and hole concentrations within the intrinsic layer is not centered within the i-layer. Instead, it is voltage dependent due to the assumptions of a non-uniform photogeneration rate and due to the asymmetry between the electrical properties of electrons and holes.

Moreover, this thesis studies the performance of a-Si:H-based modules under different illumination levels by analyzing their current density/voltage (J/V) characteristics as a function of the illumination intensity Φ. The measurements of J/V-characteristics yield an illumination-intensity dependent parallel resistance $R_{\mathrm{p}}(\Phi)$ rather than a constant one. The parallel resistance $R_{\mathrm{p}}(\Phi)$ follows a power law, understood by the photoconductivity of parallel resistances distributed over the whole solar cell area. I studied the parallel resistance of each cell of commercial a-Si:H modules without accessing the electrical contacts of these individual cells, by measuring the global J/V-characteristics of the module with a novel method of sequential partial shading of the component cells. Maximum and minimum values of the parallel resistances of the component cells allow for a quality control of laser scribing and cell performance.

Chapter 5

Appendices

5.1 System of differential equations

This appendix, gives necessary mathematical details of my model of calculating the current density/voltage (J/V) characteristics of p-i-n type a-Si:H solar cells. By dividing the i-layer into two regions, I solve for the minority carrier density then for the majority carriers in each region. In region R_1, the electrons are minority carriers and the continuity equation for the dark case reads

$$\frac{d^2 n(x)}{dx^2} + \frac{\mu_n F}{D_n} \frac{dn(x)}{dx} - \frac{n(x)}{D_n \tau_n} = -\frac{N_D}{D_n \tau_n} e^{\frac{V_{bi}}{V_t}\left(\frac{x-W}{W}\right)}. \tag{5.1}$$

The general solution of Eq. (5.1) is given by

$$n_{\text{Dark}}(x) \;=\; C_1 e^{\Lambda_1 x} + C_2 e^{\Lambda_2 x} + Z_1 e^{\frac{V_{bi}}{V_t}\left(\frac{x-W}{W}\right)}, \tag{5.2}$$

where Z_1 and the eigenvalues Λ_1 and Λ_2 are given by

$$Z_1 \;=\; \frac{-N_D}{D_n \tau_n \left[\left(\frac{V_{bi}}{WV_t}\right)^2 + \left(\frac{V_{bi}}{WV_t}\right)\left(\frac{\mu_n F}{D_n}\right) - \left(\frac{1}{D_n \tau_n}\right)\right]}, \tag{5.3}$$

$$\Lambda_{1,2} \;=\; -\frac{\mu_n F}{2D_n} \pm \sqrt{\left(\frac{\mu_n F}{2D_n}\right)^2 + \left(\frac{1}{D_n \tau_n}\right)}, \tag{5.4}$$

Now, I introduce the solution $n_{\text{Dark}}(x)$ into the continuity equations for the majority carriers (holes) to obtain

$$\frac{d^2 p(x)}{dx^2} - \frac{\mu_p E}{D_p} \frac{dp(x)}{dx} = \left\{ \frac{Z_1}{D_p \tau_n} - \frac{N_D}{D_p \tau_n} \right\} e^{\frac{V_{bi}}{V_t} \left(\frac{x-W}{W} \right)}$$
$$+ \frac{C_1}{D_p \tau_n} e^{\Lambda_1 x} + \frac{C_2}{D_p \tau_n} e^{\Lambda_2 x}. \tag{5.5}$$

The solution of Eq. (5.5) is

$$p_{\text{Dark}}(x) = C_5 + C_6 e^{\frac{\mu_p E}{D_p} x} + Z_3 e^{\Lambda_1 x} + Z_4 e^{\Lambda_2 x}$$
$$+ Z_5 e^{\frac{V_{bi}}{V_t} \left(\frac{x-W}{W} \right)}, \tag{5.6}$$

where

$$Z_3 = \frac{C_1}{D_p \tau_n \left[\Lambda_1^2 - \Lambda_1 \frac{\mu_p F}{D_p} \right]}, \tag{5.7}$$

$$Z_4 = \frac{C_2}{D_p \tau_n \left[\Lambda_2^2 - \Lambda_2 \frac{\mu_p F}{D_p} \right]}, \tag{5.8}$$

and

$$Z_5 = \frac{Z_1 - N_D}{D_p \tau_n \left[\left(\frac{V_{bi}}{W V_t} \right)^2 - \left(\frac{V_{bi}}{W V_t} \right) \left(\frac{\mu_p F}{D_p} \right) \right]}. \tag{5.9}$$

The solution n_{Photo} under illumination is given by the superposition $n_{\text{Photo}} = n_{\text{Photo}} + \sum_{i=0} n_i$ where n_i are the partial solutions that belong to different wavelengths λ_i each having a different absorption coefficient α_i. The following derives such partial solutions omitting the index i for convenience. I again start with the continuity equation for electrons in region R_1

$$\frac{d^2 n(x)}{dx^2} + \frac{\mu_n E}{D_n} \frac{dn(x)}{dx} - \frac{n(x)}{D_n \tau_n} = -\frac{\alpha N_{ph}}{D_n} e^{-\alpha x}. \tag{5.10}$$

The solution for $n(x)$ is

$$n_{\text{Photo}}(x) = C_1 e^{\Lambda_1 x} + C_2 e^{\Lambda_2 x} + Z_2 e^{-\alpha x}, \tag{5.11}$$

where

$$Z_2 = \frac{-\alpha N_{ph}}{D_n \left[\alpha^2 - \alpha \frac{\mu_n E}{D_n} - \left(\frac{1}{D_n \tau_n}\right)\right]}. \tag{5.12}$$

Entering Eq. (5.11) into the continuity equation for holes yields

$$\frac{d^2 p(x)}{dx^2} - \frac{\mu_p E}{D_p} \frac{dp(x)}{dx} = \left\{\frac{Z_2}{D_p \tau_n} - \frac{\alpha N_{ph}}{D_p}\right\} e^{-\alpha x}$$
$$+ \frac{C_1}{D_p \tau_n} e^{\Lambda_1 x} + \frac{C_2}{D_p \tau_n} e^{\Lambda_2 x}. \tag{5.13}$$

The solution of Eq. (5.13) is

$$p_{\text{Photo}}(x) = C_5 + C_6 e^{\frac{\mu_p E}{D_p} x} + Z_3 e^{\Lambda_1 x} + Z_4 e^{\Lambda_2 x}$$
$$+ Z_6 e^{-\alpha x}, \tag{5.14}$$

where

$$Z_6 = \frac{Z_2 - \alpha \tau_n N_{ph}}{D_p \tau_n \left[\alpha^2 + \alpha \frac{\mu_p E}{D_p}\right]}. \tag{5.15}$$

The solution for the continuity equation for holes (minorities in region R_2) and electrons now follows the same scheme with the role of electrons and holes interchanged. I have

$$\frac{d^2 p(x)}{dx^2} - \frac{\mu_p E}{D_p} \frac{dp(x)}{dx} - \frac{p(x)}{D_p \tau_p} = -\frac{N_A}{D_p \tau_p} e^{\frac{-V_{bi}}{V_t}\left(\frac{x}{W}\right)}, \tag{5.16}$$

which is solved by

$$p_{\text{Dark}}(x) = C_3 e^{\Lambda_3 x} + C_4 e^{\Lambda_4 x} + Z_7 e^{\frac{-V_{bi}}{V_t}\left(\frac{x}{W}\right)}, \tag{5.17}$$

where Z_7 and the eigenvalues Λ_3 and Λ_4 are given by

$$Z_7 = \frac{-N_A}{D_p \tau_p \left[\left(\frac{V_{bi}}{WV_t} \right)^2 + \left(\frac{V_{bi}}{WV_t} \right) \left(\frac{\mu_p E}{D_p} \right) - \left(\frac{1}{D_p \tau_p} \right) \right]},$$

(5.18)

$$\Lambda_{3,4} = \frac{\mu_p E}{2D_p} \pm \sqrt{\left(\frac{\mu_p E}{2D_p} \right)^2 + \left(\frac{1}{D_p \tau_p} \right)},$$

(5.19)

Entering Eq. (5.17) into the continuity equation for electrons yields

$$\frac{d^2 n(x)}{dx^2} + \frac{\mu_n E}{D_n} \frac{dn(x)}{dx} = \left\{ \frac{Z_7}{D_n \tau_p} - \frac{N_A}{D_n \tau_p} \right\} e^{\frac{-V_{bi}}{V_t} \left(\frac{x}{W} \right)}$$

$$+ \frac{C_3}{D_n \tau_p} e^{\Lambda_3 x} + \frac{C_4}{D_n \tau_p} e^{\Lambda_4 x}.$$

(5.20)

The solution of Eq. (5.20) is

$$n_{\text{Dark}}(x) = C_7 + C_8 e^{\frac{-\mu_n E}{D_n} x} + N_3 e^{\Lambda_3 x} + N_4 e^{\Lambda_4 x}$$

$$+ N_5 e^{\frac{-V_{bi}}{V_t} \left(\frac{x}{W} \right)},$$

(5.21)

where

$$N_3 = \frac{C_3}{D_n \tau_p \left[\Lambda_3^2 + \Lambda_3 \frac{\mu_n E}{D_n} \right]},$$

(5.22)

$$N_4 = \frac{C_4}{D_n \tau_p \left[\Lambda_4^2 + \Lambda_4 \frac{\mu_n E}{D_n} \right]},$$

(5.23)

and

$$N_5 = \frac{Z_7 - N_A}{D_n \tau_p \left[\left(\frac{V_{bi}}{WV_t} \right)^2 - \left(\frac{V_{bi}}{WV_t} \right) \left(\frac{\mu_n E}{D_n} \right) \right]}.$$

(5.24)

The partial solution under illumination under illumination is by solving

$$\frac{d^2 p(x)}{dx^2} - \frac{\mu_p E}{D_p} \frac{dp(x)}{dx} - \frac{p(x)}{D_p \tau_p} = -\frac{\alpha N_{ph}}{D_p} e^{-\alpha x}$$

(5.25)

with

$$p_{\text{Photo}}(x) \quad = \quad C_3 e^{\Lambda_3 x} + C_4 e^{\Lambda_4 x} + Z_8 e^{-\alpha x}, \tag{5.26}$$

where

$$Z_8 \quad = \quad \frac{-\alpha N_{ph}}{D_p \left[\alpha^2 + \alpha \frac{\mu_p E}{D_p} - \left(\frac{1}{D_p \tau_p} \right) \right]}, \tag{5.27}$$

For electron concentration n, it holds

$$\frac{d^2 n(x)}{dx^2} + \frac{\mu_n E}{D_n} \frac{dn(x)}{dx} = \left\{ \frac{Z_8}{D_n \tau_p} - \frac{\alpha N_{ph}}{D_n} \right\} e^{-\alpha x}. \tag{5.28}$$

The solution of Eq. (5.28) is given by

$$n_{\text{Photo}}(x) = C_7 + C_8 e^{\frac{-\mu_n E}{D_n} x} + N_3 e^{\Lambda_3 x} + N_4 e^{\Lambda_4 x}$$
$$+ N_6 e^{-\alpha x}, \tag{5.29}$$

where

$$N_6 \quad = \quad \frac{Z_8 - \alpha \tau_p N_{ph}}{D_n \tau_p \left[\alpha^2 - \alpha \frac{\mu_n E}{D_n} \right]}. \tag{5.30}$$

Now, I am able to write the whole system of differential equations in a matrix form in order to calculate the coefficients C_1, ..., C_8, up to now unknown, which determine the carrier concentrations and the their corresponding current densities at each position of the i-layer. The final matrix form of the algebraic equation defining C_1, ..., C_8 is given in Appendix B.

5.2 Matrix representation

Entering the general solutions of Appendix 5.1 into the boundary conditions [Eqs. (3.7)-(3.14)], yields eight algebraic equations for the, up to now unknown, coefficients C_1, ..., C_8. Rearranging these equations yields the matrix equations

$$\underline{\mathbf{C}}^{\text{Dark}} \;=\; \mathbf{M}^{-1}\gamma^{\text{Dark}}, \tag{5.31}$$

and

$$\underline{\mathbf{C}}^{\text{Photo}} \;=\; \mathbf{M}^{-1}\gamma^{\text{Photo}}, \tag{5.32}$$

where the vectors γ^{Dark} and γ^{Photo} are defined as

$$\gamma^{\text{Dark}} = \begin{pmatrix}
Z_1 e^{-\frac{V_{bi}}{V_t}}\left(\frac{D_n V_{bi}}{WV_t} - S_n + \mu_n E\right) + S_n N_D e^{-\frac{V_{bi}}{V_t}} \\[4pt]
N_A - Z_5 e^{-\frac{V_{bi}}{V_t}} \\[4pt]
Z_7 e^{-\frac{V_{bi}}{V_t}}\left(\frac{D_p V_{bi}}{WV_t} - S_p + \mu_p E\right) + S_p N_A e^{-\frac{V_{bi}}{V_t}} \\[4pt]
N_D - N_5 e^{-\frac{V_{bi}}{V_t}} \\[4pt]
-Z_1 e^{\frac{V_{bi}}{V_t}\left(\frac{X_c - W}{W}\right)} + N_5 e^{-\frac{V_{bi}}{V_t}\frac{X_c}{W}} \\[4pt]
-Z_5 e^{\frac{V_{bi}}{V_t}\left(\frac{X_c - W}{W}\right)} + Z_7 e^{-\frac{V_{bi}}{V_t}\frac{X_c}{W}} \\[4pt]
-Z_1 \frac{V_{bi}}{WV_t} e^{\frac{V_{bi}}{V_t}\left(\frac{X_c - W}{W}\right)} - N_5 \frac{V_{bi}}{WV_t} e^{-\frac{V_{bi}}{V_t}\frac{X_c}{W}} \\[4pt]
-Z_5 \frac{V_{bi}}{WV_t} e^{\frac{V_{bi}}{V_t}\left(\frac{X_c - W}{W}\right)} - Z_7 \frac{V_{bi}}{WV_t} e^{-\frac{V_{bi}}{V_t}\frac{X_c}{W}}
\end{pmatrix}$$

and

$$\gamma^{\text{Photo}} = \begin{pmatrix}
-Z_2\left(S_n - \mu_n E\right) - Z_2 D_n \alpha \\[4pt]
-Z_6 \\[4pt]
-Z_8\left(S_p - \mu_p E\right) e^{-\alpha W} + Z_8 D_p \alpha e^{-\alpha W} \\[4pt]
-N_6 e^{-\alpha W} \\[4pt]
-Z_2 e^{-\alpha X_c} + N_6 e^{-\alpha X_c} \\[4pt]
-Z_6 e^{-\alpha X_c} + Z_8 e^{-\alpha X_c} \\[4pt]
\alpha Z_2 e^{-\alpha X_c} - N_6 \alpha e^{-\alpha X_c} \\[4pt]
\alpha Z_6 e^{-\alpha X_c} - \alpha Z_8 e^{-\alpha X_c}
\end{pmatrix}$$

The matrix $\mathbf{M}$ is defined by

$$\mathbf{M} = \begin{pmatrix}
M_{11} & \underline{0} & M_{13} & \underline{0} \\
\underline{0} & M_{22} & \underline{0} & M_{24} \\
M_{31} & M_{32} & M_{33} & M_{34} \\
M_{41} & M_{42} & M_{43} & M_{44}
\end{pmatrix}$$

where the matrices $M_{11}...M_{44}$ are defined as

$$M_{11} = \begin{pmatrix} S_n - \mu_n E - D_n \Lambda_1 & S_n - \mu_n E - D_n \Lambda_2 \\ \frac{1}{D_p \tau_n \left[\Lambda_1^2 - \Lambda_1 \frac{\mu_p E}{D_p} \right]} & \frac{1}{D_p \tau_n \left[\Lambda_2^2 - \Lambda_2 \frac{\mu_p E}{D_p} \right]} \end{pmatrix},$$

$$M_{22} = \begin{pmatrix} (S_p - \mu_p E + D_p \Lambda_3) e^{\Lambda_3 W} & (S_p - \mu_p E + D_p \Lambda_4) e^{\Lambda_4 W} \\ \frac{1}{D_n \tau_p \left[\Lambda_3^2 + \Lambda_3 \frac{\mu_n E}{D_n} \right]} & \frac{1}{D_n \tau_p \left[\Lambda_4^2 + \Lambda_4 \frac{\mu_n E}{D_n} \right]} \end{pmatrix},$$

$$M_{13} = \begin{pmatrix} 0 & 0 \\ 1 & 1 \end{pmatrix}, M_{24} = \begin{pmatrix} 0 & 0 \\ 1 & e^{-\frac{\mu_n E}{D_n} W} \end{pmatrix},$$

$$M_{31} = \begin{pmatrix} e^{\Lambda_1 X_s} & e^{\Lambda_2 X_s} \\ \frac{1}{D_p \tau_n \left[\Lambda_1^2 - \Lambda_1 \frac{\mu_p E}{D_p} \right]} e^{\Lambda_1 X_s} & \frac{1}{D_p \tau_n \left[\Lambda_2^2 - \Lambda_2 \frac{\mu_p E}{D_p} \right]} e^{\Lambda_2 X_s} \end{pmatrix},$$

$$M_{32} = \begin{pmatrix} \frac{e^{\Lambda_3 X_s}}{D_n \tau_p \left[\Lambda_3^2 + \Lambda_3 \frac{\mu_n E}{D_n} \right]} & \frac{e^{\Lambda_4 X_s}}{D_n \tau_p \left[\Lambda_4^2 + \Lambda_4 \frac{\mu_n E}{D_n} \right]} \\ -e^{\Lambda_3 X_s} & -e^{\Lambda_4 X_s} \end{pmatrix},$$

$$M_{33} = \begin{pmatrix} 0 & 0 \\ 1 & e^{\frac{\mu_p E}{D_p} X_s} \end{pmatrix}, M_{34} = \begin{pmatrix} -1 & -e^{\frac{-\mu_n E}{D_n} X_s} \\ 0 & 0 \end{pmatrix},$$

$$M_{41} = \begin{pmatrix} \Lambda_1 e^{\Lambda_1 X_s} & \Lambda_2 e^{\Lambda_2 X_s} \\ \frac{\Lambda_1}{D_p \tau_n \left[\Lambda_1^2 - \Lambda_1 \frac{\mu_p E}{D_p} \right]} e^{\Lambda_1 X_s} & \frac{\Lambda_2}{D_p \tau_n \left[\Lambda_2^2 - \Lambda_2 \frac{\mu_p E}{D_p} \right]} e^{\Lambda_2 X_s} \end{pmatrix},$$

$$M_{42} = \begin{pmatrix} \frac{\Lambda_3 e^{\Lambda_3 X_s}}{D_n \tau_p \left[\Lambda_3^2 + \Lambda_3 \frac{\mu_n E}{D_n} \right]} & \frac{\Lambda_4 e^{\Lambda_4 X_s}}{D_n \tau_p \left[\Lambda_4^2 + \Lambda_4 \frac{\mu_n E}{D_n} \right]} \\ -\Lambda_3 e^{\Lambda_3 X_s} & -\Lambda_4 e^{\Lambda_4 X_s} \end{pmatrix},$$

$$M_{43} = \begin{pmatrix} 0 & 0 \\ 0 & \frac{\mu_p E}{D_p} e^{\frac{\mu_p E}{D_p} X_s} \end{pmatrix}, M_{44} = \begin{pmatrix} 0 & \frac{\mu_n E}{D_n} e^{\frac{-\mu_n E}{D_n} X_s} \\ 0 & 0 \end{pmatrix},$$

The solution of Eq. (5.31) or (5.32) is given by

$$\underline{C} = \begin{pmatrix} C_1 & C_2 & C_3 & C_4 & C_5 & C_6 & C_7 & C_8 \end{pmatrix}^T.$$

Note that any wavelength λ_i from the solar spectrum yields a different γ^{Photo} and hence $C_{i_{\text{Photo}}}$. Hence, the current density $J_{\text{Photo}}(\lambda_i)$ calculated from the coefficients $C_{1_{\text{Photo}}}$, ..., $C_{8_{\text{Photo}}}$ with the help of Eq. (3.17) have to be added up according to Eq. (3.18).

5.3 Werner plot A

This appendix summarizes the Werner plot A by which the series resistance is evaluated.

$$J = J_0 \left\{ \exp \left(\frac{V - JR_\text{s}}{n_\text{id} V_\text{t}} \right) - 1 \right\} + \frac{V - JR_\text{s}}{R_\text{p}} - J_\text{ph}, \tag{5.33}$$

To calculate R_s from Eq. (5.33), the following steps have to be done

1. In a-Si:H solar cells, the assumption of $R_\text{s} \ll R_\text{p}$ is accepted

2. The parallel resistance R_p is evaluated from the slope of the J/V-characteristics at $V = 0$.

3. Defining $J_\text{corr} = J - V/R_\text{p} + J_\text{ph}$.

4. $d/dV \ln(J_\text{corr}) = 1/n_\text{id} V_\text{t} - dJ/dV R_\text{s}/(n_\text{id} V_\text{t})$.

5. Plotting $d/dV ln(J_\text{corr})$ vs. dJ/dV. From the extrapolation of the data, the ideality factor n_id is evaluated at $dJ/dV = 0$ where the series resistance R_s is evaluated from the extrapolation where $d/dV \ln(J_\text{corr}) = 0$.

Chapter 6

List of symbols and abbreviations

List of symbols

Symbol	Definition	Unit
A	Effective area of the solar cell	[cm^2]
A_{pga}	Photocarrier grating amplitude	1
α	Absoprtion coefficient	[cm^{-1}]
d_{f}	Film thickness	[nm]
d_{s}	Substrate thickness	[μm]
E	Energy	[eV]
E_{act}	Activation energy	[meV]
E_{F}	Quasi-Fermi level	[meV]
E_{g}	Optical (Tauc) band gap	[eV]
E_{U}	Urbach energy	[eV]
η	Efficiency	[%]
F	Electric field	[V cm^{-1}]
f	Plasma excitation frequency	[MHz]
FF	Fill factor	[%]
G	Photogeneration rate	[W cm^{-3}]
Γ	Grating period	[nm]
J_{n}	Electron current density	[A cm^{-2}]
J_{p}	Hole current density	[A cm^{-2}]
J_{ph}	Photogenerated current density	[mA cm^{-2}]

Symbol	Definition	Unit
J_{sc}	Short-circuit current density	[mA cm^{-2}]
k	Boltzmann caonstant	[eV K^{-1}]
κ	Extinction coefficient	1
L_{α}	Absorption length	[cm]
L_{amb}	Ambipolar diffusion length	[nm]
λ	Wavelength	[nm]
$\mu\tau$	Mobility lifetime product	[cm^2 V^{-1}]
n	Concentration of electrons	[cm^{-3}]
N_{A}	Doping concentration in p-layer	[cm^{-3}]
N_{D}	Doping concentration in n-layer	[cm^{-3}]
N_{s}	Concentration of dangling bonds	[cm^{-3}]
n_{id}	Ideality factor	1
n_{rix}	Refractive index	1
P	Power density	[mW cm^{-2}]
p	Concentration of holes	[cm^{-3}]
P_{in}	Plasma power	[W]
P_{r}	Pressure of the deposition chamber	[mTorr]
Ψ	Photosensitivity	1
Φ	Illumination intensity	[mW cm^{-2}]
Q	Quality factor	1
q	Elementary charge	[A s]
QE	Quantum efficiency	[%]
R	Radius	[m]
r	Deposition rate	[Ås^{-1}]
R_{ext}	External shunt resistance	[Ω cm^2]
R_{g}	Growth rate	[Ås^{-1}]
R_{H}	Hydrogen dilution	1
R_{M}	Methane ratio	1
R_{p}	Parallel (shunt) resistance	[Ω cm^2]
R_{ref}	Reflection percentage	[%]
R_{s}	Series resistance	[Ω cm^2]
S	Surface velocity	[cm s^{-1}]
σ_{dark}	Dark conductivity	[Ω^{-1} cm^{-1}]

Symbol	Definition	Unit
σ_{g}	Average conductivity	$[\Omega^{-1}\ \mathrm{cm}^{-1}]$
σ_{photo}	Photoconductivity	$[\Omega^{-1}\ \mathrm{cm}^{-1}]$
T	Ambient temperature	[K]
T_{r}	Transmission	[%]
T_{dep}	Deposition temperature	[ºC]
t_{dep}	Deposition time	[s]
V_{bi}	Built-in voltage	[V]
V_{oc}	Open-circuit voltage	[mV]
V_{t}	Thermal voltage	[V]
ε	Built-in strain	1
W	Thickness of the i-layer	[nm]
ξ	Temperature coefficient of E_{F}	$[\mathrm{eV\ K}^{-1}]$
Y	Young's modulus	$[\mathrm{N\ m}^{-2}]$

List of abbreviations

Abbreviation	Definition
Al	Aluminium
ASA	Amorphous semiconductor analysis
a-Si	Amorphous silicon
a-Si:H	Hydrogenated amorphous silicon
a-SiC:H	Hydrogenated amorphous-carbon silicon
BS	Beam splitter
c-Si	Crystalline silicon
CIGS	Copper indium gallium diselenide
CPM	Constant photocurrent method
DPM	Defect pool model
i-layer	Intrinsic amorphous silicon layer (undoped)
n-layer	Amorphous silicon layer doped with Phosphane
ND	Neutral density
p-layer	Amorphous silicon layer doped with Boron
PECVD	Plasma enhanced chemical vapor deposition
PEN	Polyethylene naphtalene
PET	Polyethylene terephtalate
PI	Polyimide
SSPG	Steady-state photocarrier grating
TCO	Transparent conducting oxide

Publication List

1. A. Al Tarabsheh, M. B. Schubert, and J. H. Werner, *Effect of the illumination intensity on a-Si:H solar cells*, 11$^{\text{th}}$ Euregional Workshop on Thin Silicon Devices, 2-4 February 2005, Delft, The Netherlands.

2. A. Al Tarabsheh, M. B. Schubert, and J. H. Werner, *Amorphous silicon solar cells under different illumination levels*, German Physical Society 4-9 March 2005, Berlin, Germany.

3. A. Al Tarabsheh, U. Rau, and M. B. Schubert, *Novel analytical description for the current/voltage curve of p-i-n solar cell*, 21$^{\text{st}}$ EU PVSECE, 4-8 September 2006, Dresden, Germany.

4. A. Al Tarabsheh, M. B. Schubert, *Parallel resistance of integrated amorphous silicon solar cells*, Global Conference on Renewable Energy Approaches for DEsert Regions [GCREADER], 18-22 September 2006, Amman, Jordan.

5. A. Al Tarabsheh, M. B. Schubert, and J. H. Werner, *Characterization of amorphous silicon based photovoltaic modules*, PV-UNI-NETZ, "Materialforschung für die Photovoltaik", 23-24 November 2006, Technischen Universität Hamburg-Harburg, Hamburg, Germany.

6. A. Al Tarabsheh, U. Rau, and M. B. Schubert, *Analytical model for the current/voltage characteristics of amorphous silicon solar cells*, (submitted for acceptance).

Bibliography

[1] R. C. Chittick, J. H. Alexander, and H. F. Sterling, J. Electrochem. Soc. **116**, 77 (1969).

[2] W. E. Spear and P. G. Le Comber, Solid State Comm. **17**, 1193 (1975).

[3] D. E. Carlson and C. R. Wronski, Appl. Phys. Lett. **28**, 671 (1976).

[4] M. B. Schubert, Y. Ishikawa, J. W. Krämer, C. E. M. Gemmer, and J. H. Werner, *in Proc. of the 31st Photovoltaic Specialists Conference*, (IEEE, New York, 2005), p. 1488.

[5] J. A. Willemen, *Modelling of amorphous silicon single-and multi-junction solar cells*, Ph.D. thesis, Delft University of Technology (1998), p.7.

[6] R. Platz, *Amorphous silicon for optimized multi-junction solar cells: material study and cell design*, (UFO Atelier für Gestaltung & Verlag GbR, Konstanz, 1999), p. 34.

[7] S. Wieder, *Amorphous silicon solar cells: comparison of p-i-n and n-i-p structures with zinc-oxide frontcontact*, Ph.D. thesis, Forschungszentrum Jülich (1999), p. 9.

[8] G. W. Neudeck and A. K. Malhotra, J. Appl. Phys. **46**, 239 (1975).

[9] G. Bruno, P. Capezzuto, and A. Madan, *Plasma deposition of amorphous silicon-based materials*, (Academic Press, California, 1995), p. 4.

[10] R. A. Street, *Technology and applications of amorphous silicon*, (Springer-Verlag Heidelberg, Berlin, 2000), p. 40.

[11] J. Ballutaud, *Study of radio-frequency plasma deposition of amorphous silicon for the improvement of the cell production*, Ph.D. thesis, Université Paris (2003), p. 1.

[12] A. Matsuda, Plasma Phys. Control. Fusion **39**, 431 (1997).

[13] J. C. Knights, T. M. Hayes, and J. C. Mikkelsen, Phys. Lett. **39**, 712 (1977).

[14] J. Perrin, P. R. Cabarrocas, B. Allain, and J. Freidt, Jpn. J. Appl. Phys. 27, 2041 (1988).

[15] R. A. Street, J. Zesch, and M. J. Thompson, Appl. Phys. Lett. **43**, 672 (1983).

[16] J. Perrin, P. Roca i Cabarrocas, B. Allian, J. M. Friedt, Jpn. J. Appl. Phys. **27**, 2041 (1988).

[17] N. Layadi, P. Roca i Cabarrocas, B. Drévillon, and I. Solomon, Phys. Rev. B **52**, 5136 (1995).

[18] S. Hamma and P. Roca i Cabarrocas, J. Appl. Phys. **81**, 7282 (1997).

[19] Y. M. Li, Ilsin An, H. V. Nguyen, C. R. Wronski, and R. W. Collins, Appl. Phys. Lett. **68**, 2814 (1992).

[20] G. Ganguly, Phys. Rev. B **47**, 3661 (1993).

[21] C. Böhm, J. Perrin, and P. Roca i Cabarrocas, J. Appl. Phys. **73**, 2578 (1993).

[22] J. Robertson, Phys. Rev. B **31**, 3817 (1985).

[23] R. A. Street, J. Kakalios, and T. M. Hayes, Phys. Rev. B **34**, 3030 (1986).

[24] D. Das, Solid State Phenomena **44-46**, 227 (1995).

[25] R. E. I. Schropp and M. Zeman, *Amorphous and microcrystaline silicon solar cells: modeling, materials and device technology*, (Kluwer Academic Publishers Group, Dordrecht, 1998). p. 9.

[26] J. A. Reimer, R. W. Vaughan, and J. C. Knights, Phys. Rev. B **24**, 3360 (1981).

[27] X. Deng and E. Schiff, *Amorphous silicon based solar cells*(John Wiley & Sons, Chichester, 2003), p. 18.

[28] N. Wang, *Improving the stability of amorphous silicon solar cells by chemical annealing*, Ph.D. thesis, Iowa State University (2006), p. 29.

[29] www.diplot.de.

[30] R. Swanepoel, J. Phys. E: Sci. Instrum. **16**, 1214 (1983).

[31] private communication of M. B. Schubert, 19 December 2005.

[32] R. Street, *Hydrogenated amorphous silicon*, (Cambridge University Press, Cambridge, 1991), p. 228.

[33] N. Beck, N. Wyrsch, Ch. Hof, and A. Shah, J. Appl. Phys. **79**, 9361 (1996).

[34] V. Augelli, R. Murri, and N. Alba, J. Appl. Phys. **54**, 248 (1983).

[35] J. Yoon, J. Jang, and C. Lee, J. Appl. Phys. **64**, 6591 (1988).

[36] H. Brummack, *Optimierung von driftbestimmten Solarzellen aus Amorphem und Nanokristalliem Silizium*, Ph.D. thesis, Universität Stuttgart, (2000), p. 35.

[37] J. A. Schmidt and F. A. Rubinelli, J. Appl. Phys. **83**, 339 (1998).

[38] M. Vaněček, J. Kočka, A. Poruba, and A. Fejfar, J. Appl. Phys. **78**, 6203 (1995).

[39] R. Platz, *Amorphous silicon for optimized multi-junction solar cells: material study and cell design*, (UFO Atelier für Gestaltung & Verlag GbR, Konstanz, 1999), p. 14.

[40] F. Urbach, Phys. Rev. **92**, 1324 (1953).

[41] Z. Smith, V. Chu, K. Shepard, S. Aljishi, D. Slobodin, J. Kolodzey, and S. Wagner, Appl. Phys. Lett. **50**, 1521 (1987).

[42] J. A. Schmidt, Phys. Rev. B **71**, 125208 (2005).

[43] C. Droz, *Thin film microcrystalline silicon layers and solar cells: microstructure and electrical performances*, Ph.D. thesis, Université de Neuchaâtel (2003), p. 60.

[44] Qing Gu, E. A. Schiff, S. Grebner, F. Wang, and R. Schwarz, Phys. Rev. Lett. **76**, 3196 (1996).

[45] D. Ritter, K. Weiser, and E. Zeldov, J. Appl. Phys. **62**, 4563 (1987).

[46] I. Balberg, A. E. Delahoy, and H. A. Weakliem, Appl. Phys. Lett. **53**, 992 (1988).

[47] I. Balberg, A. E. Delahoy, and H. A. Weakliem, Appl. Phys. Lett. **53**, 1949 (1988).

[48] D. Ritter, E. Zeldov, and K. Weiser, Appl. Phys. Lett. **49**, 791 (1986).

[49] K. Hattori, H. Okamoto, and Y. Hamakawa, Phys. Rev. B **45**, 1126 (1992).

[50] C. Koch, *Niedertemperaturabscheidung von Dünnschicht Silicium für Solarzellen auf Kunststofffolien*, Ph.D. thesis, Universität Stuttgart (2002), p. 30.

[51] www.kobelco.co.jp/p108/dmn/e/dmn08e.htm.

[52] H. Gleskova, J. Cheng, S. Wagner, J. Sturm, and Z. Suo, Solar Energy **80**, 687 (2006).

[53] Z. Suo, E. Y. Ma, H. Gleskova, and S. Wagner, Appl. Phys. Lett. **74**, 1177 (1999).

[54] I. Chen and S. Lee, J. Appl. Phys. **53**, 1045 (1982).

[55] A. Mittiga, P. Fiorini, M. falconieri, and F. Evangelisti, J. Appl. Phys. **66**, 2667 (1989).

[56] H. Matsuura, A. Matsuda, H. Okushi, and K. Tanaka, J. Appl. Phys. **58**, 1578 (1985).

[57] J. Merten, J. M. Asensi, C. Voz, A. V. Shah, R. Platz, and J. Andreu, IEEE Transactions on Electron Devices **45**, 423 (1998).

[58] K. Orgassa, *Coherent optical analysis of the ZnO/CdS/Cu(In,Ga)Se₂ thin film solar cell*, Ph.D. thesis, Universität Stuttgart (2004), p. 17.

[59] C. Hof, *Thin film solar cells of amorphous silicon: influence of i-layer material on the cell efficiency*, Ph.D. thesis, Université de Neuchâtel (1999), p. 36.

[60] M. Zeman, M. Kroon, and J. Heuvel, *Amorphous Semiconductor Analysis (ASA), users manual*, (Delft University of Technology, 1999), p. 2.

[61] M. Zeman, J. A. Willeman, L. L. A. Vosteen, G. Tao, and W. J. Metselaar, Solar Energy and Solar Cells **46**, 81 (1999).

[62] J. Willemen, M. Zeman, and J. W. Metselaar, *in Proc. of the 1st WCPEC*, (IEEE, Hawaii, 1994), p. 599.

[63] M. J. Powel, S. C. Deane, Phys. Rev. B **48**, 10815 (1993).

[64] M. J. Powel, S. C. Deane, Phys. Rev. B **53**, 10121 (1996).

[65] B. A. Korevaar, *Integration of expanding thermal plasma deposited hydrogenated amorphous silicon in solar cells*, Ph.D. thesis, Eindhoven University of Technology (2002), p. 44.

[66] R. Crandall, J. Appl. Phys. **53**, 3350 (1982).

[67] K. Taretto, U. Rau, and J. H. Werner, Appl. Phys. A **77**, 865 (2003).

[68] K. Taretto, U. Rau, Prog. Photovolt: Res. Appl. **12**, 573 (2004).

[69] G. Oliver, *Solarzellen aus amorphem Silizium auf Aluminium: Drei Wege, den Substrateinfluss zu beschreiben*, Ph.D. thesis, Université de Neuchâtel (1997), p. 69.

[70] S. Y. Myong, S. S. Kim, and K. S. Lim, J. Appl. Phys. **95**, 1525 (2004).

[71] M. A. Kroon and R. A. C. M. M. van Swaaij, J. Appl. Phys. **90**, 994 (2001).

[72] R. Crandall, J. Appl. Phys. **53**, 3350 (1982).

[73] H. Okamoto, H. Kida, S. Nomomura, K. Fukumoto, and Y. Hamakawa, J. Appl. Phys. **54**, 3236 (1983).

[74] K. Misiakos and F. A. Lindholm, J. Appl. Phys. **64**, 283 (1988).

[75] R. Crandall, J. Appl. Phys. **54**, 7176 (1983).

[76] A. R. Moore, Appl. Phys. Lett. **31**, 762 (1977).

[77] W. R. Fahrner, G. Grabosch, D. Borchert, Y. Chan, S. Kwong, and K. Man, J. Solid State Electrochem. **3**, 245 (1999).

[78] S. M. Sze, *Physics of Semiconductor Devices*, (John Wiley & Sons, New York, 1981), p. 75.

[79] A. L. Fahrenbruch and R. H. Bube, *Fundamentals of Solar Cells* (Academic Press, New York, 1983), p. 73.

[80] S. Dimitrijev, *Understanding Semiconductor Devices*, (Oxford University Press, New York, 2000), p. 32.

[81] Ref. [78], p. 56.

[82] J. M. Asensi, J. Merten, C. Voz, and J. Andreu, J. Appl. Phys. **85**, 2939 (1999).

[83] P. Alpuima and V. Chu, J. Appl. Phys. **68**, 3812 (1999).

[84] R. M. A. Dawson, C. M. Fortmann, M. Gunes, Y. M. Li, S. S. Nag, R. W. Collins, and C. R. Wronski, Appl. Phys. Lett. **63**, 955 (1993).

[85] C. Koch, M. Ito, M. B. Schubert, and J. H. Werner, Mat. Res. Soc. Symp. Proc. **557**, 749 (1999).

[86] M. K. van Veen and R. E. I. Schropp, J. Appl. Phys. **93**, 121 (2003).

[87] A. Smets, *Growth related material properties of hydrogenated amorphous silicon*, Ph.D. thesis, Eindhoven University of Technology (2002), p. 11.

[88] C. Koch, *Niedertemperaturabscheidung von Dünnschicht Silicium für Solarzellen auf Kunststofffolien*, Ph.D. thesis, Universität Stuttgart (2002), p. 91.

[89] J. Robertson, Mat. Res. Soc. Symp. Proc. vol. 609, 1.4 (2000).

[90] C. Tsai, amorphous silicon and related materials, vol. A, 123 (1998).

[91] K. F. Feenstra, R. E. Schropp, and W. F. Van der Weg, J. Appl. Phys. **85**, 6843 (1999).

[92] J. Yang, X. Xu, and S. Guha, Mat. Res. Soc. Sym. Proc. **336**, 687 (1994).

[93] P. Alpuim, and V. Chu, J. Appl. Phys. **86**, 3812 (1999).

[94] P. Alpuim, V. Chu, and J. P. Conde, J. Vac. Sci. Technol. A 21(4), 1048 (2003).

[95] S. Guha, J. Yang, A. Banerjee, B. Yan, and K. Lord, Solar Energy Materials and Solar Cells **78**, 329 (2003).

[96] See page 69 in Ref. [32].

[97] T. Fujibayashi, J. Appl. Phys. **99**, 043703 (2006).

[98] H. Pfleiderer, Mat. Res. Soc. Symp. Proc. vol. 297, 791 (1993).

[99] A. Yamada, J. Kenne, M. Konagia, and K. Takahashi, Appl. Phys. Lett. **46**, 272, (1985).

[100] Y. Tawada, K. Tsuge, M. Kondo, H. Okamoto, and Y. Hamakawa, J. Appl. Phys. **53**, 5273 (1982).

[101] See page 13 in Ref. [7].

[102] J. K. Arch, F. A. Rubinelli, J. Y. Hou, and S. J. Fonash, J. Appl. Phys. **69**, 7057 (1991).

[103] A. Dasgupta, A. Lambertz, O. Vetterl, F. Finger, R. Carius, U. Zastrow, and H. Wagner, *16th European Photovoltaic Solar Energy Conference and Exhibition*, (Glasgow, 2000), p. 557.

[104] G. M. Ferreira, Chi Chen, R. J. Koval, J. M. Pearce, C. R. Wronski, and R. W. Collins, Journal of Non-Crystalline Solids **338**, 694 (2004).

[105] J. Merten, C. Voz, A. Munõz, J. M. Asensi, J. Andreu, Solar Enrgy Materials and Solar Cells **57**, 153 (1999).

[106] N. Palit and P. Chatterjee, J. Appl. Phys. **86**, 6879 (1999).

[107] A. Berger, *Amorphous silicon solar cells on plastic films*, Student work, Universität Stuttgart (2005), p. 46.

[108] Y. Kishi, H. Inoue, K. Murata, S. Kouzuma, M. Morizane, H. Shubuya, H. Nishi-waki, and Y. Kuwano, Jpn. J. Appl. Phys. **31**, 12 (1992).

[109] U. Kroll, J. Meier, H. Keppner, S. D. Littlewood, I. E. Kelly, P. Giannoulés, and A. Shah, J. Vac. Sci. Technol. A **13**, 2743 (1995).

[110] S. Tsuda, T. Takahama, M. Isomura, H. Tarui, Y. Nakashima, Y. Hishikawa, N. Nakamura, T. Matsuoka, H. Nishawaki, S. Nakano, M. Ohnishi, and Y. Kuwano, Jpn. J. Appl. Phys. **26**, 33 (1987).

[111] D. E. Carlson, J. Vac. Sci. Technol. **20**, 290 (1981).

[112] J. H. Werner, Appl. Phys. A. **47**, 292 (1988).

[113] C. D. Abel, *Photoelektronische Charakterisierung amorpher Halbleiter*, Ph.D. thesis, Universität Stuttgart (1993), p. 25.

[114] A. Takano and T. Kamoshita, Jpn. J. Appl. Phys. **86**, 3812 (1999).

[115] L. D. Partain, *Solar cells and their applications*, (John Wiley & Sons, New York, 1995), p. 164.

[116] C. E. M. Gemmer, *Analytische und numerische Untersuchungen von Solarzellen unter wechselnden Beleuchtungsbedingungen*, Ph.D. thesis, Universität Stuttgart (1993), p. 116.

Acknowledgment

At this point, I would like to acknowledge

- My parents and my brother Khaled, for their continuous support and encouragement and for all they did for me.

- My wife, Eshraq, who is my life, for her daily supporting, understanding and the great patience for being away from her. I miss you my young daughter Wafaa Besan.

Thank you!
Anas Al Tarabsheh

Curriculum Vitae

Anas Ibrahim Qasem Al Tarabsheh

30.06.1978	Born in Irbid, Jordan.
1984-1990	Primary school, Irbid.
1990-1993	Preparatory school, Irbid.
1993-1996	Secondary school, Irbid.
1996-2000	College studies at the department of electrical engineering in Jordan University of Science and Technology (JUST).
09.2000	Bachelor degree in communications and electronics.
2000-2002	Instructor at the department of electrical engineering in JUST.
09.2002	Master degree in communications and electronics (JUST).
06.2002-02.2003	Lecturer at the department of electrical and computer engineering in the Hashemite University.
03.2003-02.2007	Ph.D. student at the *Institut für Physikalische Elektronik* in *Universität Stuttgart*, Germany.
02.2007-now	Assistant Professor at the Hashemite University.